AD NUMBER

AD907635

LIMITATION CHANGES

TO:

Approved for public release; distribution is unlimited.

FROM:

Distribution authorized to U.S. Gov't. agencies only; Test and Evaluation; FEB 1973. Other requests shall be referred to Air Force Weapons Lab., Kirtland AFB, NM.

AUTHORITY

AFWL ltr 30 Apr 1986

AD 907 635

AUTHORITY:
AFWL etc,
30 Apr 86

AFWL-TR-
72-202

ANGULAR VIBRATION EFFECTS ON A TELESCOPE SYSTEM

Lawrence Sher

TECHNICAL REPORT NO. AFWL-TR-72-202

February 1973

AIR FORCE WEAPONS LABORATORY
Air Force Systems Command
Kirtland Air Force Base
New Mexico

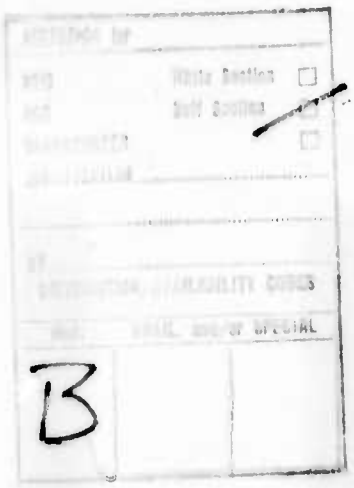

AIR FORCE WEAPONS LABORATORY
Air Force Systems Command
Kirtland Air Force Base
New Mexico 87117

AFWL-TR-72-202

ANGULAR VIBRATION EFFECTS ON A TELESCOPE SYSTEM

Lawrence Sher

Feb 73

Technical rpt. Jun – Sep 72,

TECHNICAL REPORT NO. AFWL-TR-72-202

AF-317J

FOREWORD

The research was performed under Program Element 63605F, Project 317J, Task II.

Inclusive dates of research were January 1972 through September 1972. The report was submitted 8 December 1972 by the Air Force Weapons Laboratory Project Officer, Mr. Lawrence Sher (LRO).

The author would like to acknowledge the help given by the NASA Manned Spacecraft Center, Houston, Texas, in supplying the ADAs, in particular Mr. Robert G. Chilton, Chief, Guidance and Control Division. The help of the Aircraft Use Committee of the USAEC, Nevada Operations Office, in particular, Mr. Kenneth N. Joy, in providing the use of the NC-135 aircraft and AEC facilities, is acknowledged.

Acknowledgment is made to Dr. Glen Morris of EG&G and his co-workers, who installed the equipment and analyzed the flight data.

Thanks are due to Capt Robert J. Johnson of the Air Force Weapons Laboratory for writing the programs to calculate optical system errors.

This technical report has been reviewed and is approved.

LAWRENCE SHER
Project Officer

EDWARD N. LAUGHLIN
Major, USAF
Chief, Optics Technology Branch

DONALD L. LAMBERSON
Colonel, USAF
Chief, Laser Division

ABSTRACT

(Distribution Limitation Statement B)

The results of angular vibration measurements made at three stations in an NC-135 aircraft are described. The magnitude of the relative motions between stations is calculated. The requirements for the range of corrections required for an autocollimator to correct the relative motion between the three stations are determined. The effects of the motions at the aircraft ceiling on the angular stability of various types of pointing systems are calculated and discussed.

CONTENTS

ILLUSTRATIONS

ILLUSTRATIONS (CONT'D)

TABLES

SECTION I

INTRODUCTION

The optical system considered here consists of a pointing system used to direct a laser beam from an aircraft. The laser is located on the floor of the aircraft, and its beam is relayed by a mirror to the ceiling, into the base of a beam director, which is used to point the beam to a target. This type of system has many applications for Air Force missions, including high-bandwidth, secure, data links. The objective of this study was to determine the magnitude of the angular vibrations at the three stations of interest in a C-135 aircraft where the optical elements would be placed.

Angular vibrations deteriorate system-pointing capability in two ways. First, given a stabilized pointing system, the beam will be diverted from the target if the beam is misaligned coming into the beam director. Thus, any motion of the relay mirror or source relative to a reference surface on the beam director is important. If this motion is larger than the pointing requirements, then some sort of active alignment system is needed, and one will need to know the dynamic range required of the autocollimator.

The second major effect of angular vibration is the destabilization of the beam director. If the director has a telescope stabilized about three axes or more, the effects are small. If a two-axis stabilized beam director is used, then the aircraft motion will misdirect the beam due to kinematic coupling effects.

The results of the vibration measurements made at three stations in a C-135 aircraft indicate that the largest relative motion in the optical path is 26 μr rms from 5 Hz to 2000 Hz. The motion that an autocollimator would have to remove would be twice that amount, or 52 μr. The motions at the aircraft ceiling, where the beam director would be located, are at most 22 μr rms from 5 Hz to 2000 Hz. Summaries of all vehicle data can be found in section II. The use of tracking and stabilization systems with various bandwidths are discussed in section III and the effects of using rotational vibration isolators is discussed as well. The method of evaluating the misalignment effects when there are motions of all three elements in the optical system is described in section IV. A description

of the equipment used to make the measurements and their installation in the C-135 aircraft is given in section V.

SECTION II

FLIGHT DATA SUMMARY

Angular velocity data were taken at three stations on an NC-135A aircraft owned by the Atomic Energy Commission and was used by the Air Force Special Weapons Center for test programs. The aircraft has a dome, on top of the forward part of the fuselage, that is used to house several instrumentation packages. An outline drawing of the aircraft is seen in figure 1. It was felt that this aircraft having a dome would be subjected to vibrations in the same way as any large aircraft with large protuberances in the airstream. The dome on this aircraft is a fairly compliant structure made from fiberglass and may not transmit windloads to the structure as a metal structure would. The eight angular vibration transducers, were mounted at three stations: three at FS 409 WL 299 (top), three at FS 409 WL 210 (floor), and two at FS 554 WL 217 (floor).

The two-sensor package measured only pitch and yaw information. Roll information at this station is not needed for a beam transmitting system, although it is quite important for a receiving imaging system.

Two flights were conducted in March and April 1972 to evaluate other inertial navigation equipment on board the aircraft. The flights consisted of takeoffs, straight and level portions, orbits of 2 g to test the navigator, rapid descent maneuvers, final approaches and landing. Four sections of flight data were analyzed and consisted of 1 minute sequences. The data sections were:

Data set No. 1 -- After lift-off on takeoff of first flight.

Data set No. 2 -- After climb out on takeoff of first flight at an altitude of approximately 20,000 feet.

Data set No. 3 -- During straight and level flight on the second flight at approximately 20,000 feet.

Data set No. 4 -- During final approach with flaps down after the second flight.

The data from the eight angular velocity transducers (ADAs) were digitized and subjected to power and cross spectral analysis from 5 Hz to 2000 Hz. The spectral bandwidth varied with frequency as:

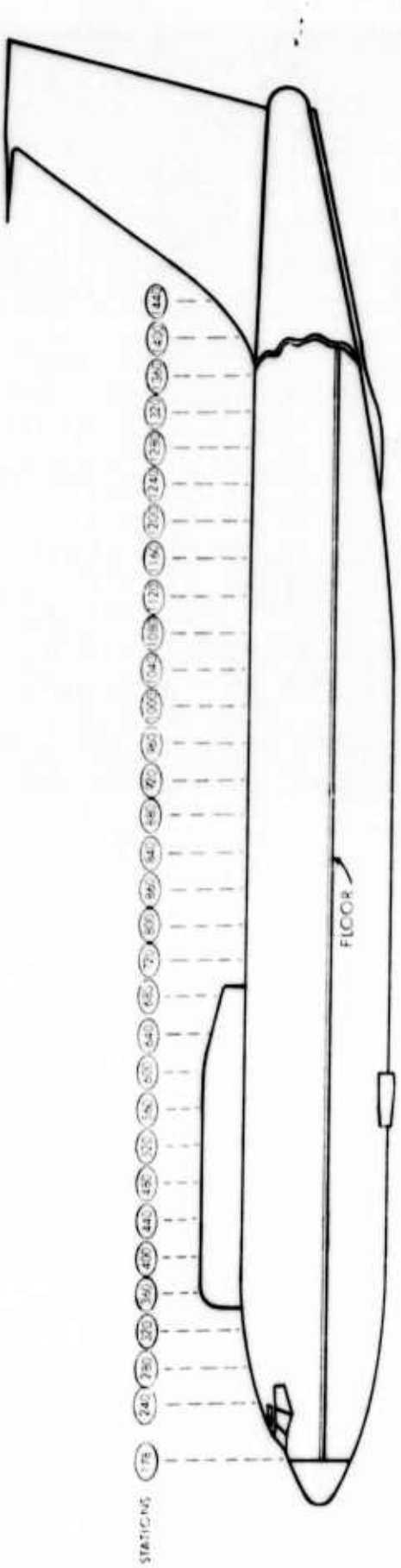

Figure 1. NC-135 Aircraft

Frequency Range	Bandwidth
5 to 20 Hz	1 Hz
20 to 100 Hz	5 Hz
100 to 200 Hz	20 Hz
200 to 2000 Hz	100 Hz

The data were reduced digitally using fast Fourier transform techniques (FFT) and converted from angular velocity spectra to angle spectra by dividing each spectra point by its frequency squared. The power and cross spectra (the real parts) were combined to determine relative angular motions, as defined in section IV. The area under each curve was calculated and the rms value of each quantity was determined. Table I shows a tabulation of each parameter for all data sets. The angles are defined about the axes as shown in figure 2. The power spectral density (PSD) of the angles for data set No. 2 are shown in figures 3 through 10. The PSDs for the remaining flights are shown in appendix B.

TABLE I

rms ANGLES AND ANGULAR VELOCITIES

Rate	Angle	Data Set 1 After Lift Off		Data Set 2 During Climb Out		Data Set 3 Straight and Level		Data Set 4 Final Approach	
		Rate	Angle	Rate	Angle	Rate	Angle	Rate	Angle
		deg/sec	μr	deg/sec	μr	deg/sec	μr	deg/sec	μr
$\dot{\alpha}$	α	0.36	12	0.14	4.4	0.12	2	0.11	5.5
$\dot{\beta}$	β	0.08	12	0.04	4.5	0.03	1.3	0.04	4.8
$\dot{\alpha}_i$	α_i	0.25	12.7	0.08	5	0.07	2	0.1	4.9
$\dot{\beta}_i$	β_i	0.07	10.6	0.03	3.4	0.03	1	0.03	3.4
$\dot{\gamma}_i$	γ_i	0.17	13.2	0.07	13.6	0.05	1.5	0.06	6.6
$\dot{\alpha}_T$	α_T	0.41	13.2	0.7	8.5	0.37	4	0.15	4.1
$\dot{\beta}_T$	β_T	0.08	12.9	0.12	3.4	0.07	1.3	0.04	4.5
$\dot{\gamma}_T$	γ_T	0.44	21.8	1.07	13.6	0.5	5.6	0.16	10.1

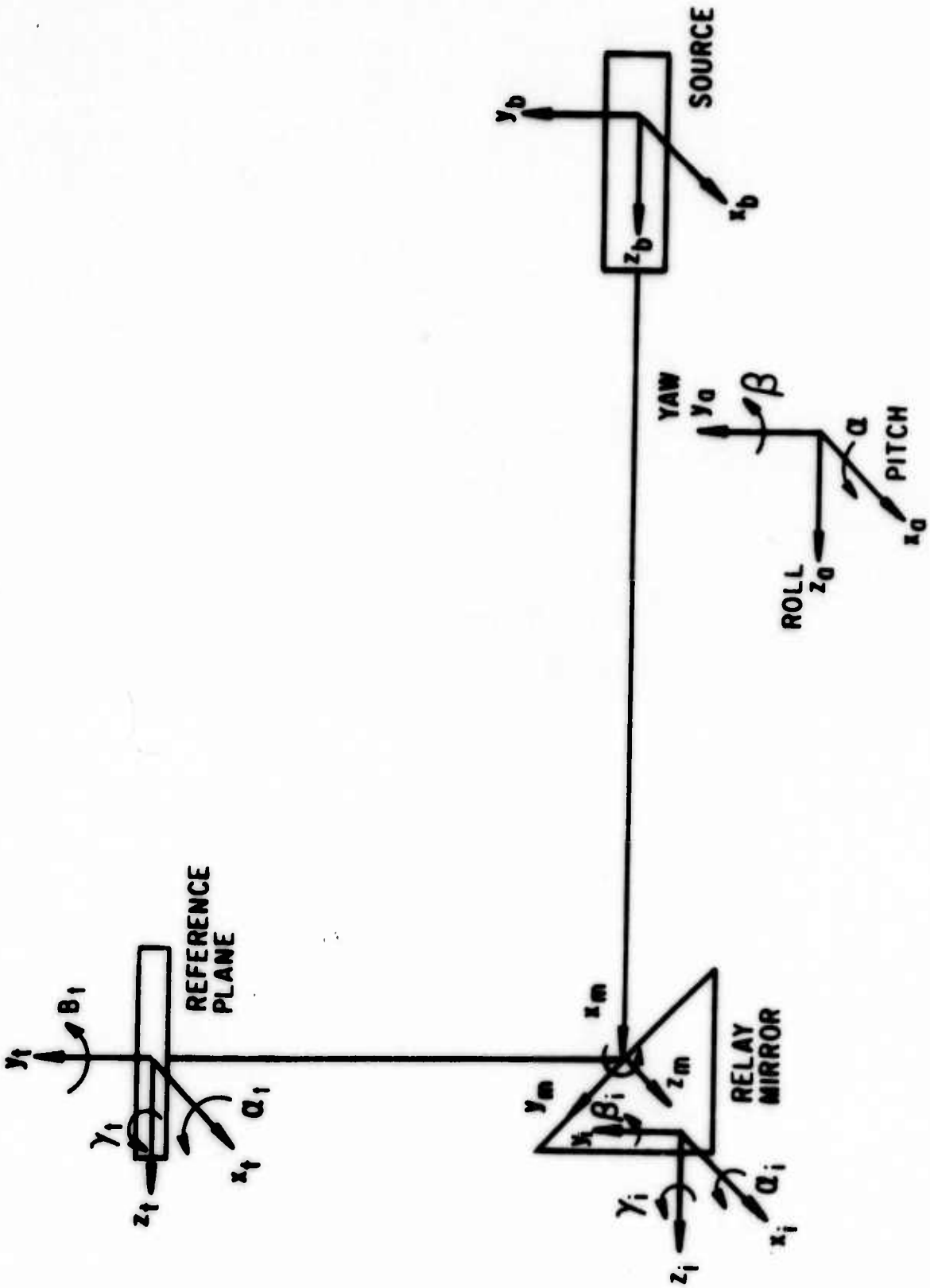

Figure 2. Optical System Definition

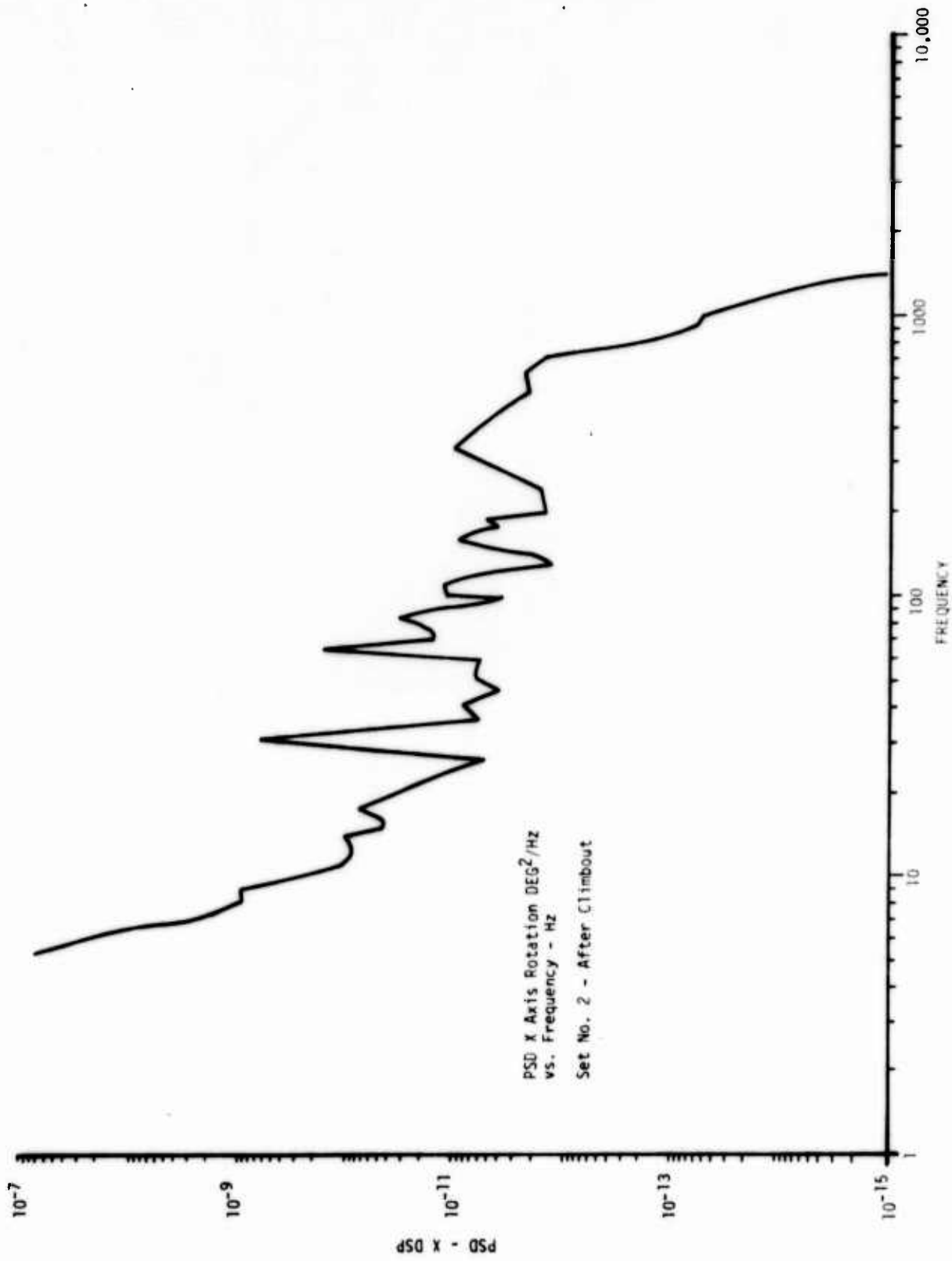

Figure 3. PSD of X Rotation - Set No. 2

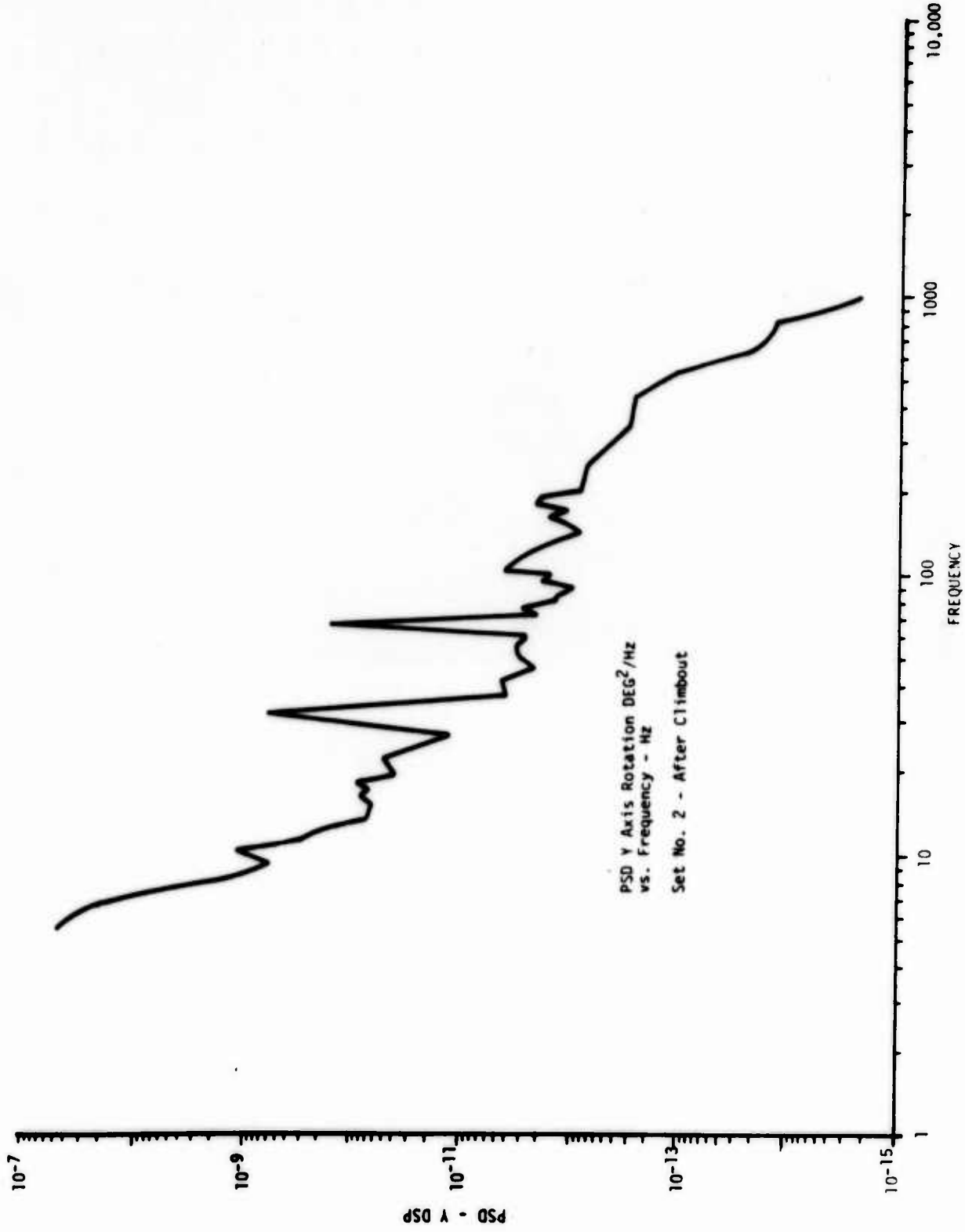

Figure 4. PSD of Y Rotation - Set No. 2

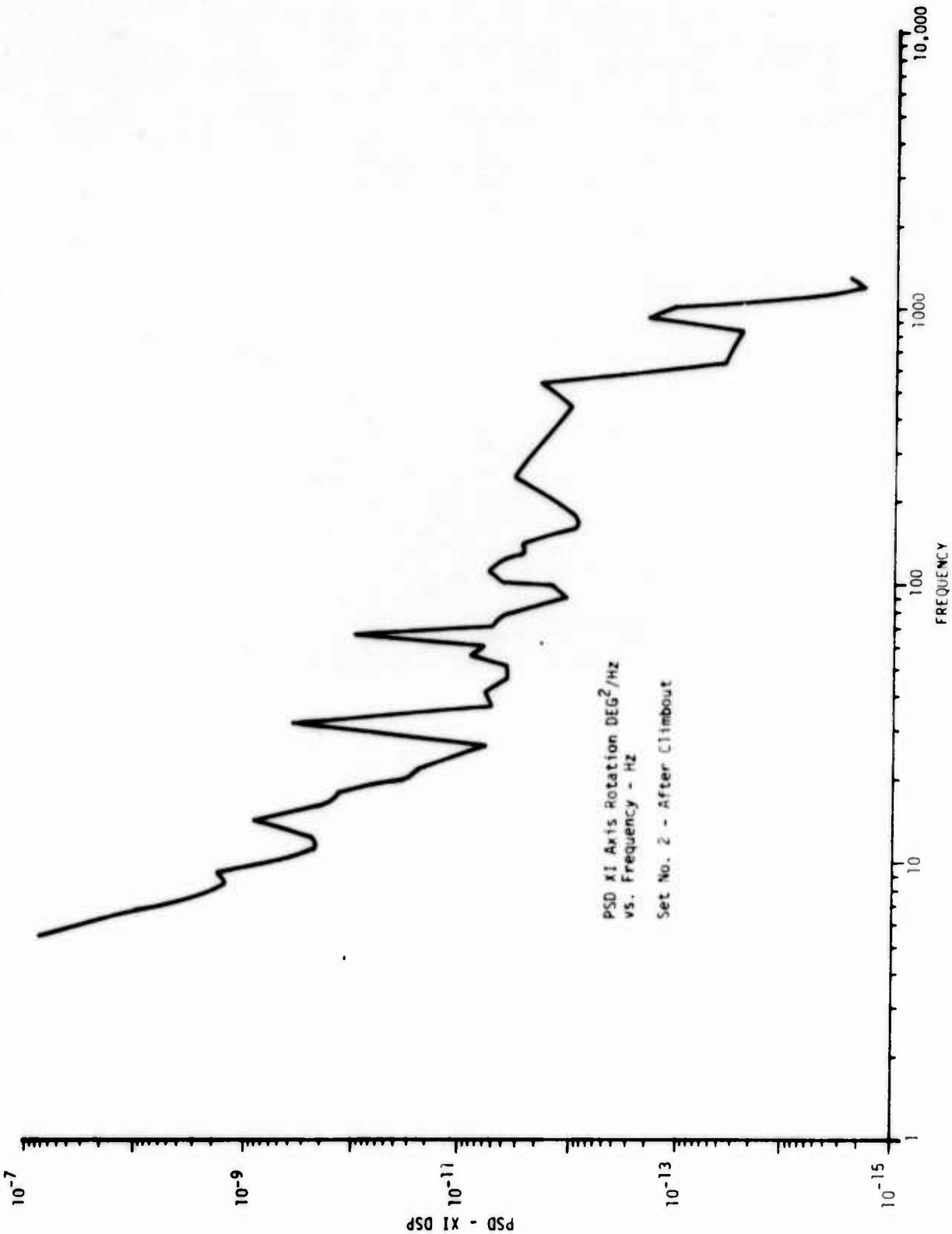

Figure 5. PSD of XI Rotation - Set No. 2

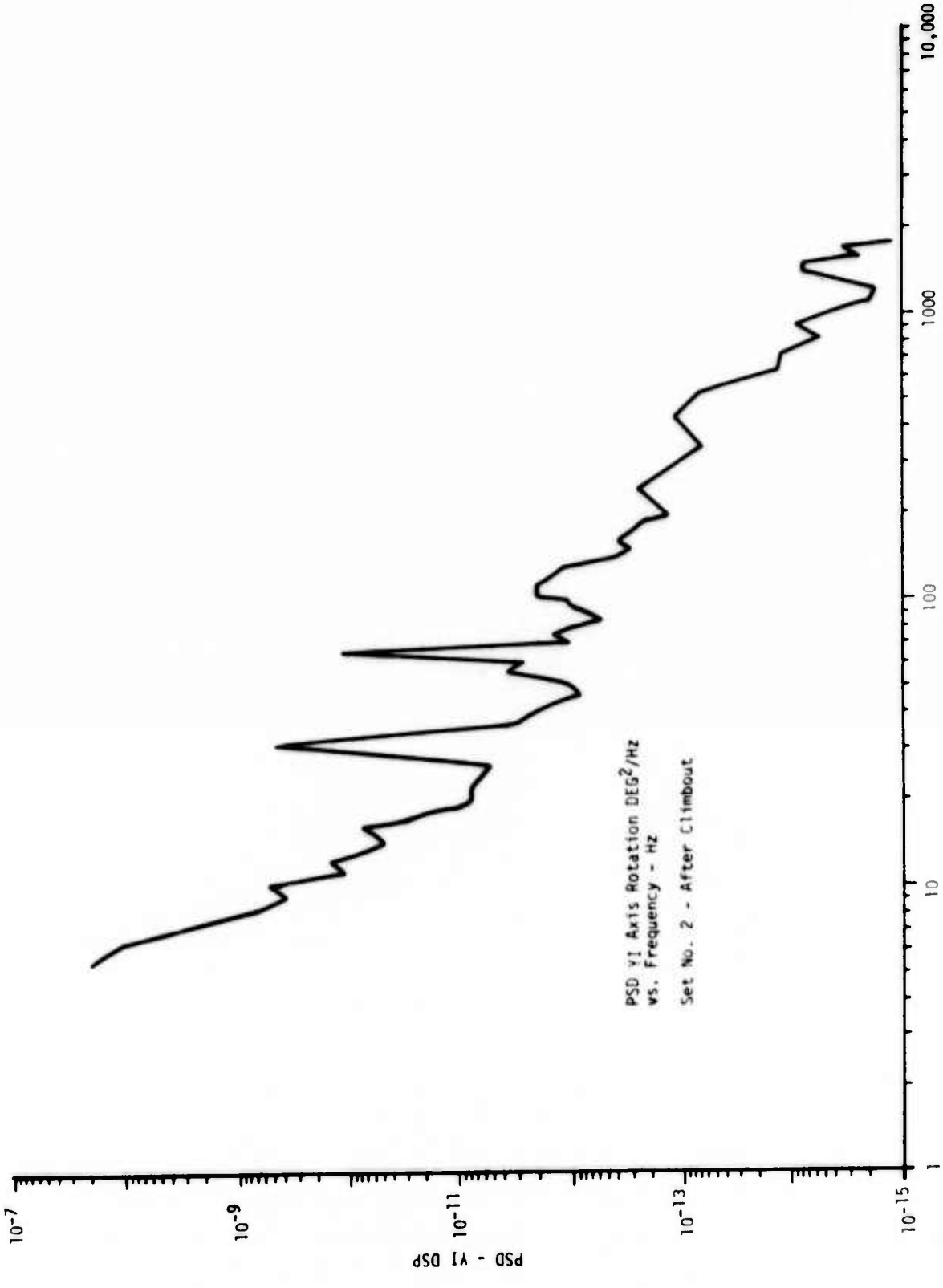

Figure 6. PSD of YI Rotation - Set No. 2

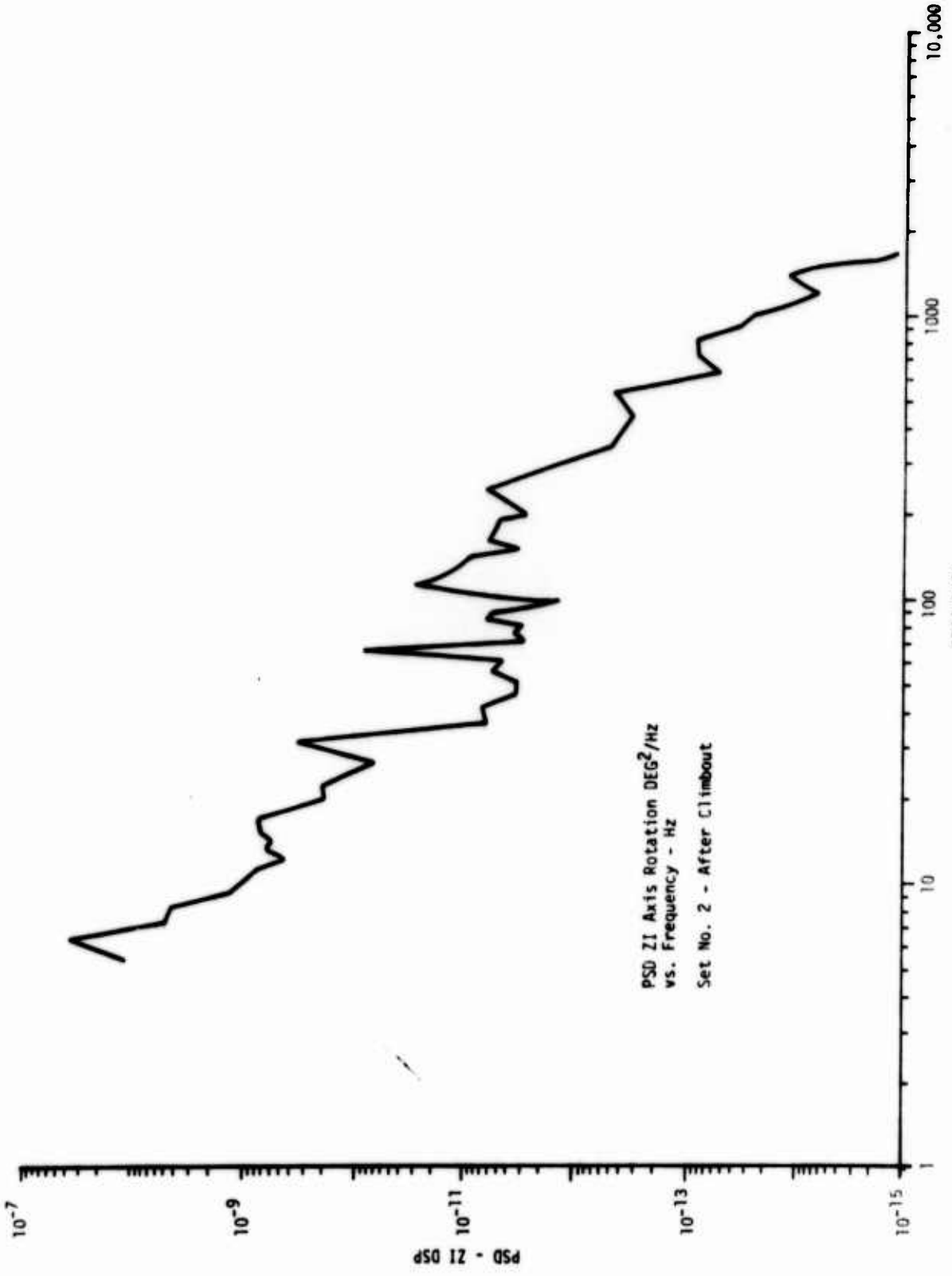

Figure 7. PSD of ZI Rotation - Set No. 2

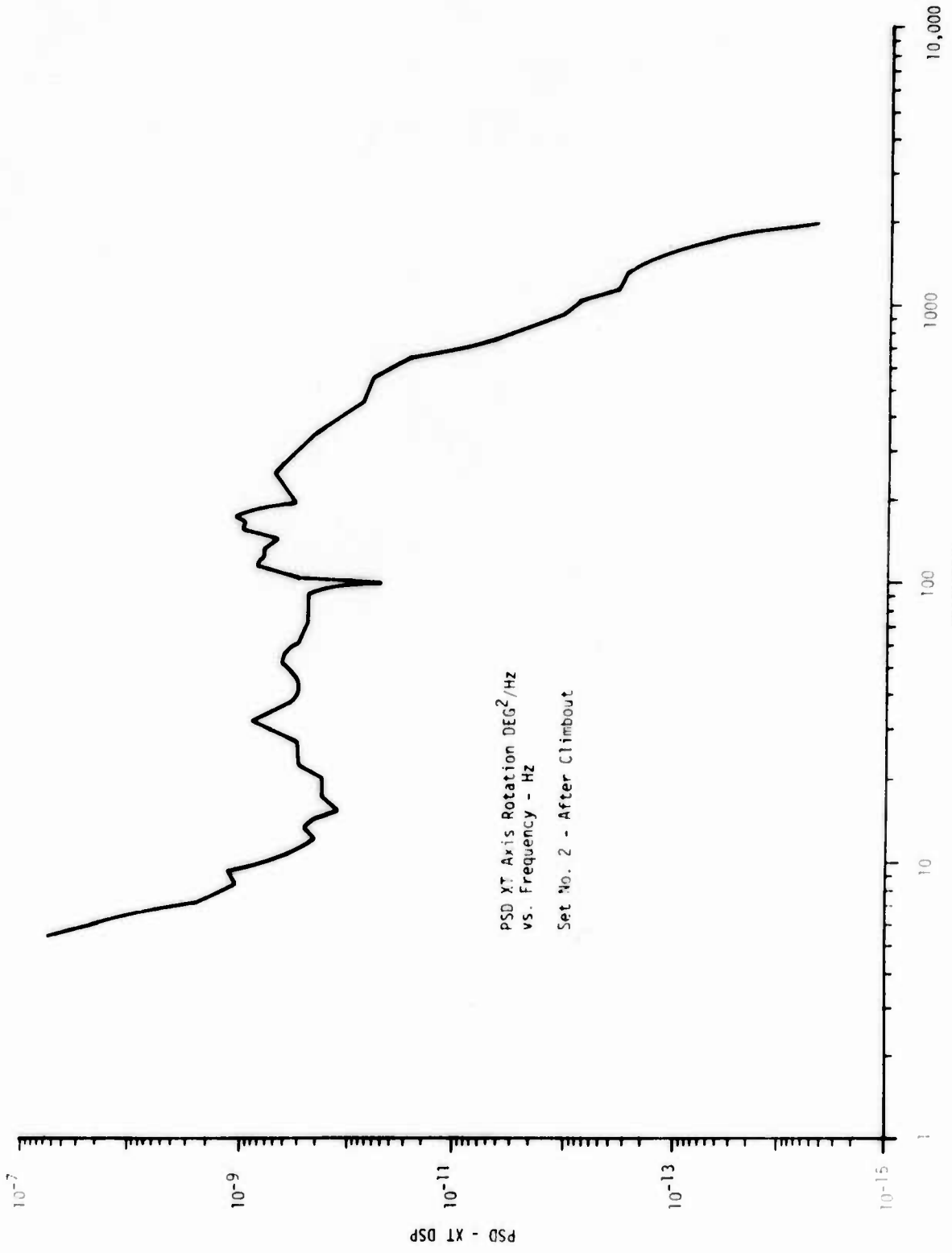

Figure 8. PSD of XT Rotation - Set No. 2

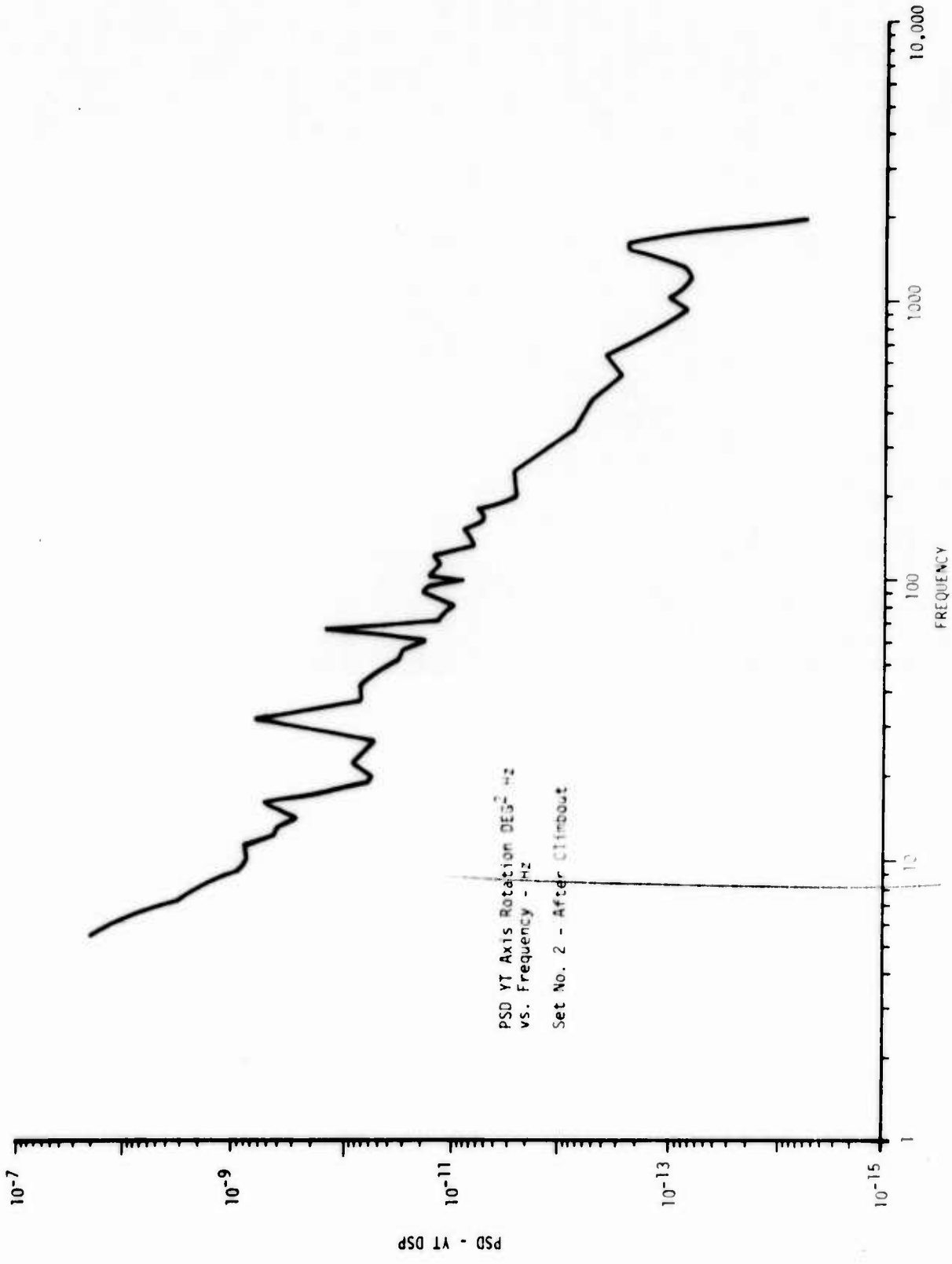

Figure 9. PSD of YT Rotation - Set No. 2

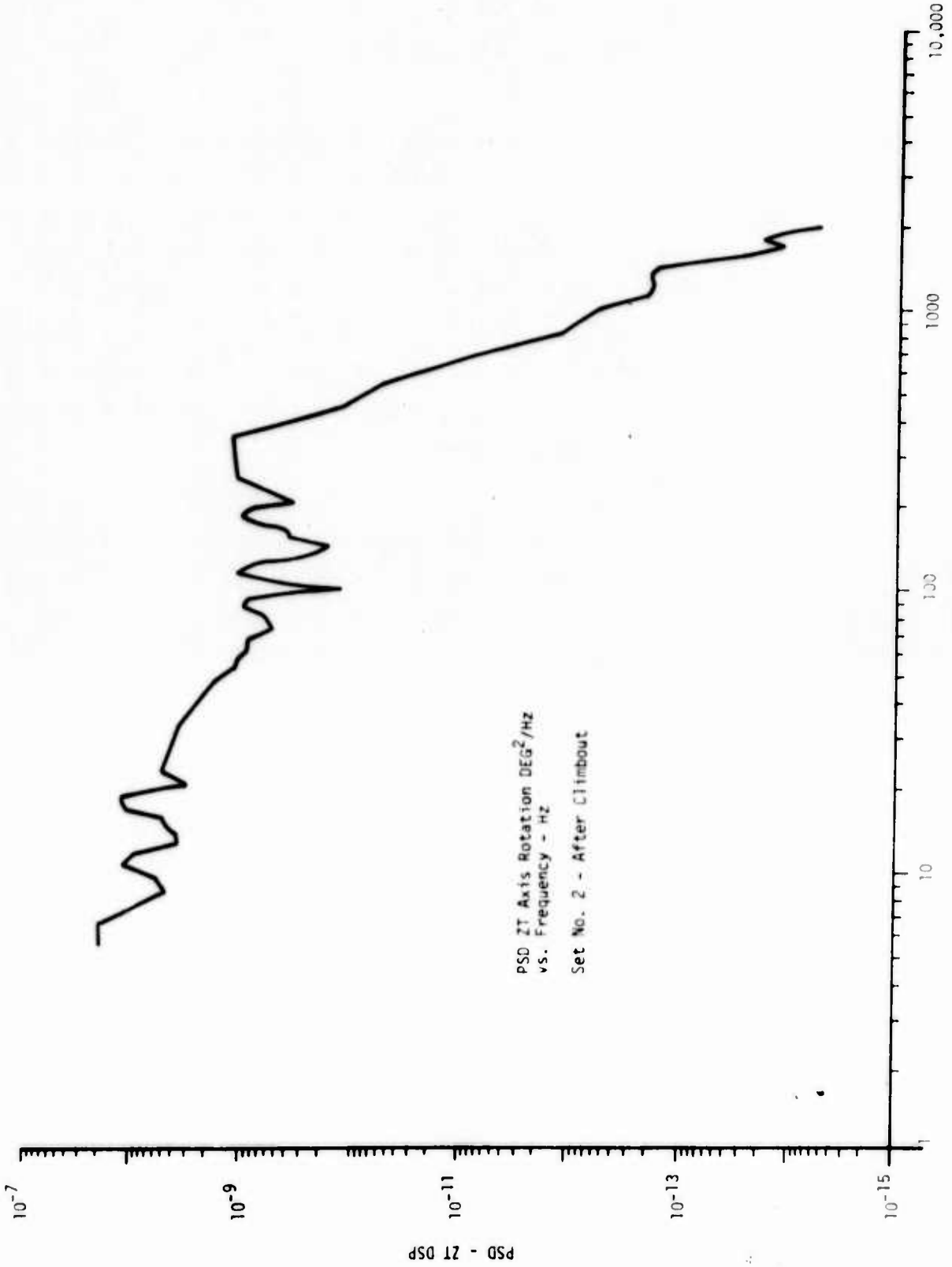

Figure 10. PSD of ZT Rotation - Set No. 2

SECTION III

POINTING SYSTEM EFFECTS

Several pointing system concepts could be used to collect incoming optical information or to direct an outgoing beam. The three generic types usually considered are the gimballed telescope, the single mirror heliostat, and the two-mirror coelostat. These are shown schematically in figure 11. The gimballed telescope has several relay mirrors to bring the beam into the expanding telescope when wide angular coverage is desired. The heliostat has simply the single mirror with the telescope mounted to the aircraft and has limited coverage in elevation. The coelostat has full coverage and the telescope mounted to the airframe, but is usually the largest installation.

The output optical elements of these systems are pointed in the desired direction using closed-loop control systems. The system configuration generally has a stabilization loop, usually gyroscope controlled, which has as its main function to keep the output optics following their commands in the face of disturbances such as windloads, dynamic torques, or friction. A target tracker is then used to form a closed tracking loop to keep the pointing system on target (figure 12).

Angular vibrations of the airframe can be directly coupled into the pointing system when a two-gimbal pointing system is used. Figure 13 shows the gimballed telescope system at a given elevation angle E_{LOS}. The component of the vehicle angular velocity ω_{V_X} is seen to have a component along the perpendicular to the line of sight. Thus, the vehicle motions would misdirect the beam. For the gimballed telescope, the stabilization system gyroscope on the telescope would sense this as a disturbance and try to remove it. For the heliostat system, the azimuth channel has the gyroscope on the azimuth gimbal, not the mirror. The mechanism for base motion coupling on the heliostat is the same as shown in figure 14. The gyroscope, however, would not sense the motion, and the tracking loop would have to remove the effect. The heliostat has another mechanism in which vehicle motions about the elevation axis cause the beam to be misdirected. Since the single mirror is stabilized about the elevation axis, one can see that if the incoming beam rotates the outgoing beam will move in the opposite direction. Thus, for vehicle motion ω_{V_Z}, the beam moves $-\omega_{V_Z}$. The control systems and the

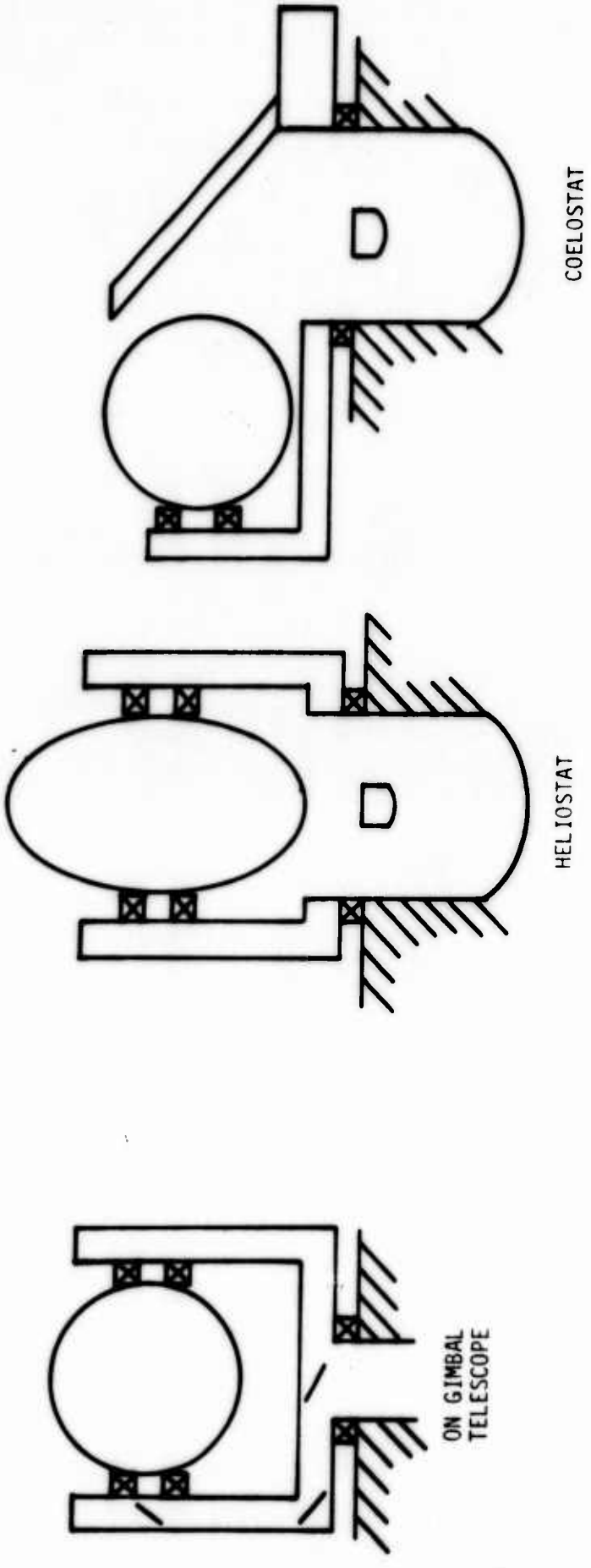

Figure 11. Various Beam Pointer Concepts

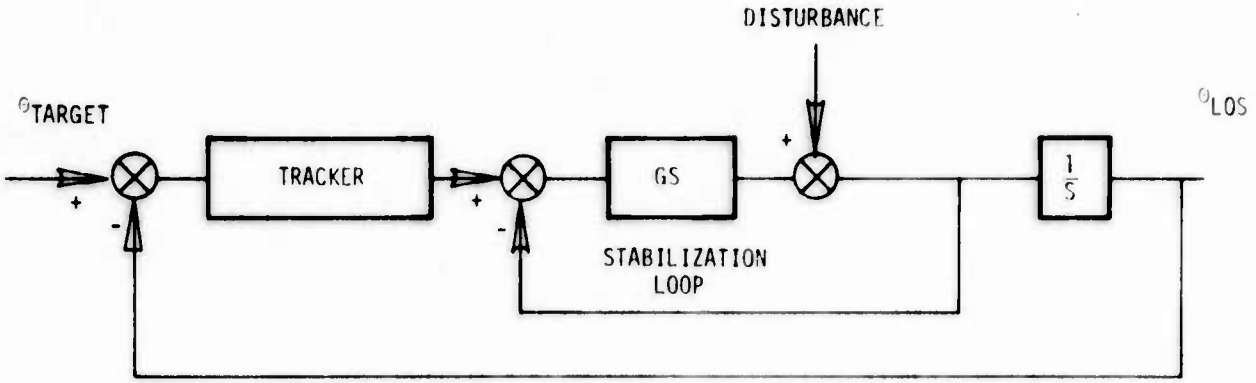

Figure 12. Typical Tracing Loop for Pointing System Control

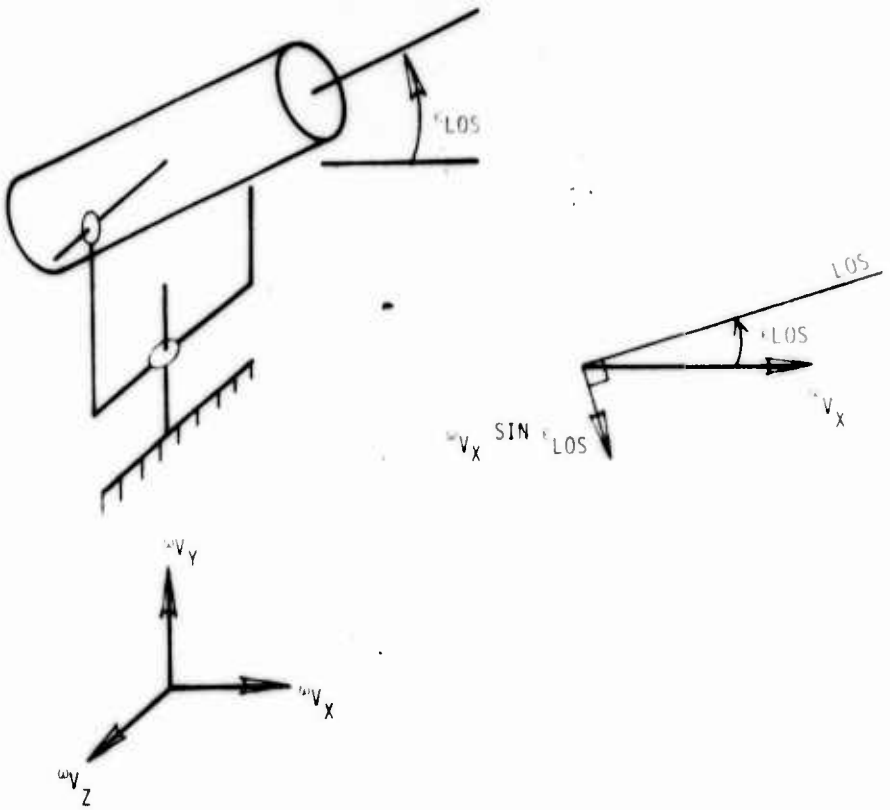

Figure 13. Base Motion Effect on Azimuth Axis - 2 Gimbal Telescope

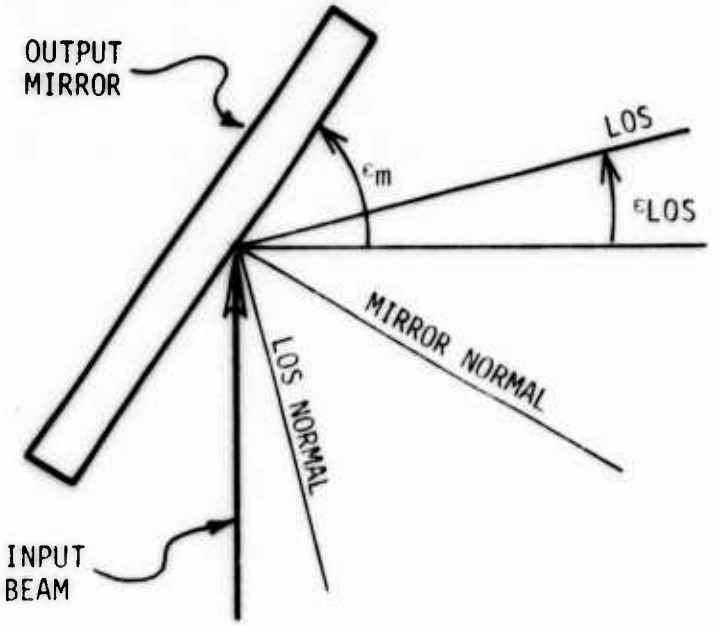

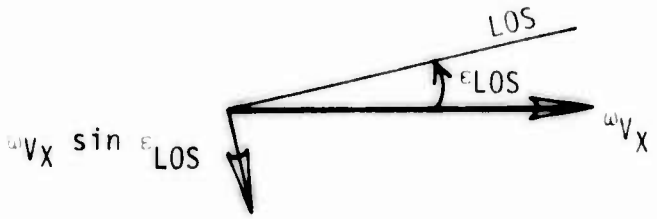

$$\varepsilon_{LOS} = 2\varepsilon_m - 90°$$

Figure 14. Base Motion Effect on Azimuth Axis Heliostat

mechanisms by which base motions enter as disturbances are shown in figure 15. For the heliostat, it is seen that the rejection of base motions must be accomplished by the tracking loop; whereas, for the gimballed telescope, the stabilization loop can be used to reject the base motion. The reason for this is that the heliostat generally does not have the azimuth gyro on the mirror, but it is usually placed on the azimuth gimbal. If it were placed on the mirror, the gain of the stabilization loop would be attenuated for most useful elevation angles and the ability to reject disturbances about the azimuth axis would be impaired. The coelostat, of course, could put the stabilization sensors on the elevation output mirror and retain the rejection capability of the stabilization loop.

The effect of base motion on the tracking stability of the heliostat control systems is

$$e = \frac{\omega_V \cdot 1/s}{1+GT} = \frac{\theta_V}{1+GT} \tag{1}$$

where e is the angular following error, GT is the forward loop gain of the tracking loop, and θ_V is the vehicle angular motion. The rms angular error is

$$e_{rms} = \left[\int_0^f \left| \frac{1}{1+GT} \right|^2 \Phi_{\theta_V} \, df \right]^{1/2} \tag{2}$$

where Φ_{θ_V} is the power spectral density of the vehicle angular motion.

For the control systems of the gimballed telescope and coelostat, the effect of vehicle motion on the tracking stability of the azimuth channel is

$$e = \frac{\theta_V}{[1+GS]\,[1+GT]} \tag{3}$$

where GS is the forward loop gain of the stabilization loop. The rms error angle is

$$e_{rms} = \left[\int_0^f \left| \frac{1}{1+GT} \right|^2 \left| \frac{1}{1+GS} \right|^2 \Phi_{\theta_V} \, df \right]^{1/2} \tag{4}$$

The effect of stabilization loop and tracking loop bandwidth on rejection of the measured base motion spectrum was investigated using a simple second order transfer function for the loops. The type chosen was

$$GS, GT = \frac{K}{S(S+\alpha)} \tag{5}$$

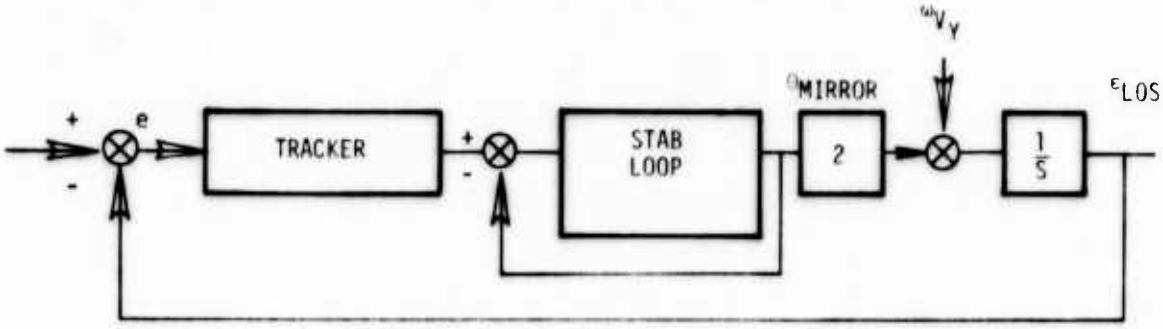

CONTROL SYSTEM - ELEVATION CHANNEL OF HELIOSTAT

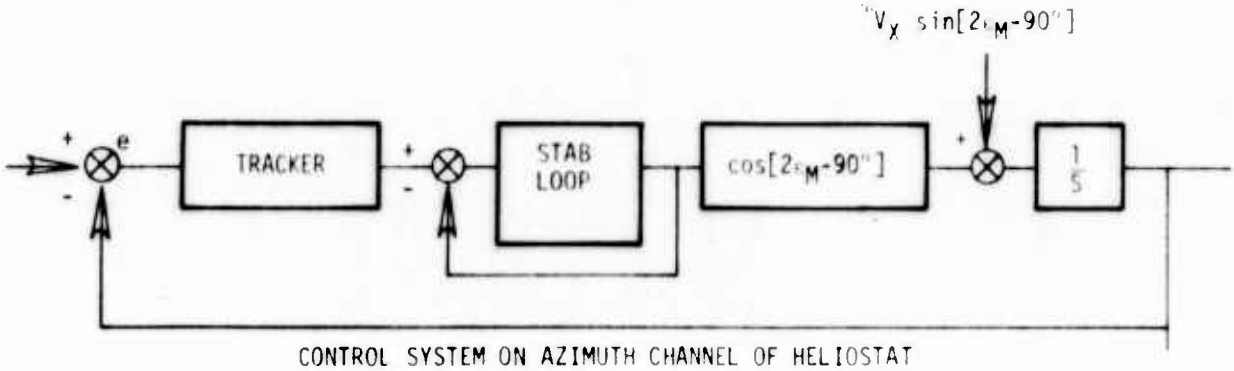

CONTROL SYSTEM ON AZIMUTH CHANNEL OF HELIOSTAT

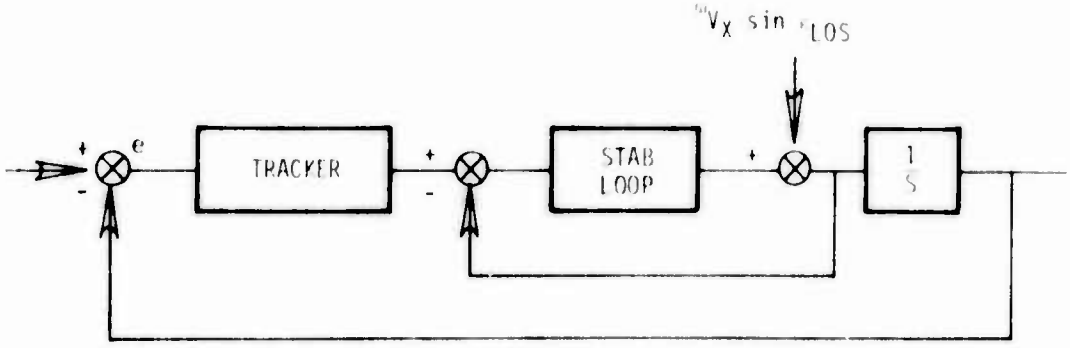

CONTROL SYSTEM - AZIMUTH CHANNEL OF GIMBALLED TELESCOPE

Figure 15. Control Systems for Pointing Systems

which would lead to closed loop response functions

$$\frac{GS}{1+GS}, \frac{GT}{1+GT} = \frac{1}{S^2/\omega_N{}^2 + 2\xi\ S/\omega_N + 1} \tag{6}$$

so that $K = \omega_N{}^2$, $\alpha = 2\xi\ \omega_N$.

The response of the gimballed telescope is determined primarily by the stabilization loop characteristics since its bandwidth must be higher than the track loop. The calculation, therefore, used only the rejection capability of the stabilization loop.

The shape of the rejection functions

$$\left|\frac{1}{1+GS}\right|^2$$

for $\omega_N = 2\pi 10$, $2\pi 200$, and $\xi = 0.7$ are shown in figures 16 and 17. At low frequencies the transmission is seen to be less than unity. In the midrange, the motion is amplified, and at high frequencies the motion is passed directly. The rms error angle for various tracking or stabilization loop bandwidths were calculated and are plotted in figure 18 using the angular power spectral density for γ_T from data set No. 2. The rms of the input motion is shown also. It is seen that even a bandwidth of 200 Hz does not appreciably lower the rms error angle.

The use of a more sophisticated tracking system and the use of a rotational vibration isolation system were investigated also. The more complex control system is shown in block diagram form in figure 19. This postulated system has a hydraulic drive and a gyroscope controlled stabilization system. The base motion rejection curves for just the stabilization portion and the total tracking loops are shown in figures 20 and 21. The stabilization loop is seen to amplify the base motion up to seven times in the 100-Hz range. This is due to the narrow gain margin of the stabilization loop. The tracking loop is seen to reject motion only for a small frequency interval.

The use of a rotational vibration isolation system would reduce the rotational environment seen by the pointing system. A second order isolator was postulated whose transmission is

$$G_{ISOLATOR} = \frac{1}{[(S/\nu)^2 + 2\xi_{IS}\ S/\nu + 1]} \tag{7}$$

where ν is the resonant frequency of the isolator. The rms error angle response is then calculated from

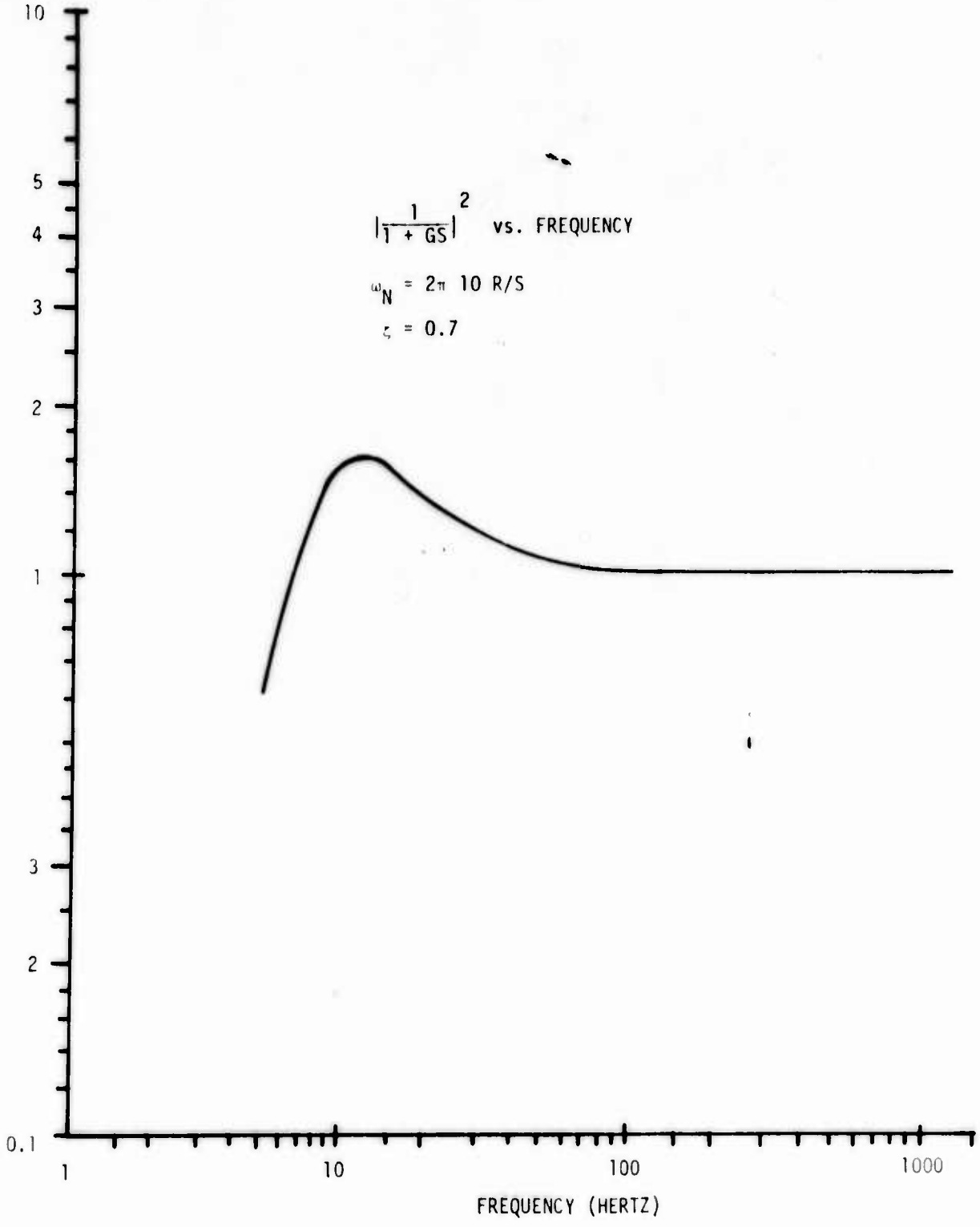

Figure 16. Rejection Function for Stabilization Loop - 10 Hz Bw

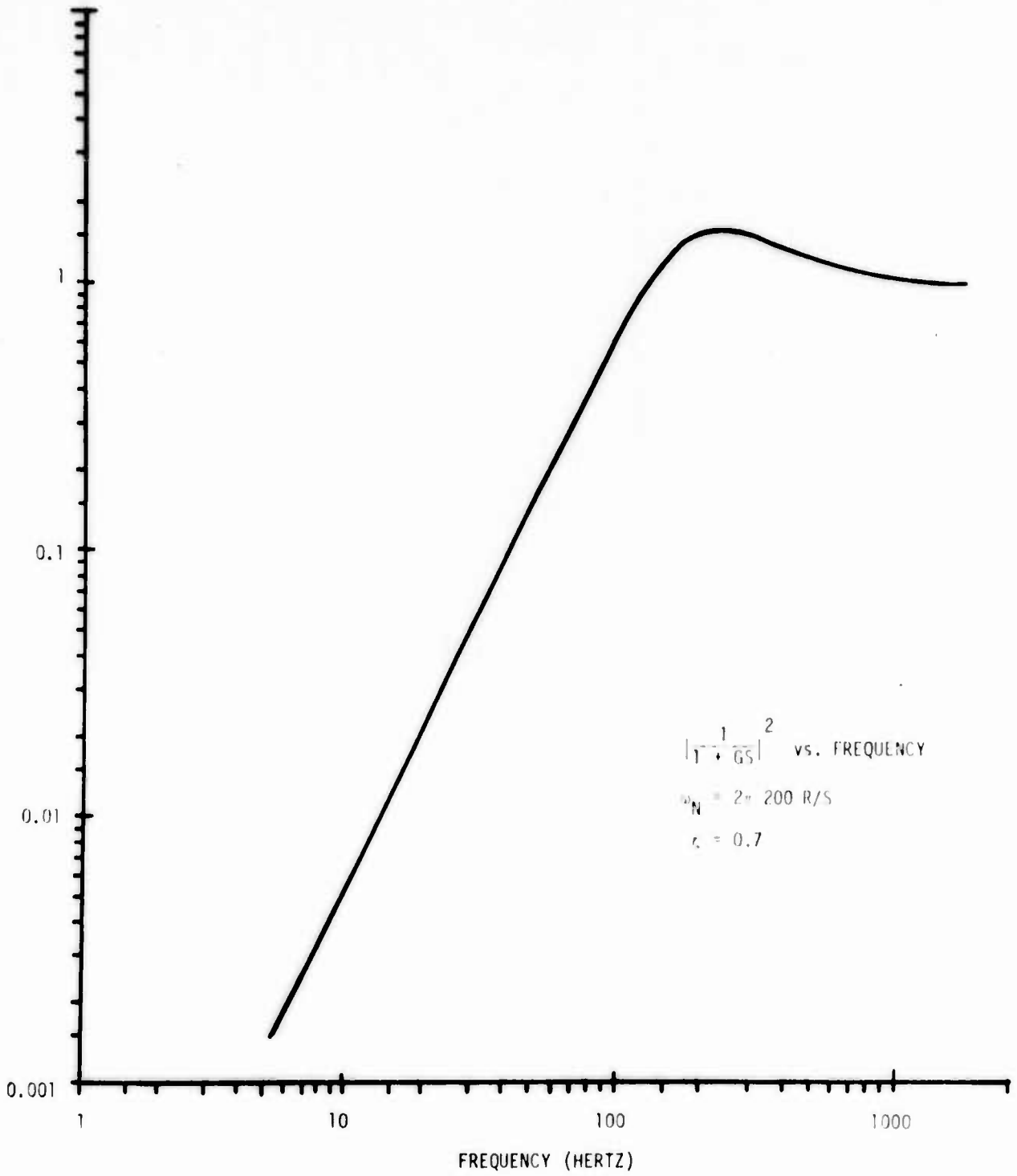

Figure 17. Rejection Function for Stabilization Loop - 200 Hz Bw

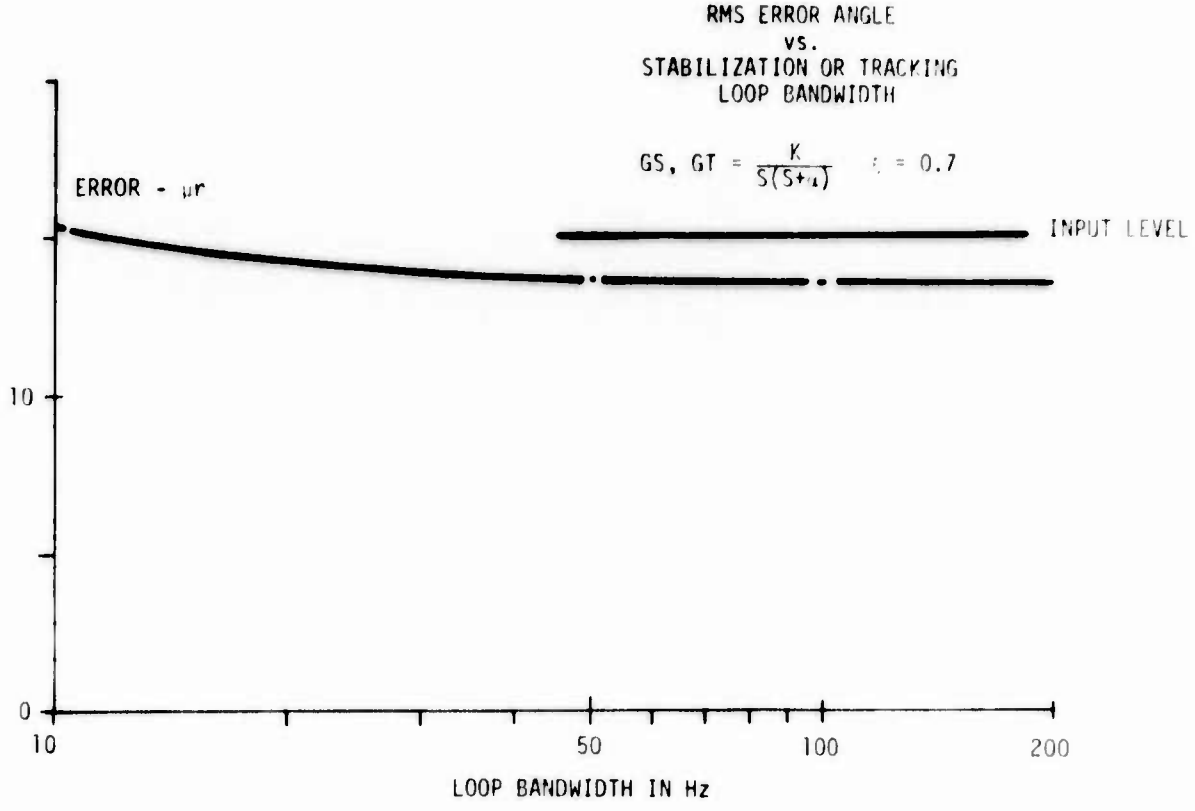

Figure 18. rms Error Angle for Various Loop Bandwidths

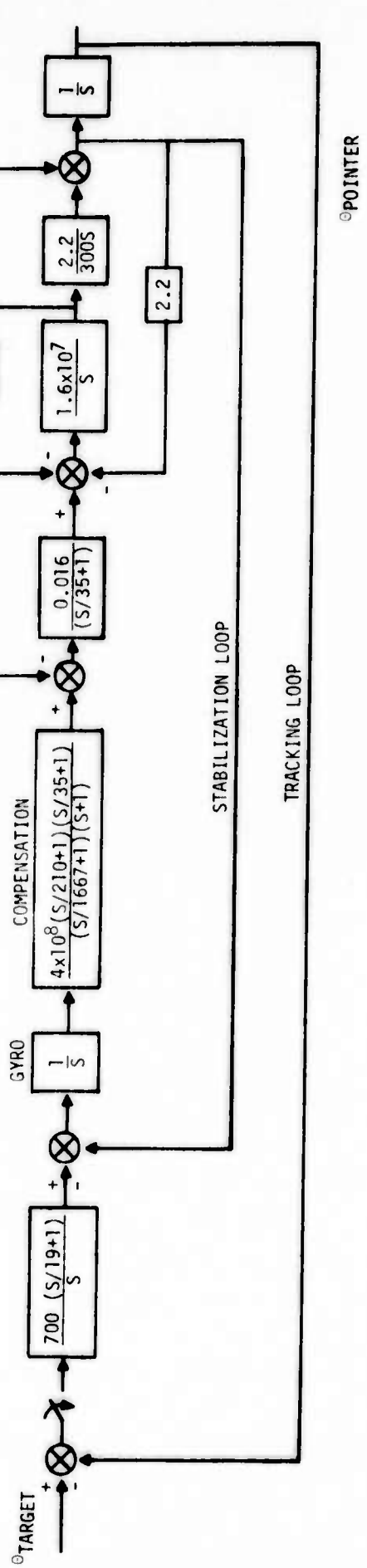

Figure 19. Reference Stabilization and Tracking System

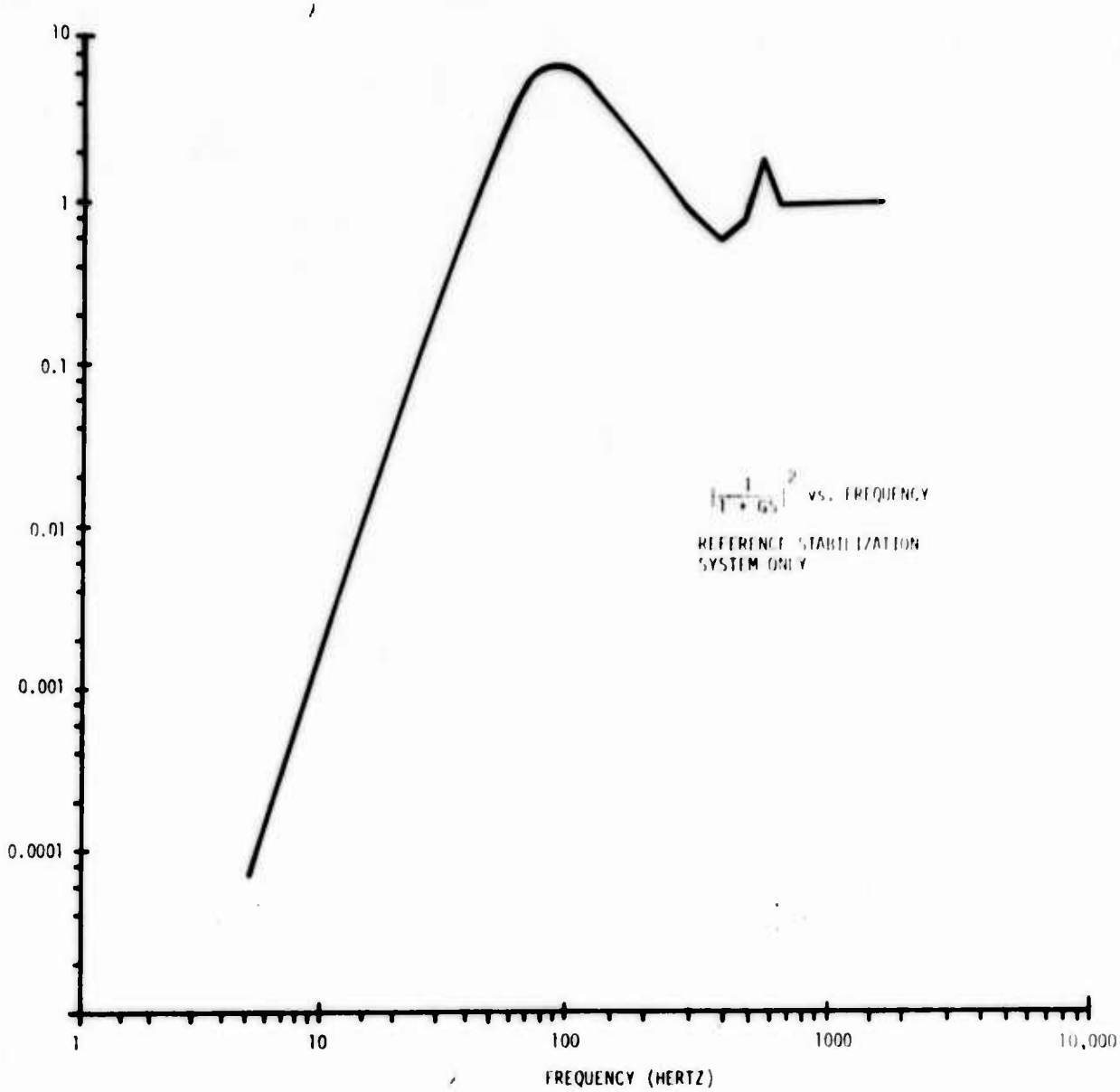

Figure 20. Rejection Function for Reference Stabilization Loop

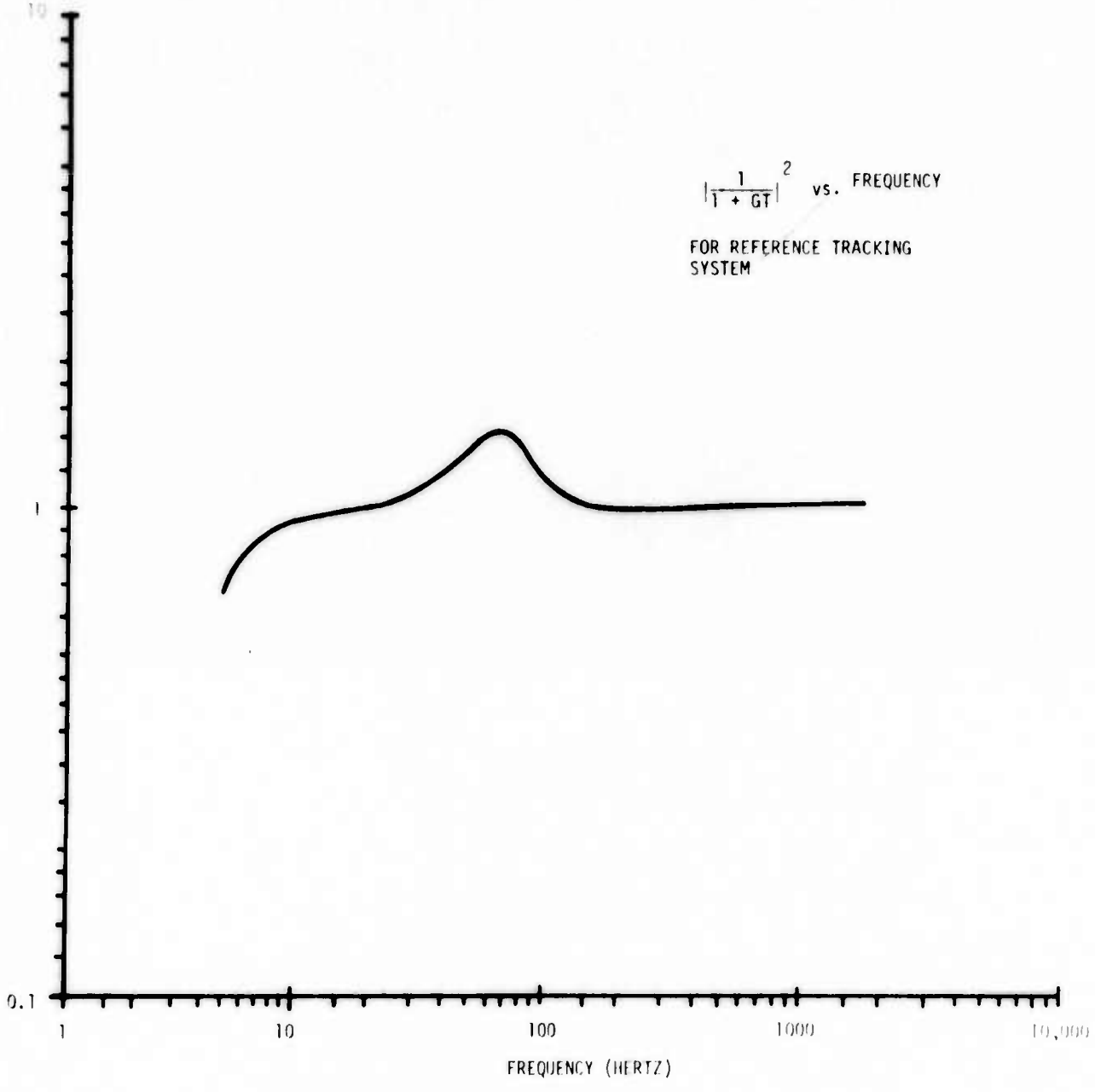

Figure 21. Rejection Function for Reference Tracking Loop

$$e_{rms} = \left[\int_0^f \left| \frac{1}{1+GS} \right|^2 \left| G_{ISOL} \right|^2 \Phi_{\theta_V} \, df \right] \tag{8}$$

The resulting pointing errors for the various tracking loops and for various isolator bandwidths and $\zeta_{IS} = 0.7$ are shown in figure 22. The data at 1000 Hz show the effect of not using an isolation system. The reduction in the pointing jitter using the isolator is quite apparent. The data shown here applies in total for the elevation error on the heliostat. The effect on the azimuth channels of the other pointing systems varies depending on the elevation or mirror angle. The data shown here are the maximum.

There are other techniques that could be used to reduce these errors. For the gimballed telescope, use of more gimbals would reduce the errors. For the heliostat, the use of a platform slaved mechanically to the line of sight, on which stabilization sensors would be mounted, could help to reduce the error (ref. 1). Measurement of the vehicle motion and feed forward compensation for the elevation and azimuth channels of the heliostat are also possibilities which have been investigated (ref. 2). Depending on the particular mission requirements, the system designer can pick from no compensation, no isolator, and low-bandwidth to the use of high-bandwidth loops and low-frequency isolation.

Three important factors have been omitted from this analysis that should be considered in the actual design of the pointing system, expecially for long-range, high-accuracy missions. The first is other noise sources in the system, expecially in the tracker itself. High-bandwidth tracking loops will respond to this noise and result in pointing jitter. The second factor is the complex dynamic torques which can rectify the line of sight (LOS) and vehicle motions to which the telescope will respond. These are generally not a problem until accuracies of fractions of an arc-second are considered. Treatment of these effects can be found in references 2 and 3. Thirdly, the design of a rotational isolator is a fairly sophisticated job, the critical issues being (1) ensuring that the center of mass and center of support are coincident, and (2) that the effective stiffness and damping of the linear elements used to make the isolator are closely matched. These are necessary so that the linear motions of the aircraft do not induce angular motions of the pointing system.

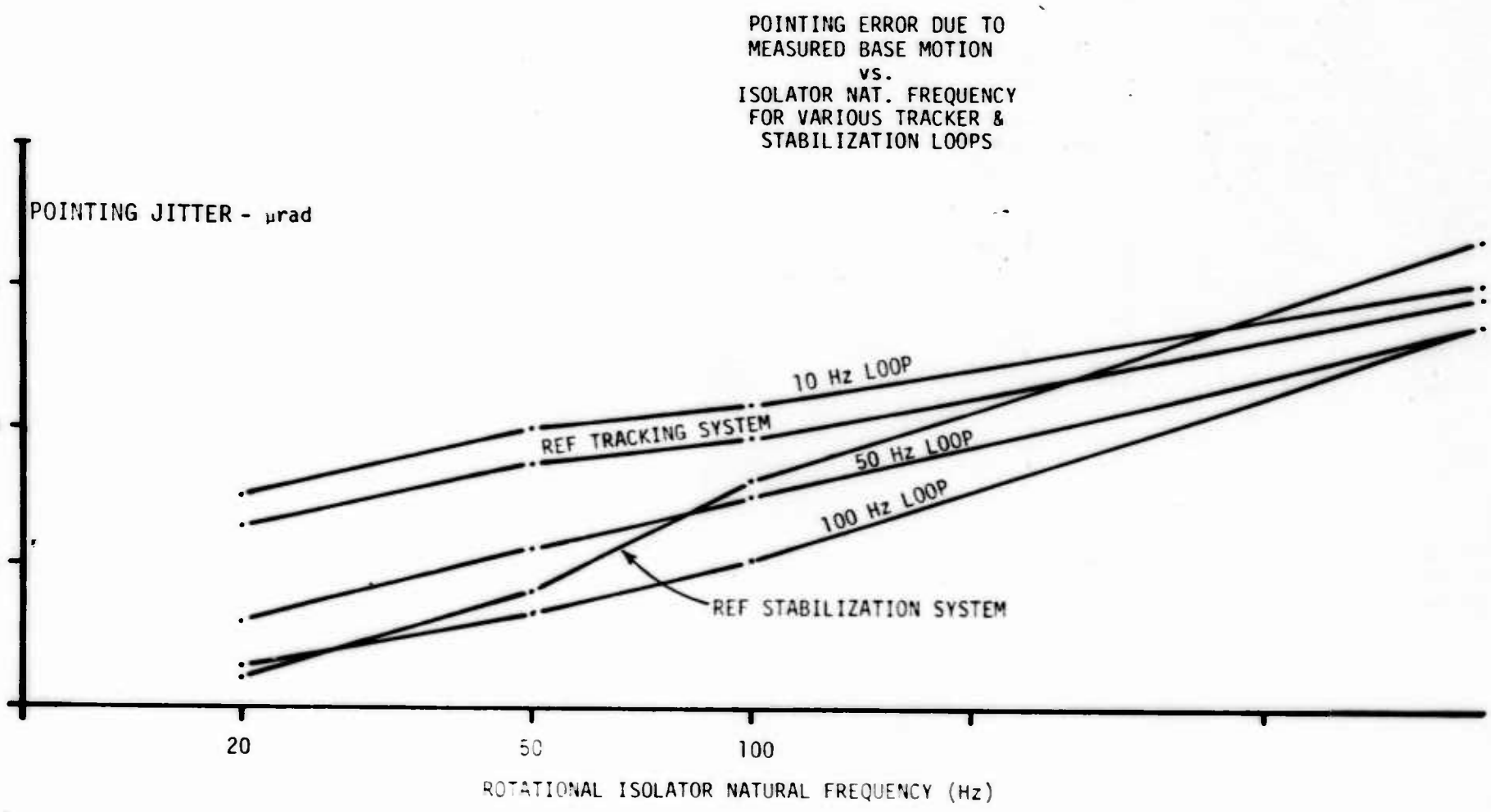

Figure 22. rms Pointing Error for Various Control Systems Versus Isolator Bandwidth

SECTION IV

MISALIGNMENT EFFECTS

The optical train under consideration consists of a collimated source, relay mirror, and reference plane (figure 2). When this train is mounted in a moving vehicle, it can be expected that each element will be angularly vibrating. Expressions will be derived to determine the relative angular motion between the ray coming from the source and the reference plane in terms of the absolute motions of each element. The situation where an autocollimator is at the source is also treated, so that the relative angular motion between transmitted and return ray can be determined.

There are four coordinate systems considered here. There are three that are nominally aligned to the vehicle roll, pitch, and yaw axes, located at and fixed to the source, relay mirror, and reference plane. A fourth coordinate system is fixed to the face of the relay mirror (figure 2).

The motions of the source have the components, with respect to an inertial frame: α about x, β about y, γ about z.

The motions of the frame at the location of the 45-degree mirror are: α_i, β_i, γ_i.

The motions of the reference plane at the top are: α_t, β_t, γ_t.

The small angular motions of the frame in the 45-degree mirror surface are: α_m, β_m, γ_m.

The motions of a propagated ray with respect to the reference plane consist of small misalignments, θ_z and θ_x, about the z and x axes of the reference plane. The angular power spectra of these relative motions in terms of the spectra of the absolute (inertial) angular motions of the source, 45-degree mirror and the reference plane are:

$$\Phi_{\theta_z} = \Phi_{\beta\beta} + \Phi_{\beta_i\beta_i} + \Phi_{\gamma_i\gamma_i} + \Phi_{\gamma_t\gamma_t} + 2\left\{\begin{matrix} -\mathrm{Re}\Psi_{\beta\beta_i} - \mathrm{Re}\Psi_{\beta\gamma_i} + \mathrm{Re}\Psi_{\beta\gamma_t} \\ +\mathrm{Re}\Psi_{\beta_i\gamma_t} - \mathrm{Re}\Psi_{\beta_i\gamma_i} - \mathrm{Re}\Psi_{\gamma_i\gamma_t} \end{matrix}\right\} \tag{9}$$

$$\Phi_{\theta_x} = \Phi_{\alpha\alpha} + 4\Phi_{\alpha_i\alpha_i} + \Phi_{\alpha_t\alpha_t} + \mathrm{Re}\Psi_{\alpha\alpha_t} - 4\mathrm{Re}\Psi_{\alpha\alpha_i} - 4\mathrm{Re}\Psi_{\alpha_i\alpha_t} \quad (10)$$

where

Φ_{ii} = power spectrum of angle i

Ψ_{mn} = cross spectrum between angle m and angle n

For the autocollimating situation, the angular misalignment of the incoming ray with respect to the transmitted ray consists of small angles ϕ_y and ϕ_x about the x and y axes in the source plane. The power spectra of the relative angular motions ϕ_y and ϕ_x in terms of the absolute (inertial) angular motion of the source, 45-degree mirror and the reference mirror plane are

$$\Phi_{\phi_y} = 4\Phi_{\theta_z} \quad (11)$$

$$\Phi_{\phi_x} = 4\Phi_{\phi_x} \quad (12)$$

The misalignment errors are seen to be a function of the motions of each element in the chain, as well as the correlation of the motions between elements. If the motions of each element are the same magnitude and correlated in phase, then the relative motions θ_z and θ_x, and thus ϕ_y and ϕ_x will be zero. For the data measured on the C-135, the rms values of the angles were determined using equations 9 and 10 and the results are summarized in table II. The rms angle is calculated from

$$\theta_{x_{rms}} = \int_0^f \Phi_{\theta_x}\, df \quad (13)$$

The spectra of these angles are shown in figures 23 to 26 which are from data set No. 2. The same data for the remaining flights are in appendix B.

1. RAY MOTION CAUSED BY VIBRATION

We start by referring motions to a fixed coordinate frame a. The ray source is angularly vibrating, and we wish to determine its motion with respect to the reference frame a. The b coordinate system is fixed in the source, and we have a vector $\bar{v}$ representing the emitting ray along the z_b axis (figure 27). The vector has components in the b frame:

TABLE II

RELATIVE ANGULAR MOTIONS OF THE THREE OPTICAL ELEMENTS

Angle	Data Set 1 After Lift Off	Data Set 2 During Climb Out	Data Set 3 Straight & Level	Data Set 4 Final Approach
	μr	μr	μr	μr
θ_x	14.3	8.2	4.6	6
θ_z	26.1	13.5	6	7.8
Φ_x	28.6	16.4	9.3	11
Φ_y	52	27	12	15.5

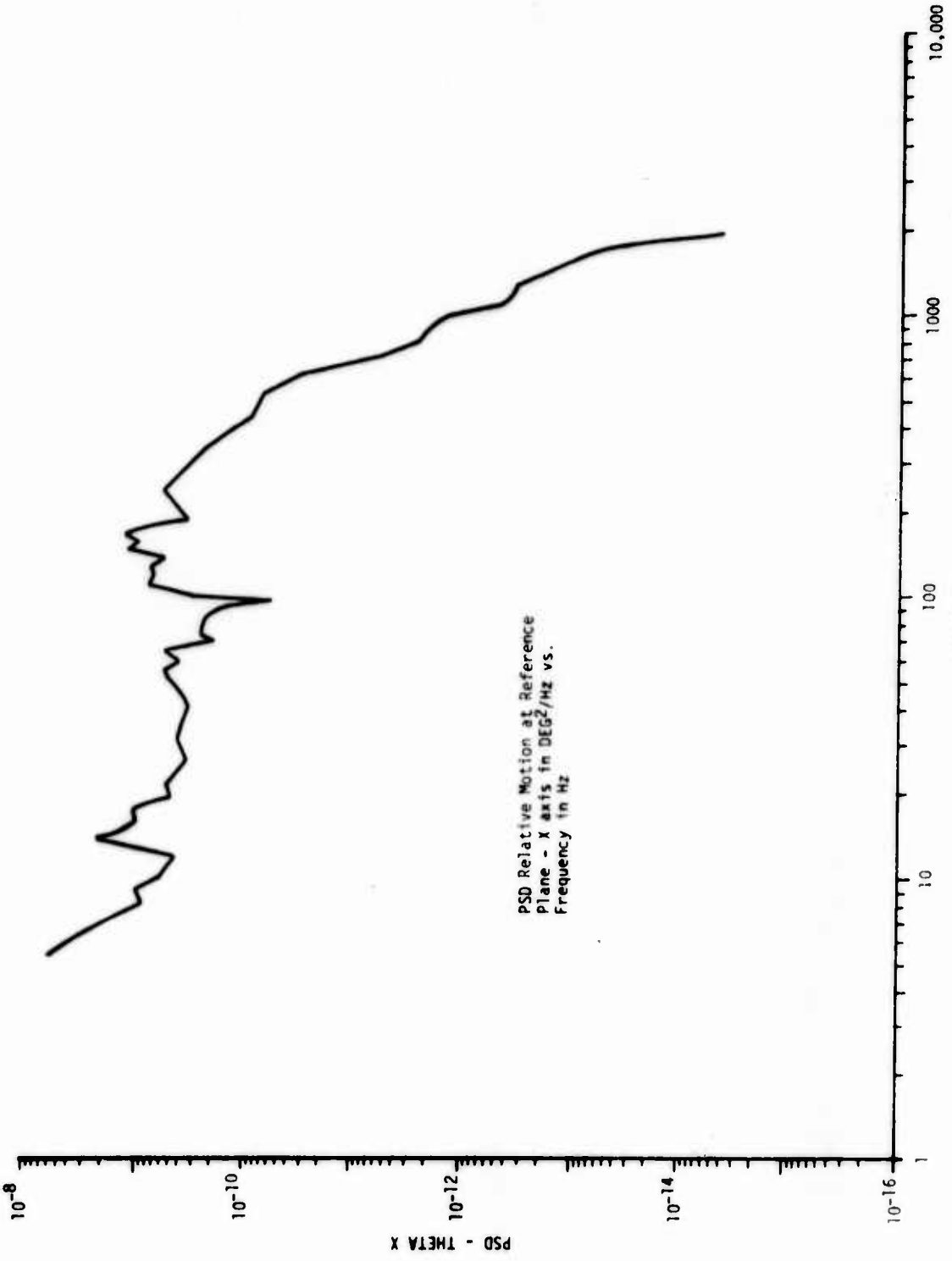

Figure 23. PSD Relative Motion at Reference Plane X Axis

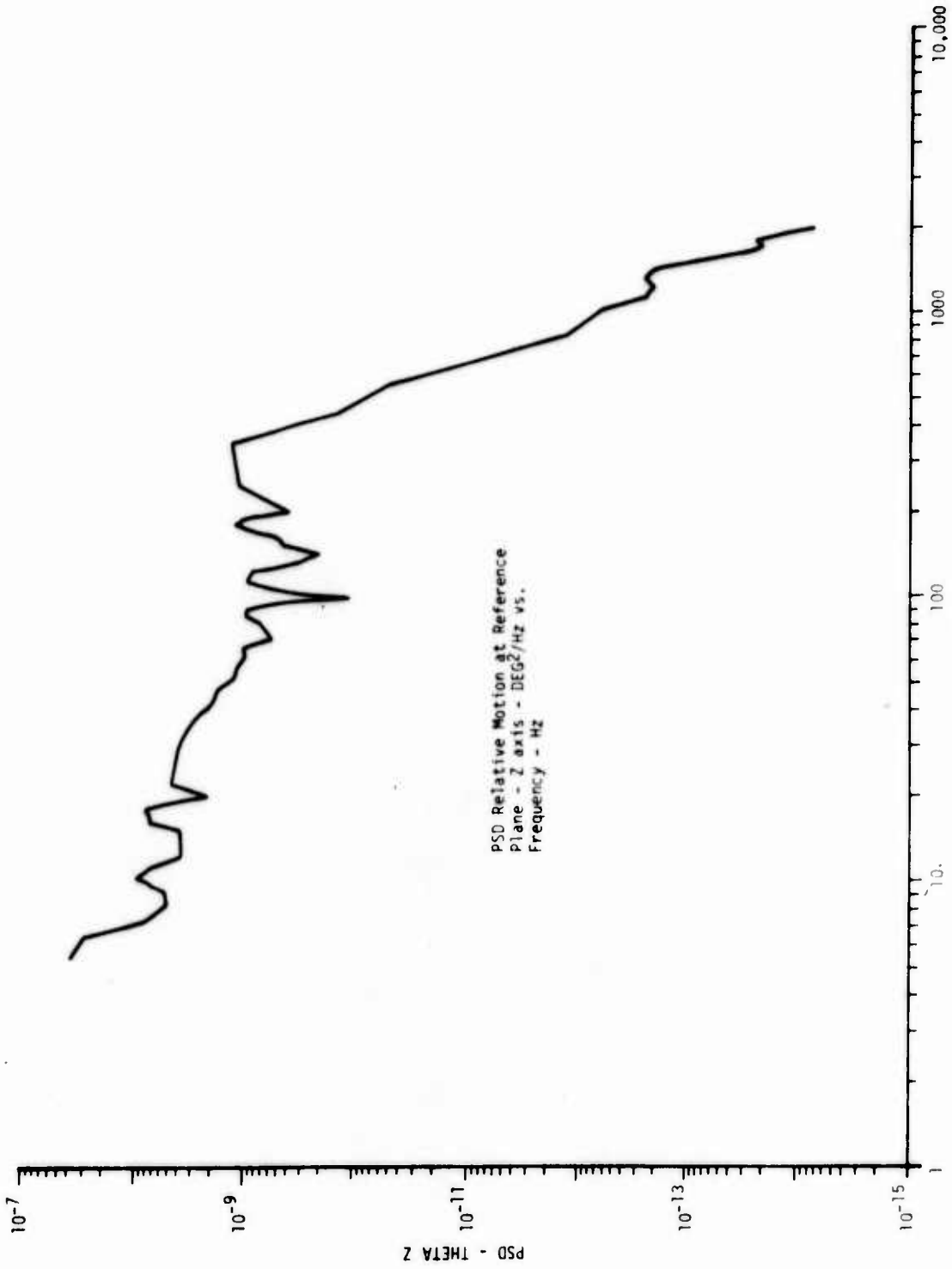

Figure 24. PSD Relative Motion at Reference Plane Z Axis

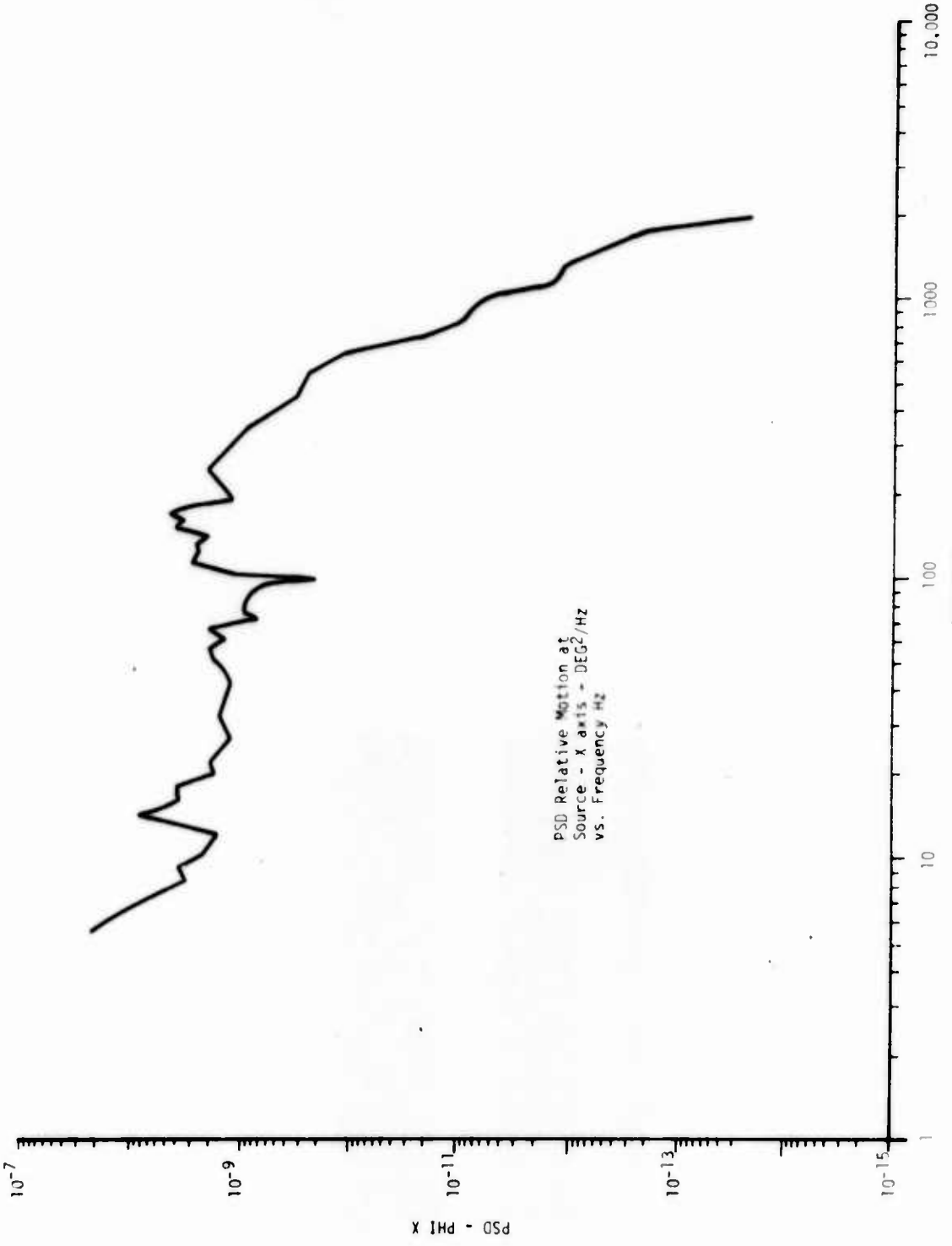

Figure 25. PSD Relative Motion at Source X Axis

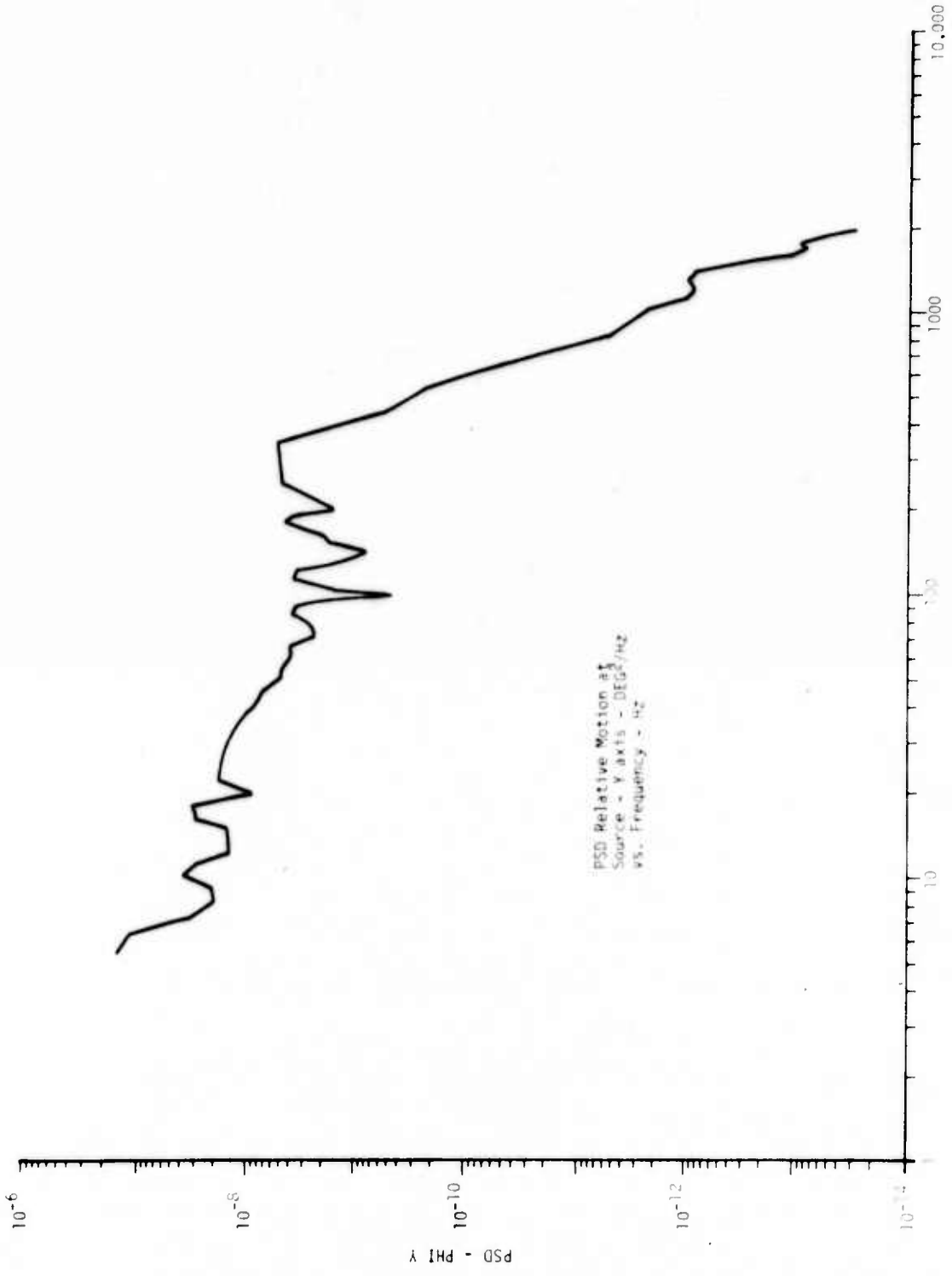

Figure 26. PSD Relative Motion at Source Y Axis

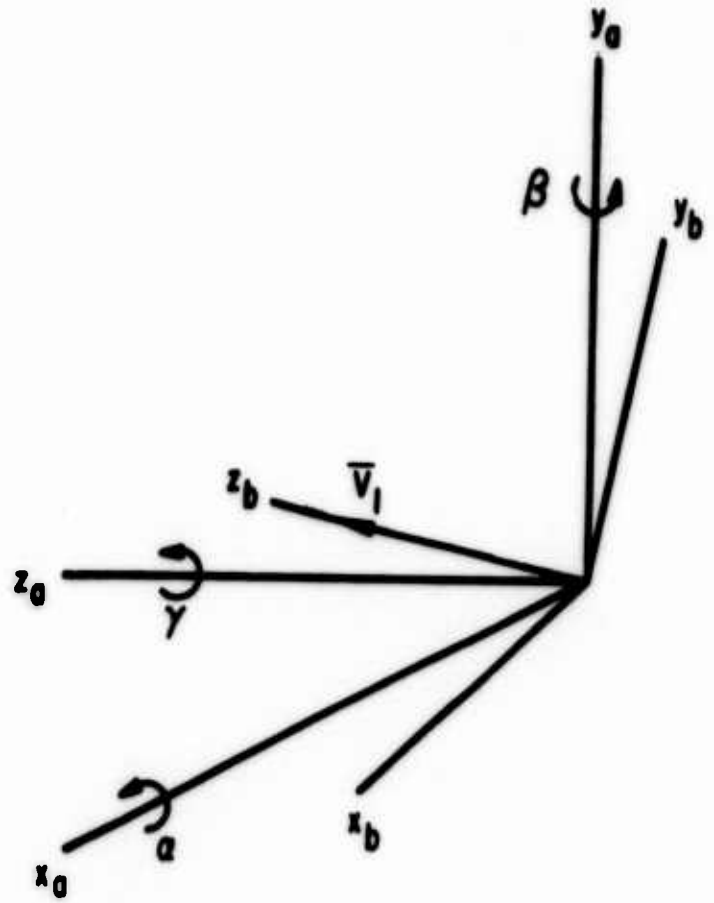

Figure 27. Orientation of the Source in the b Frame

$$\bar{v}_1^b = \begin{Bmatrix} 0 \\ 0 \\ v \end{Bmatrix} \tag{14}$$

Its components in the reference plane are determined from

$$\bar{v}_1^a = T_{ab}\, \bar{v}_1^b \tag{15}$$

where T_{ab} is the transformation matrix from the b frame to the a frame. Appendix A shows the derivation of the transformations used.

$$T_{ab} = T_{0\text{-}111} = \begin{bmatrix} 1 & -\gamma & \beta \\ \gamma & 1 & -\alpha \\ -\beta & \alpha & 1 \end{bmatrix} \tag{16}$$

The vector $\bar{v}_1$ now hits the relay mirror face, which contains the coordinate frame m. The general, the frame m is rotated with respect to the a frame by α'_m, β_m, and γ_m (figure 28). The vector $\bar{v}_1$ in the m frame is:

$$\bar{v}_1^m = T_{ma}\, \bar{v}_1^a \tag{17}$$

$$T_{ma} = \begin{bmatrix} \cos\gamma_m \cos\beta_m & \left[\begin{matrix}\cos\gamma_m \sin\beta_m \sin\alpha'_m \\ + \sin\gamma_m \cos\alpha'_m\end{matrix}\right] & \left[\begin{matrix}-\cos\gamma_m \cos\alpha'_m \sin\beta_m \\ + \sin\gamma_m \sin\alpha'_m\end{matrix}\right] \\ -\sin\gamma_m \cos\beta_m & \left[\begin{matrix}-\sin\gamma_m \sin\beta_m \sin\alpha'_m \\ + \cos\gamma_m \sin\alpha'_m\end{matrix}\right] & \left[\begin{matrix}\sin\gamma_m \sin\beta_m \cos\alpha'_m \\ + \cos\gamma_m \sin\alpha'_m\end{matrix}\right] \\ \sin\beta_m & -\cos\beta_m \sin\alpha'_m & \cos\beta_m \cos\alpha'_m \end{bmatrix} \tag{18}$$

Nominally $\alpha'_m = 45° + \alpha_m$, α_m, β_m, γ_m are small. Therefore,

$$\sin\alpha'_m = \frac{(1 + \alpha_m)}{\sqrt{2}} \qquad \cos\alpha'_m = \frac{(1 - \alpha_m)}{\sqrt{2}}$$

$$\cos\beta_m = \cos\gamma_m = 1 \qquad \sin\beta_m = \beta_m \qquad \sin\gamma_m = \gamma_m$$

$$T_{ma} \cong \begin{bmatrix} 1 & \frac{(\gamma_m + \beta_m)}{\sqrt{2}} & \frac{(\gamma_m - \beta_m)}{\sqrt{2}} \\ -\gamma_m & \frac{(1 - \alpha_m)}{\sqrt{2}} & \frac{(1 + \alpha_m)}{\sqrt{2}} \\ \beta_m & \frac{-(1 + \alpha_m)}{\sqrt{2}} & \frac{1(-\alpha_m)}{\sqrt{2}} \end{bmatrix} \tag{19}$$

The vector leaving the mirror is $\bar{v}_2$. The mirror has the property

$$\bar{v}_2^m = \begin{bmatrix} 1 & 0 & 0 \\ 0 & 1 & 0 \\ 0 & 0 & -1 \end{bmatrix} \bar{v}_1^m = M\, \bar{v}_1^m \tag{20}$$

$$\bar{v}_2^a = T_{am}\, \bar{v}_2^m \tag{21}$$

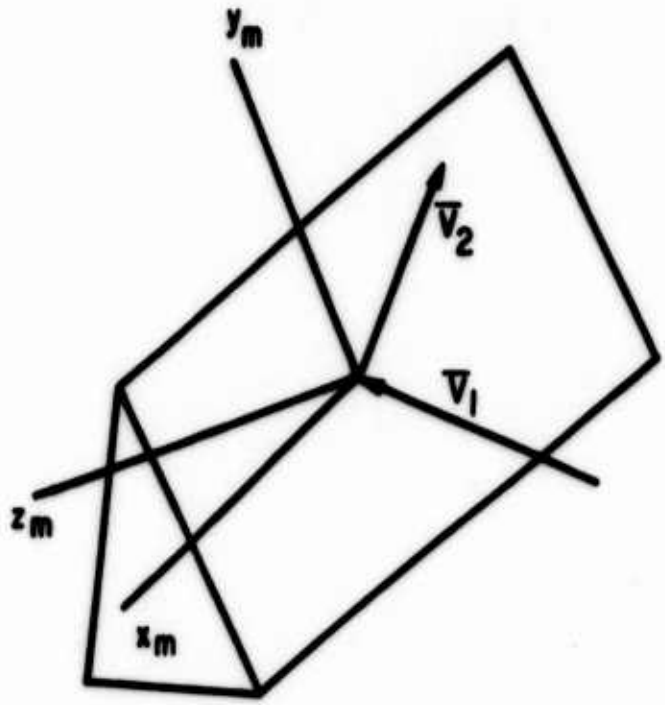

Figure 28. Coordinate Frame m on the Relay Mirror Face

$$T_{am} \cong \begin{bmatrix} 1 & -\gamma_m & \beta_m \\ \frac{(\gamma_m + \beta_m)}{\sqrt{2}} & \frac{(1 - \alpha_m)}{\sqrt{2}} & \frac{-(1 + \alpha_m)}{\sqrt{2}} \\ \frac{(\gamma_m - \beta_m)}{\sqrt{2}} & \frac{(1 + \alpha_m)}{\sqrt{2}} & \frac{(1 - \alpha_m)}{\sqrt{2}} \end{bmatrix} \tag{22}$$

The vector $\bar{v}_2$ is incident on the reference plane with a frame t fixed in it. For the situation where autocollimating is to be done (figure 29), this reference plane could also be a mirror.

$$\bar{v}^t = T_{ta}\,\bar{v}^a,\ T_{ta} = \begin{bmatrix} 1 & \gamma_t & -\beta_t \\ -\gamma_t & 1 & \alpha \\ \beta_t & -\alpha_t & 1 \end{bmatrix} \tag{23}$$

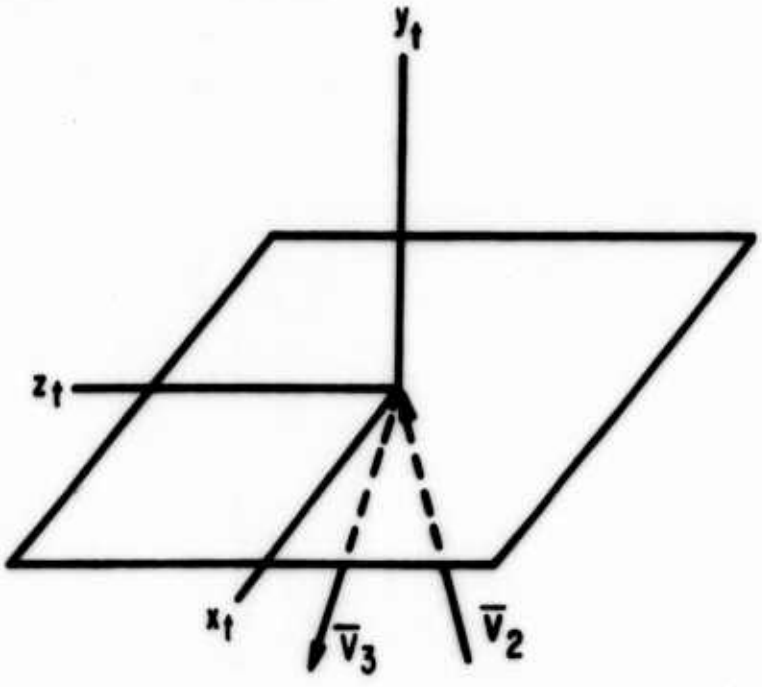

Figure 29. Coordinate Frame t in the Reference Plane

The motion of the vector $\bar{v}_2$ at the mirror frame in terms of the vector $\bar{v}_1^b$ is

$$\bar{v}_2^t = T_{ta}\, T_{am}\, M\, T_{ma}\, T_{ab}\, \bar{v}^b \tag{24}$$

We thus start with a vector

$$\bar{v}^b = \begin{Bmatrix} 0 \\ 0 \\ 1 \end{Bmatrix} v \tag{25a}$$

and transform through each transformation matrix.

After the first coordinate system the vector is

$$\begin{Bmatrix} \beta \\ -\alpha \\ 1 \end{Bmatrix} V \tag{25b}$$

and through the 45-degree mirror

$$\begin{Bmatrix} \left(\beta - \frac{2}{\sqrt{2}}\beta_m\right) \\ 1 \\ \left(-\alpha + 2\alpha_m\right) \end{Bmatrix} V \tag{25c}$$

and at the top mirror

$$\begin{Bmatrix} \left(\beta - \frac{2}{\sqrt{2}}\beta_m + \gamma_t\right) \\ 1 \\ \left(-\alpha + 2\alpha_m - \alpha_t\right) \end{Bmatrix} V \tag{25d}$$

Since we expect only the y component, the other two can be thought of as arising from misalignments about the x and y axes

$$\theta_z = -\left(\beta - 2\beta_m\sqrt{2} + \gamma_t\right)$$

$$\theta_x = -\alpha + 2\alpha_m - \alpha_t \tag{26}$$

The angular vibration measurements at the 45-degree mirror are not made in the m frame but in the i frame (figure 2). The quantities in the mirror frame, α_m, β_m, and γ_m are related to the measured quantities (assumed small), as

$$\begin{Bmatrix} \alpha_m \\ \beta_m \\ \gamma_m \end{Bmatrix} = T_{mi} \begin{Bmatrix} \alpha_i \\ \beta_i \\ \gamma_i \end{Bmatrix} \tag{27}$$

where

$$T_{mi} = T_{0-1} = \begin{bmatrix} 1 & 0 & 0 \\ 0 & \frac{1}{\sqrt{2}} & \frac{1}{\sqrt{2}} \\ 0 & \frac{-1}{\sqrt{2}} & \frac{1}{\sqrt{2}} \end{bmatrix}$$

Thus

$$\alpha_m = \alpha_i$$

$$\beta_m = \frac{1}{\sqrt{2}} \left(\beta_i + \gamma_i\right)$$

$$\gamma_m = \frac{1}{\sqrt{2}} \left(-\beta_i + \gamma_i\right) \tag{28}$$

and

$$\theta_z = \beta - \beta_i - \gamma_i + \gamma_t$$

γ

$$\theta_x = -\alpha + 2\alpha_i - \alpha_t \tag{29}$$

2. ERROR USING AUTOCOLLIMATOR

If we reflect back at the mirror t, we get a new vector $\bar{v}_3$

$$\bar{v}_3^t = \begin{bmatrix} 1 & 0 & 0 \\ 0 & -1 & 0 \\ 0 & 0 & 0 \end{bmatrix} \bar{v}_2^t = M' \bar{v}_2^t$$

This vector in the reference frame a is

$$\bar{v}_3^a = T_{at} \bar{v}_3^t \qquad T_{at} \cong \begin{bmatrix} 1 & -\gamma_t & \beta_t \\ \gamma_t & 1 & -\alpha_t \\ -\beta_t & \alpha_t & 1 \end{bmatrix} \tag{30}$$

This vector in the m frame is

$$\bar{v}_3^m = T_{ma} \bar{v}_3^a \tag{31}$$

This leaves the 45-degree mirror as vector $\bar{v}_4$

$$\bar{v}_4^m = M \bar{v}_3^m \tag{32}$$

and in the a frame

$$\bar{v}_4^a = T_{am} \bar{v}_4^m \tag{33}$$

Comparing to the b frame from which the vector originated

$$\bar{v}_4^b = T_{ba}\,\bar{v}_4^a \qquad T_{ba} \cong \begin{bmatrix} 1 & \gamma & -\beta \\ -\gamma & 1 & \alpha \\ \beta & \alpha & 1 \end{bmatrix} \tag{34}$$

We now examine the transmission from $\bar{v}_1^b$ to $\bar{v}_4^b$:

$$\bar{v}_4^b = T_{ba}\left(T_{am}\,M\,T_{ma}\right)\,T_{at}M'\,\bar{v}_2^t \tag{35a}$$

The vector $\bar{v}_2^t$ was shown in 25d. The new vector $\bar{v}_4^b$ becomes

$$\times\, M', \begin{Bmatrix} \left(\beta - \frac{2\beta_m}{\sqrt{2}} + \gamma_t\right) \\ -1 \\ -\alpha + 2\alpha_m - \alpha_t \end{Bmatrix} \tag{35b}$$

$$\times\, T_{at}, \begin{Bmatrix} \left(\beta - \frac{2\beta_m}{\sqrt{2}} + 2\gamma_t\right) \\ -1 \\ -\alpha + 2\alpha_m - 2\alpha_t \end{Bmatrix} \tag{35c}$$

$$\times \left(T_{am}\,M\,T_{ma}\right), \begin{Bmatrix} \left(\beta - \frac{4\beta_m}{\sqrt{2}} + 2\gamma_t\right) \\ -\alpha + 4\alpha_m - 2\alpha_t \\ -1 \end{Bmatrix} \tag{35d}$$

$$\times T_{ba'} \left\{ \begin{bmatrix} \left(2\beta - \frac{4\beta_m}{\sqrt{2}} + 2\gamma_t\right) \\ -2\alpha - 2\alpha_t + 4\alpha_m \\ \\ -1 \end{bmatrix} \right. \tag{35e}$$

At the autocollimator the angles due to frame motions are

$$\phi_y = -\left(2\beta - \frac{4\beta_m}{\sqrt{2}} + 2\gamma_t\right) \tag{36}$$

$$\phi_x = -\left(-2\alpha_t + 4\alpha_m - 2\alpha\right) \tag{37}$$

In terms of the i-frame measurements:

$$\phi_y = -\left(2\beta - 2\beta_i - 2\gamma_i + 2\gamma_t\right) = 2\theta_z \tag{38}$$

$$\phi_x = -\left(-2\alpha + 4\alpha_i - 2\alpha_t\right) = 2\theta_x \tag{38}$$

3. POWER SPECTRA

We wish to determine the power spectrum of the quantities θ_z, θ_x, ϕ_y, and ϕ_x. We determine first the autocorrelation function:

$$\overline{\theta_z(t)\theta_z(t+\tau)} = E\left[\left(\beta - \beta_i - \gamma_i + \gamma_t\right)\left(\beta(\tau) - \beta_i(\tau) - \gamma_i(\tau) + \gamma_t(\tau)\right)\right]$$

$$= E\left[\beta \cdot \beta(\tau) + \beta_i \cdot \beta_i(\tau) + \gamma_i \cdot \gamma_i(\tau) + \gamma_t \cdot \gamma_t(\tau)\right]$$

$$+ E\left[-\beta \cdot \beta_i(\tau) - \beta_i \cdot \beta(\tau) - \beta \cdot \gamma_i(\tau) - \gamma_i \cdot \beta(\tau)\right]$$

$$+ E\left[\beta \cdot \gamma_t(\tau) + \gamma_t \cdot \beta(\tau) + \beta_i \cdot \gamma_i(\tau) + \gamma_i \cdot \beta_i(\tau)\right]$$

$$+ E\left[-\beta_i \cdot \gamma_t(\tau) - \gamma_t \cdot \beta_i(\tau) - \gamma_i \cdot \gamma_t(\tau) - \gamma_t \cdot \gamma_i(\tau)\right] \tag{39}$$

$$\overline{\theta_z(t)\theta_z(t+\tau)} = R_{\theta_z\theta_z} = R_{\beta\beta} + R_{\beta_i\beta_i} + R_{\gamma_i\gamma_i} + R_{\gamma_t\gamma_t}$$

$$- \left(R_{\beta\beta_i}(\tau) + R_{\beta_i\beta}(\tau)\right) - \left(R_{\beta\gamma_i}(\tau) + R_{\gamma_i\beta}(\tau)\right)$$

$$+ \left(R_{\beta\gamma_t}(\tau) + R_{\gamma_t\beta}(\tau)\right) + \left(R_{\beta_i\gamma_i}(\tau) + R_{\gamma_i\beta_i}(\tau)\right)$$

$$- \left(R_{\beta_i\gamma_t}(\tau) + R_{\gamma_t\beta_i}(\tau)\right) - \left(R_{\gamma_i\gamma_t}(\tau) + R_{\gamma_t\gamma_i}(\tau)\right) \qquad (40)$$

where

R_{ii} = autocorrelation function

R_{ij} = cross correlation function

Transforming each correlation function into a spectral density, we obtain equations 9 and 10:

$$\Phi_{\theta_z} = \Phi_{\beta\beta} + \Phi_{\beta_i\beta_i} + \Phi_{\gamma_i\gamma_i} + \Phi_{\gamma_t\gamma_t}$$

$$+ 2\left[-\mathrm{Re}\Psi_{\beta\beta_i} - \mathrm{Re}\Psi_{\beta\gamma_i} + \mathrm{Re}\Psi_{\beta\gamma_t} + \mathrm{Re}\Psi_{\beta_i\gamma_i} - \mathrm{Re}\Psi_{\beta_i\gamma_t} - \mathrm{Re}\Psi_{\gamma_i\gamma_t}\right]$$

$$\Phi_{\theta_x} = \Phi_{\alpha\alpha} + 4\Phi_{\alpha_i\alpha_i} + \Phi_{\alpha_t\alpha_t} + 2\mathrm{Re}\Psi_{\alpha\cdot\alpha_t} - 4\mathrm{Re}\Psi_{\alpha\cdot\alpha_i} - 4\mathrm{Re}\Psi_{\alpha_i\alpha_t}$$

where

Φ = power spectral density

Ψ = cross spectral density

From equation 38, we obtain equations 11 and 12.

$$\Phi_{\phi_y} = 4\Phi_{\theta_z}$$

$$\Phi_{\phi_x} = 4\Phi_{\theta_x}$$

SECTION V

EQUIPMENT DESCRIPTION

The basic device used to make the angular velocity measurement is called an angular differencing integrating accelerometer (ADA) and is manufactured by the General Electric Corp. Its original task was to help stabilize inertial guidance platforms. The device is a floated torsional pendulum with a velocity pickoff. Above the natural frequency of the torsional pendulum, which is approximately 1 Hz, the pendulum tends to remain fixed in inertial space. The angular motion of the case about the pendulum axis above 1 Hz thus generates a voltage proportional to the angular velocity with respect to an inertial coordinate system. A complete description of the device can be found in reference 4.

The ADAs were mounted on blocks, attached to plates and mounted to the aircraft. The blocks were heated to approximately 55°C, the floatation temperature of the device. The rear installation of the two ADAs is shown in figure 30. The second floor installation at station 409 is shown in figure 31. The installation at the top of the fuselage is shown in figure 32. The mounting plate here fills the opening of a dome that normally has a plexiglass plate.

The ADA mounted on their blocks were calibrated at the General Electric Company, Schenectady Instrumentation Service. The ADAs were mounted at the pivot of a 24-inch fulcrum driven at one end with an electrodynamic shaker. The amplitude of the motion was measured with a calibrated microscope. The calibration was conducted from 1 Hz to 1000 Hz, which represented the limitation of the shaker. The results of the calibrations are shown in figures 33 to 40. The units are in mV rms/rad/sec peak-to-peak. The response is seen to be fairly flat to 1000 Hz. Previous experience has shown that the devices are flat to 2000 Hz, limited only by the mechanical resonances of the mounting blocks or by the ability to generate the motion (ref 5).

The ADAs outputs were amplified using a simple operational amplifier and recorded on an FM tape recorder. The performance was checked in flight using an oscillograph. A calibration source was switched in to calibrate the recording system before each flight. The polarity of each sensor was determined by physically rotating the block about each axis.

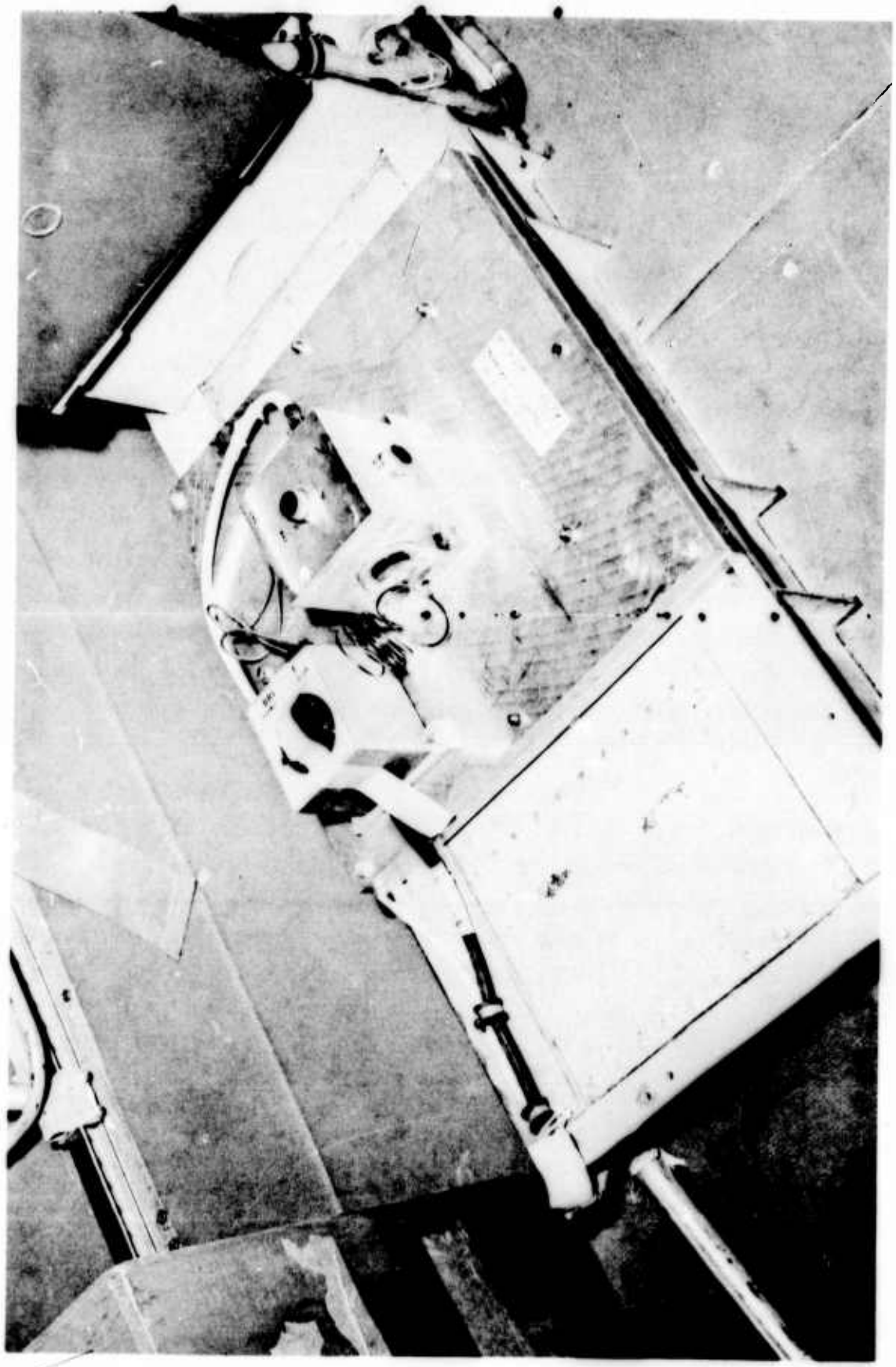

Figure 30. Floor Installation of Sensors at FS.554

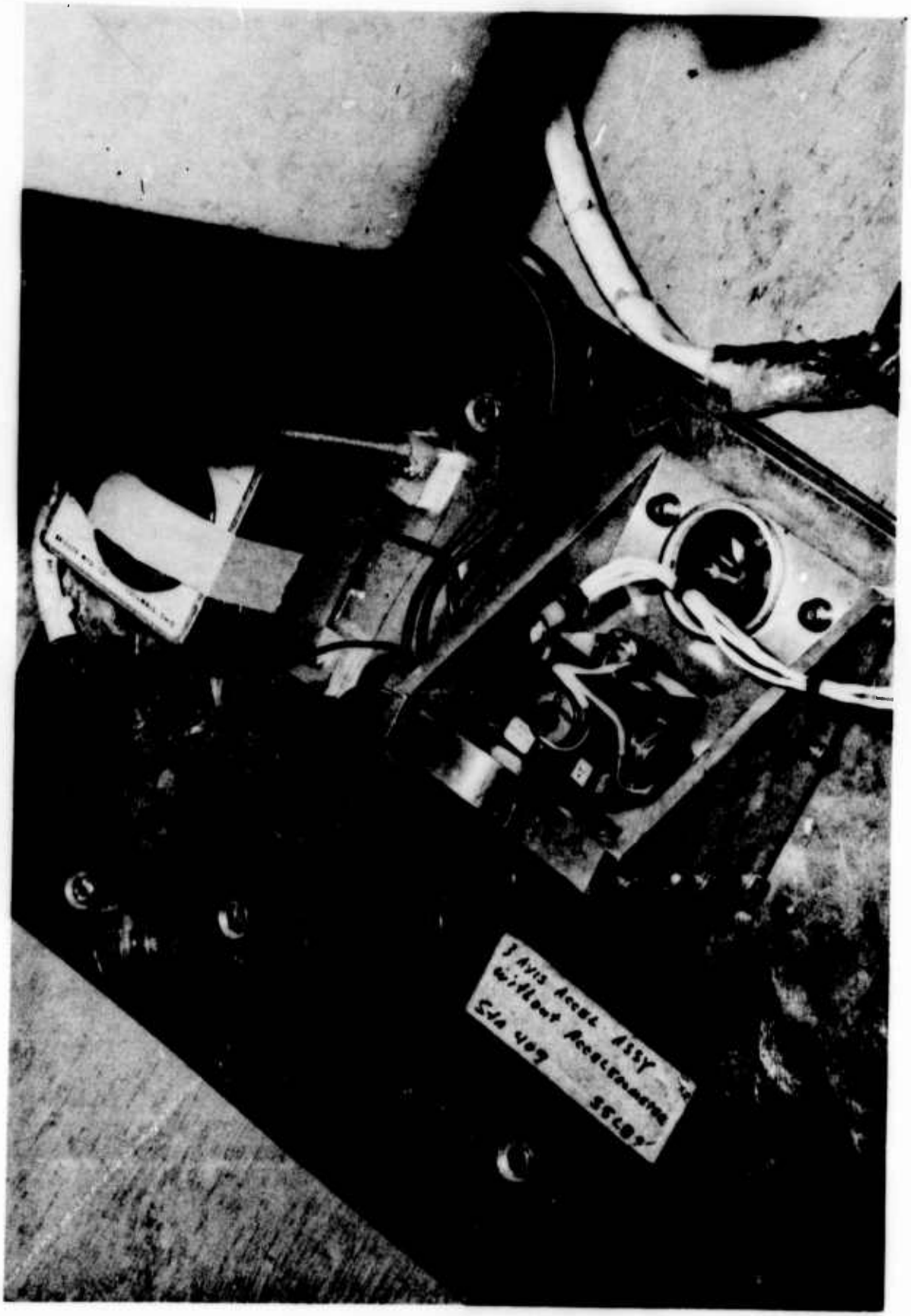

Figure 31. Floor Installation of Sensors at FS.409

Figure 32. Ceiling Installation of Sensors at FS.409

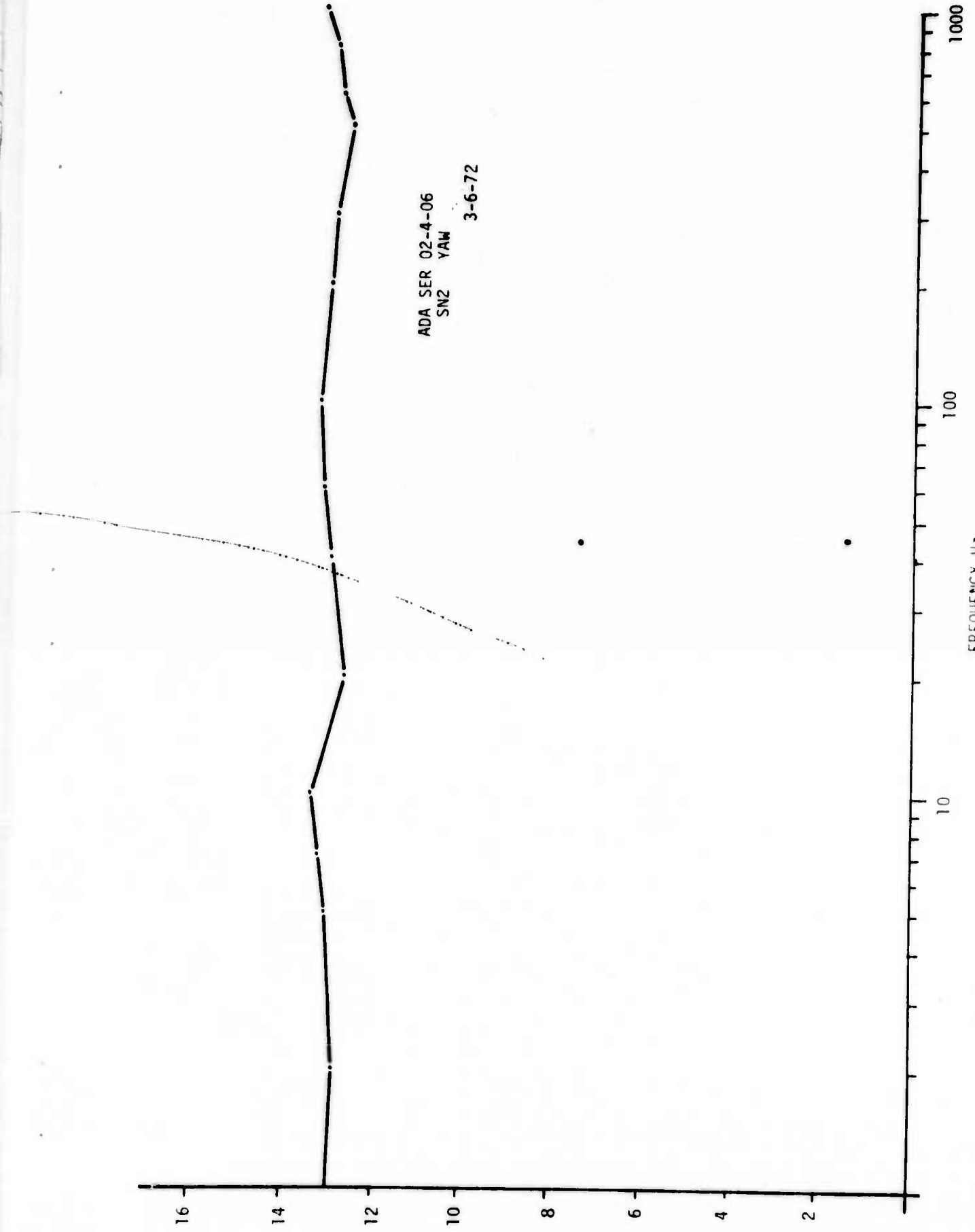

Figure 33. ADA Calibration in mV rms/rad/sec Peak-to-Peak

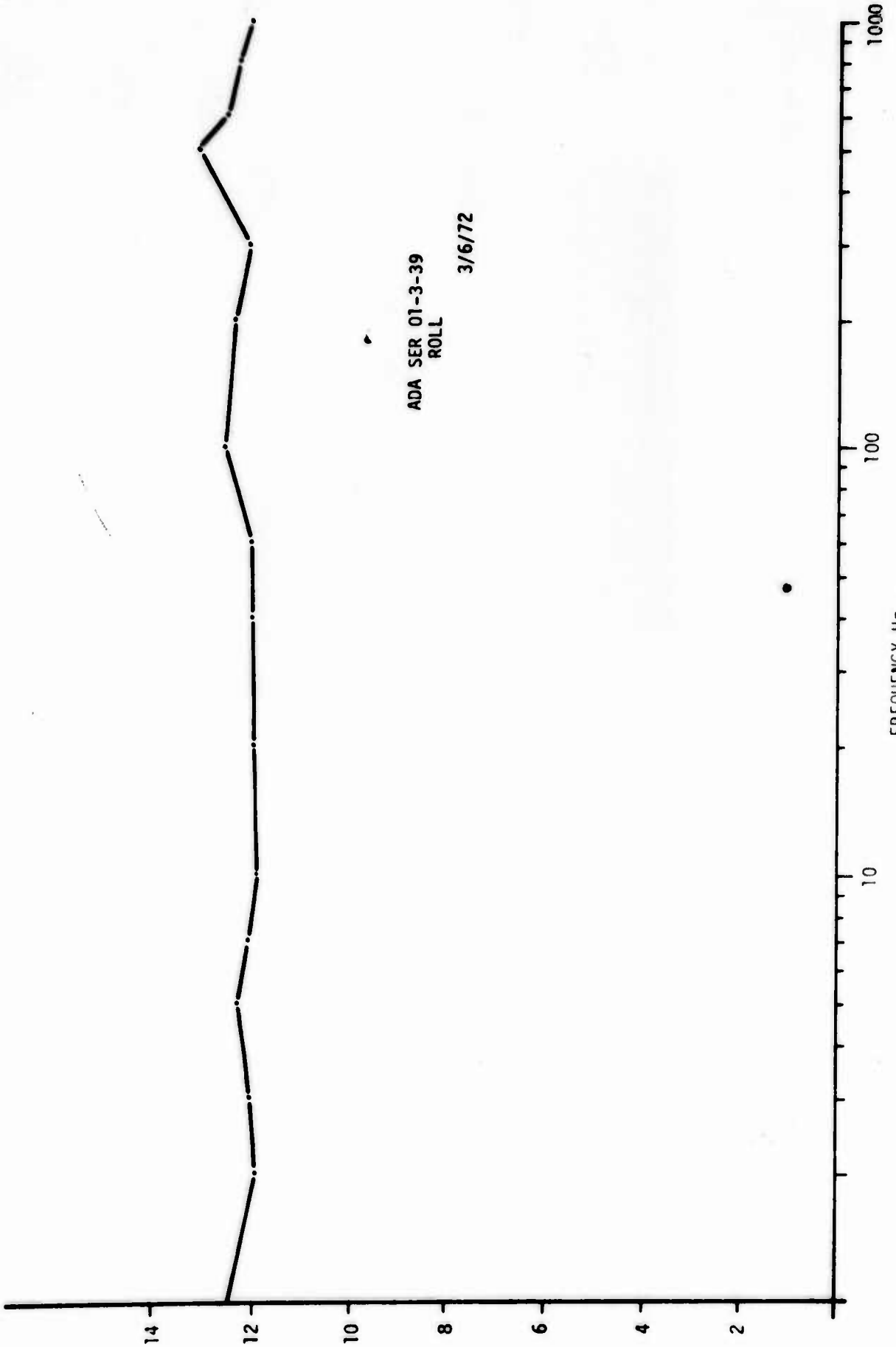

Figure 34. ADA Calibration in mV rms/rad/sec Peak-to-Peak

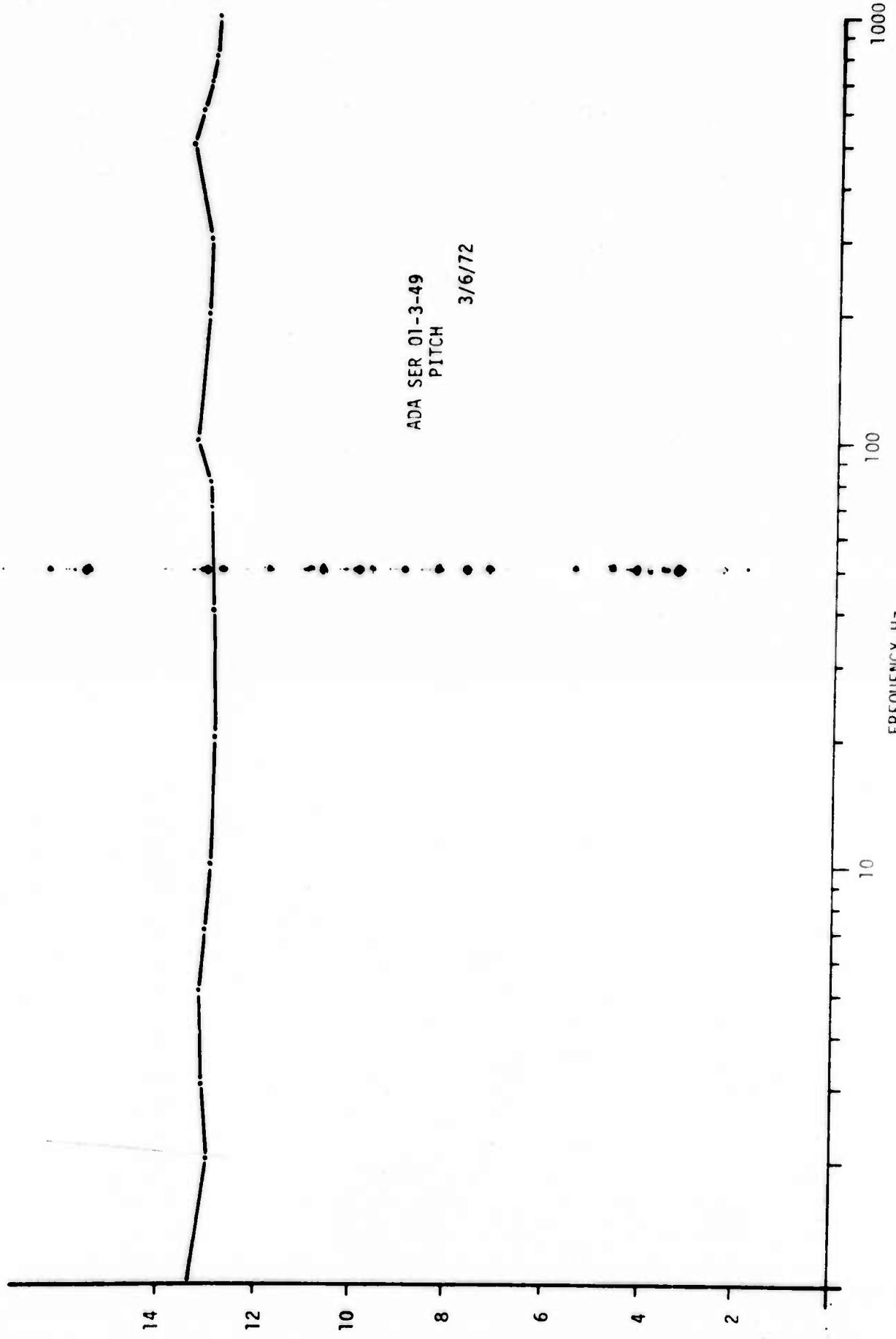

Figure 35. ADA Calibration in mV rms/rad/sec Peak-to-Peak

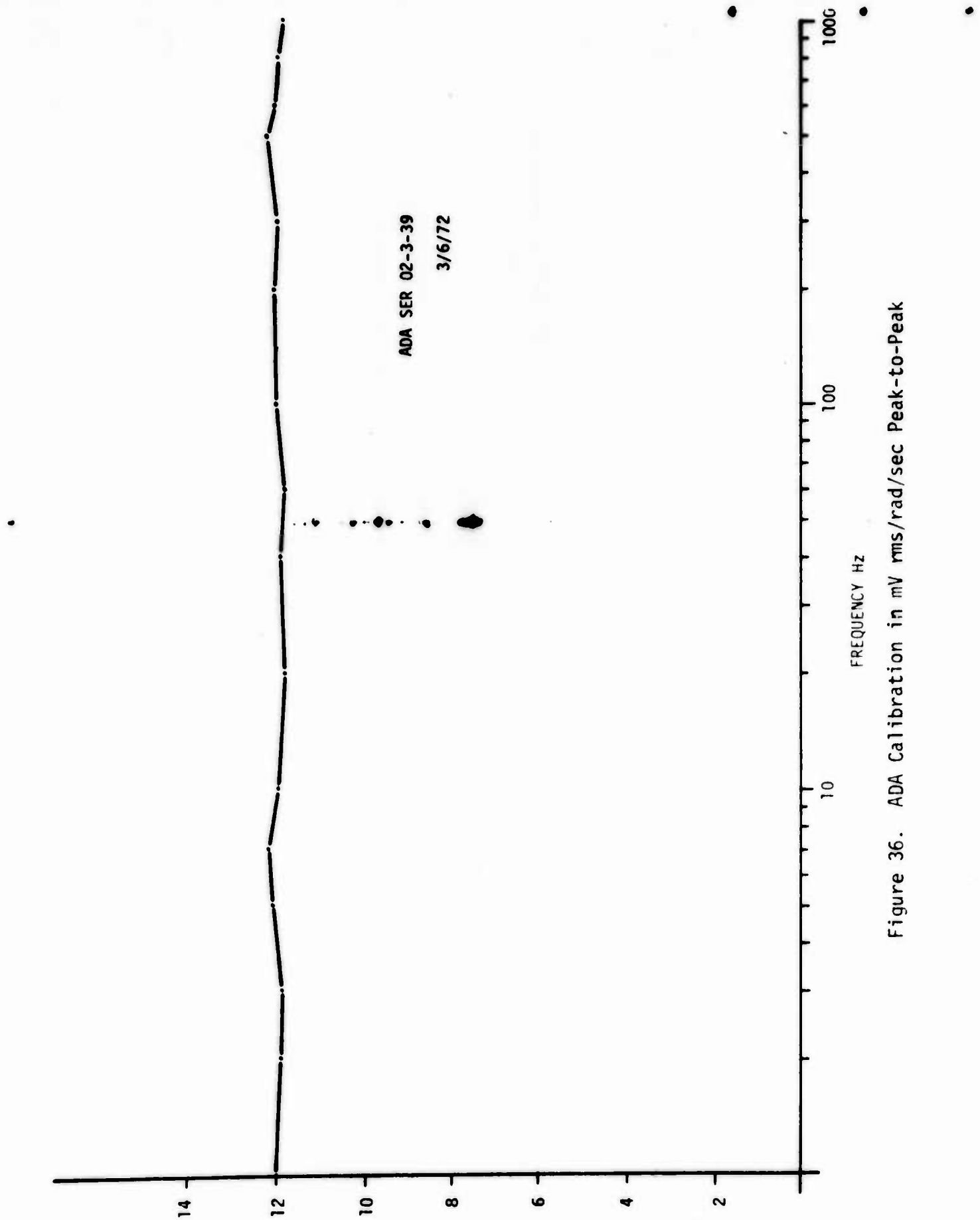

Figure 36. ADA Calibration in mV rms/rad/sec Peak-to-Peak

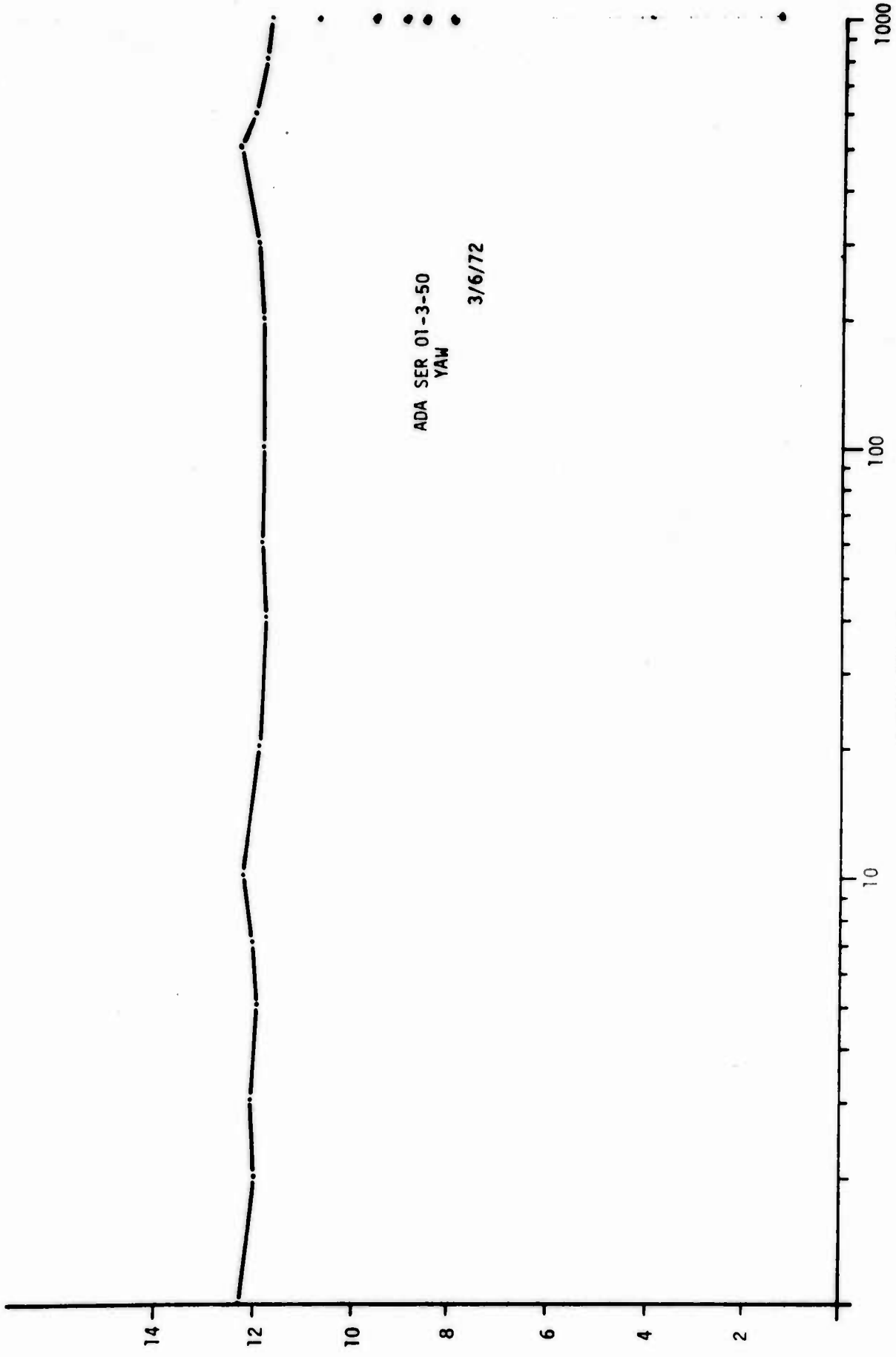

Figure 37. ADA Calibration in mV rms/rad/sec Peak-to-Peak

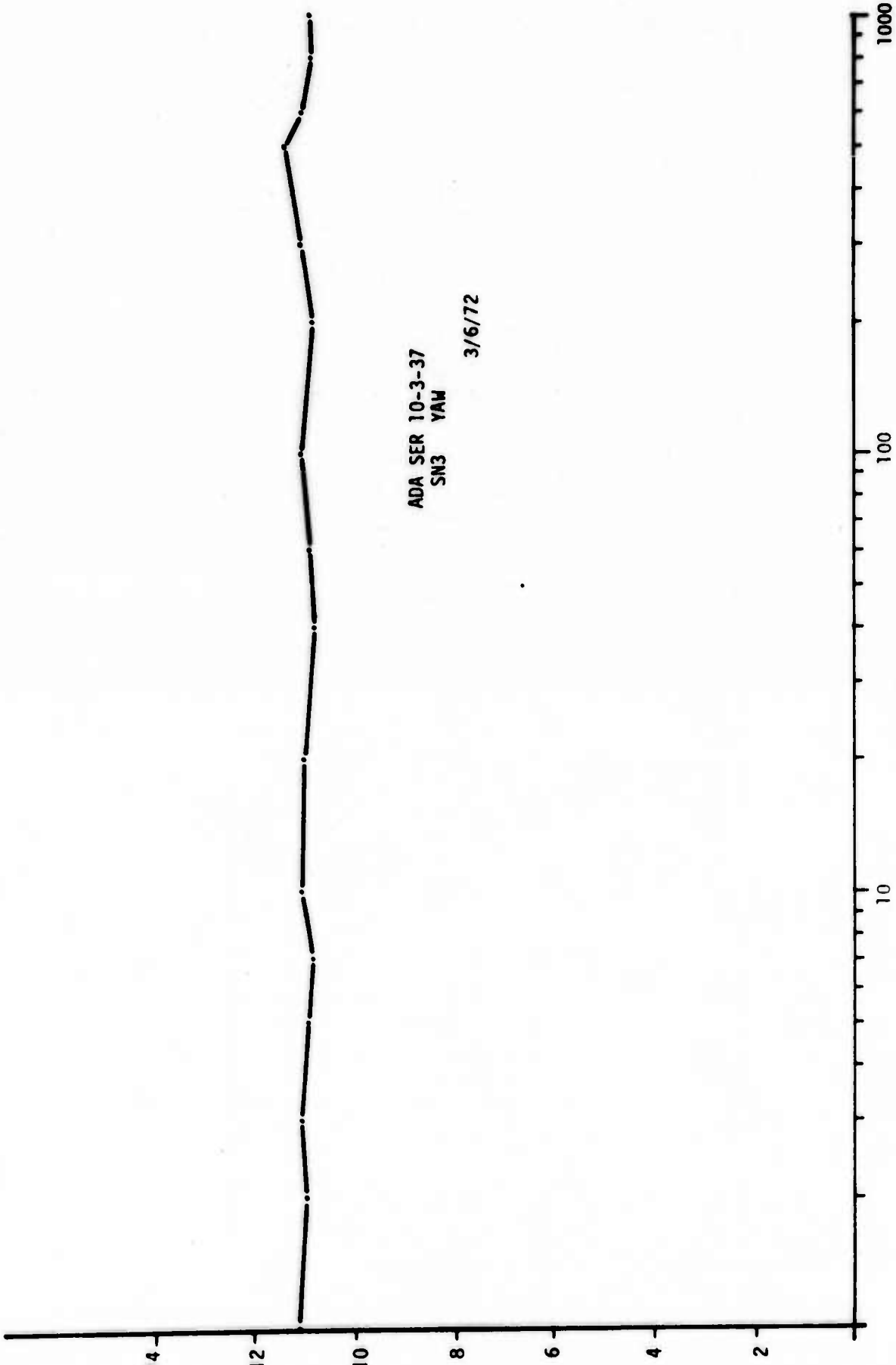

Figure 38. ADA Calibration in mV rms/rad/sec Peak-to-Peak

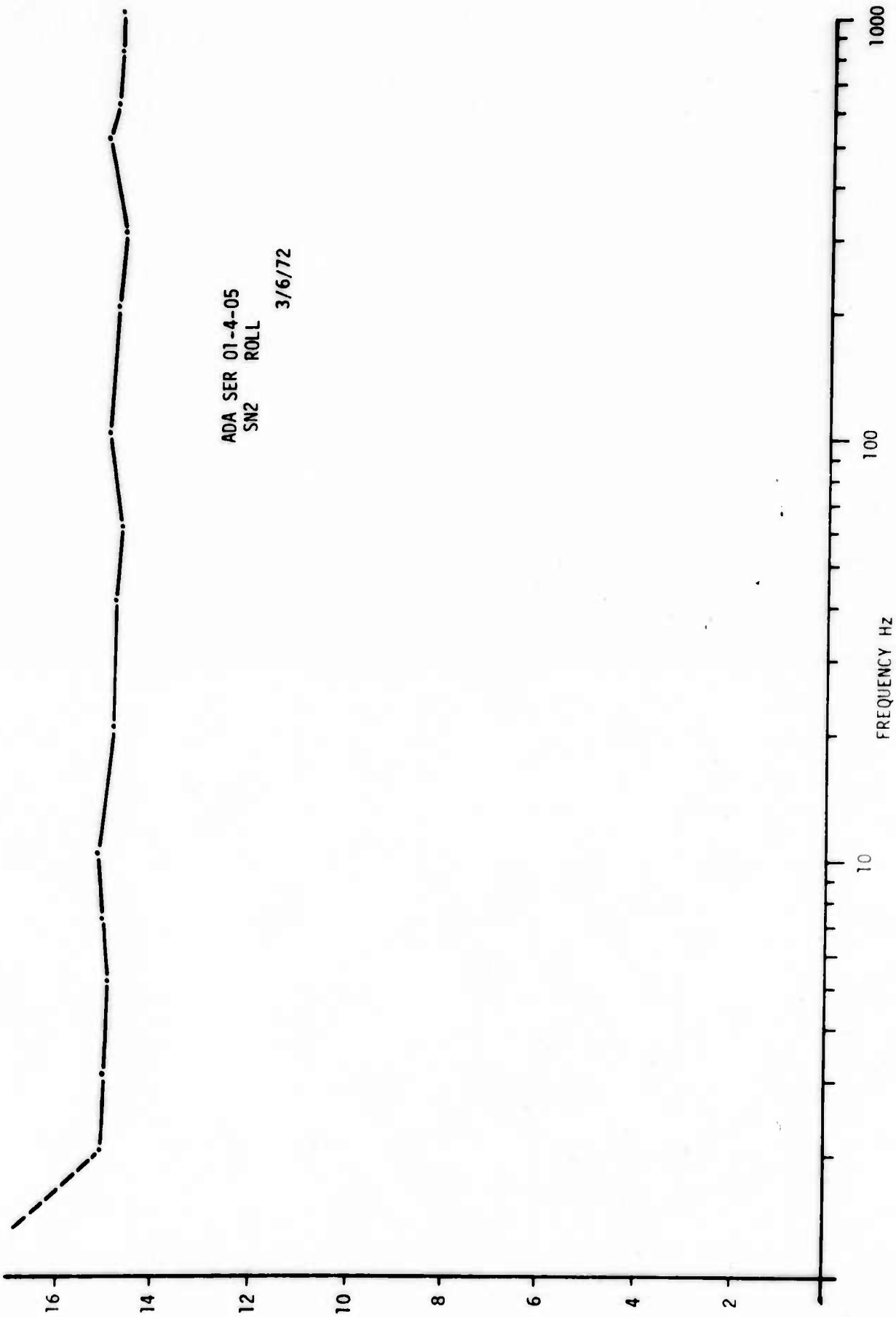

Figure 39. ADA Calibration in mV rms/rad/sec Peak-to-Peak

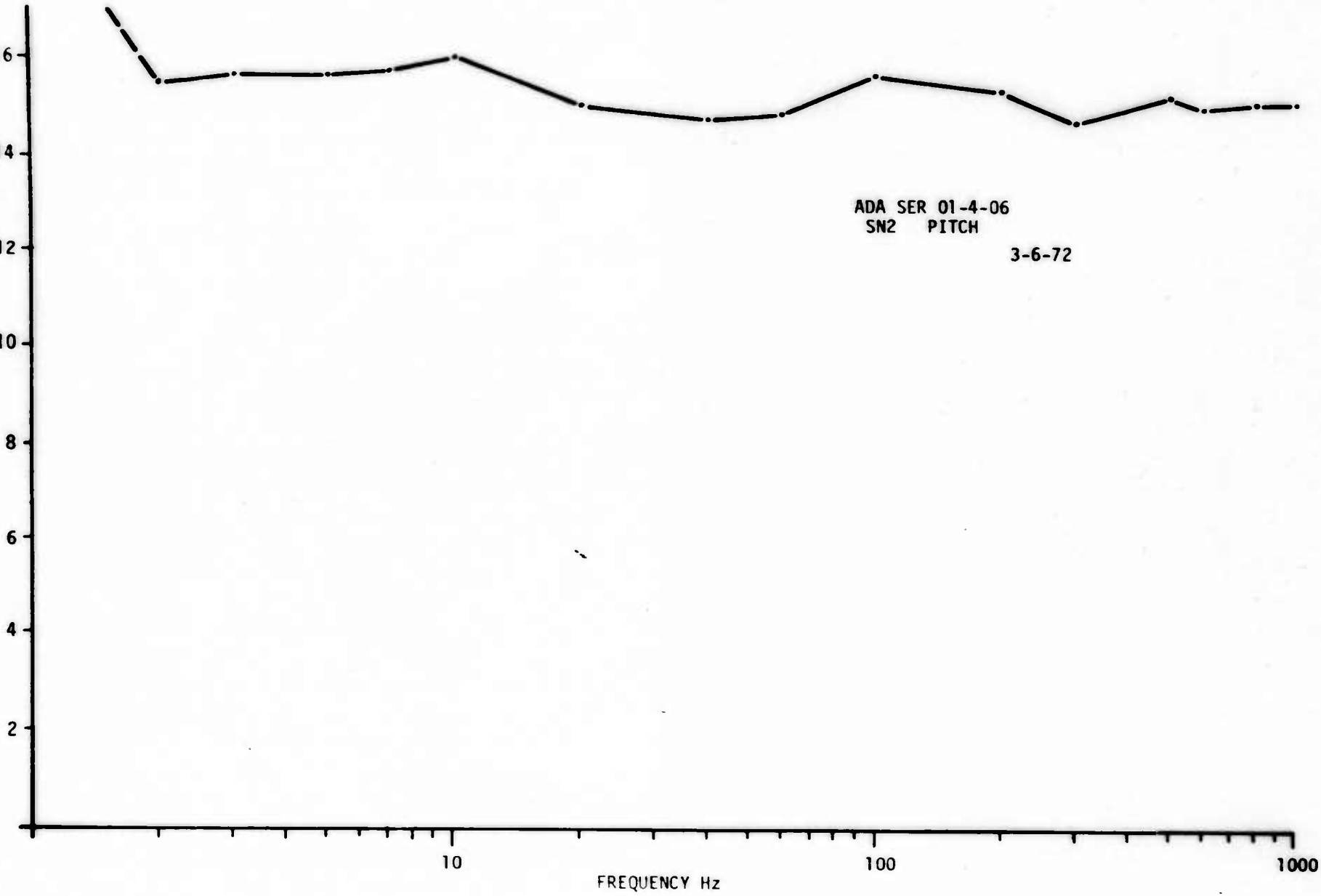

Figure 40. ADA Calibration in mV rms/rad/sec Peak-to-Peak

APPENDIX A

DERIVATION OF GENERAL TRANSFORMATION

The general transformation from one coordinate frame to another, using a sequence of rotations about three body axes, is derived. The axes chosen are shown in figure 41.

Rotation about x:

$$\bar{v} = \begin{bmatrix} 1 & 0 & 0 \\ 0 & \cos\alpha & -\sin\alpha \\ 0 & \sin\alpha & \cos\alpha \end{bmatrix} \bar{v}' \qquad \bar{v}' = \begin{bmatrix} 1 & 0 & 0 \\ 0 & \cos\alpha & \sin\alpha \\ 0 & -\sin\alpha & \cos\alpha \end{bmatrix} \bar{v}$$

Rotation about y':

$$\bar{v}' = \begin{bmatrix} \cos\beta & 0 & \sin\beta \\ 0 & 1 & 0 \\ -\sin\beta & 0 & \cos\beta \end{bmatrix} \bar{v}'' \qquad \bar{v}'' = \begin{bmatrix} \cos\beta & 0 & -\sin\beta \\ 0 & 1 & 0 \\ \sin\beta & 0 & \cos\beta \end{bmatrix} \bar{v}'$$

Rotation about z":

$$\bar{v}'' = \begin{bmatrix} \cos\gamma & -\sin\gamma & 0 \\ \sin\gamma & \cos\gamma & 0 \\ 0 & 0 & 1 \end{bmatrix} \bar{v}''' \qquad \bar{v}''' = \begin{bmatrix} \cos\gamma & \sin\gamma & 0 \\ -\sin\gamma & \cos\gamma & 0 \\ 0 & 0 & 1 \end{bmatrix} \bar{v}''$$

$$\bar{v}''' = T_{111-0}\,\bar{v}$$

$$T_{111-0} = \begin{bmatrix} \cos\gamma\cos\beta & \begin{pmatrix}\cos\gamma\sin\beta\sin\alpha \\ +\sin\gamma\cos\alpha\end{pmatrix} & \begin{pmatrix}-\cos\gamma\cos\alpha\sin\beta \\ +\sin\gamma\sin\alpha\end{pmatrix} \\ -\sin\gamma\cos\beta & \begin{pmatrix}-\sin\gamma\sin\beta\sin\alpha \\ +\cos\gamma\cos\alpha\end{pmatrix} & \begin{pmatrix}\sin\gamma\sin\beta\cos\alpha \\ +\cos\gamma\sin\alpha\end{pmatrix} \\ \sin\beta & -\cos\beta\sin\alpha & \cos\beta\cos\alpha \end{bmatrix}$$

$$\bar{v} = T_{0-111}\,\bar{v}'''$$

$$T_{0-111} = \begin{bmatrix} \cos\beta\cos\gamma & -\cos\beta\sin\gamma & \sin\beta \\ \begin{pmatrix}\cos\alpha\sin\gamma \\ +\sin\alpha\sin\beta\cos\gamma\end{pmatrix} & \begin{pmatrix}\cos\alpha\cos\gamma \\ -\sin\alpha\sin\beta\sin\gamma\end{pmatrix} & -\sin\alpha\cos\beta \\ \begin{pmatrix}\sin\alpha\sin\gamma \\ -\cos\alpha\cos\gamma\sin\beta\end{pmatrix} & \begin{pmatrix}\sin\alpha\cos\gamma \\ +\cos\alpha\sin\beta\sin\gamma\end{pmatrix} & \cos\alpha\cos\beta \end{bmatrix}$$

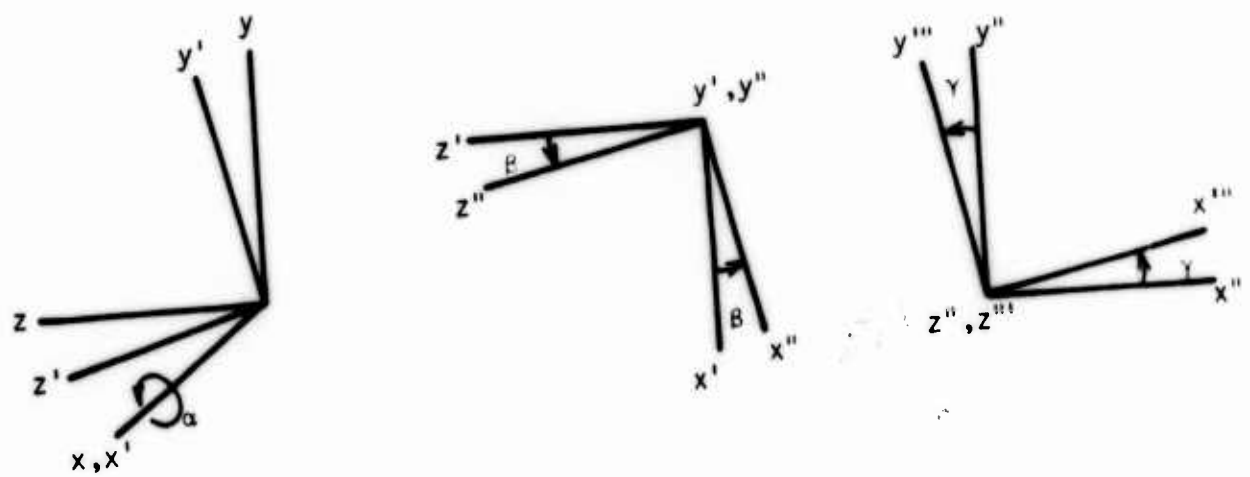

Figure 41. Three Step Rotation Sequence

APPENDIX B

DATA SETS 1, 3, AND 4

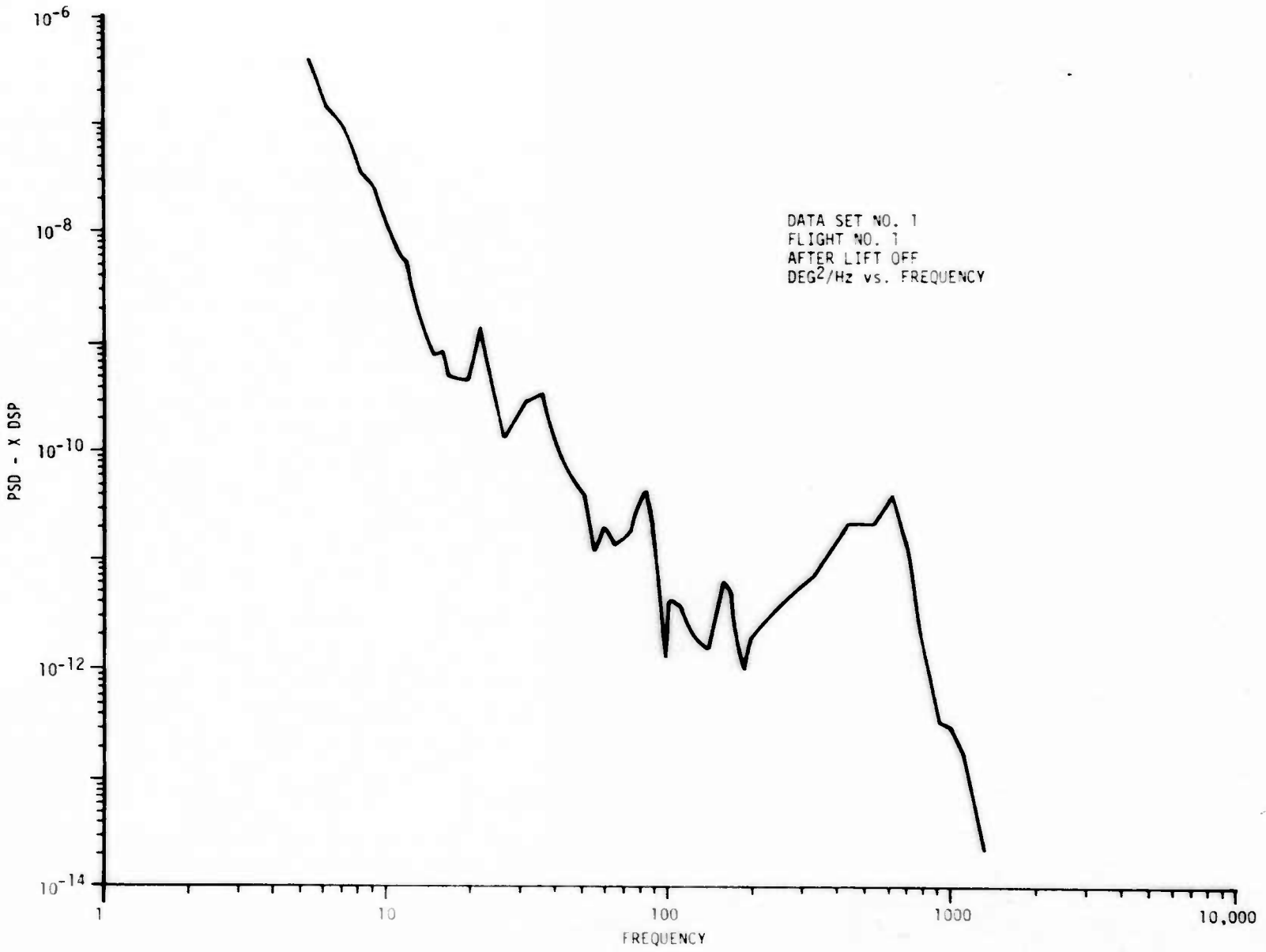

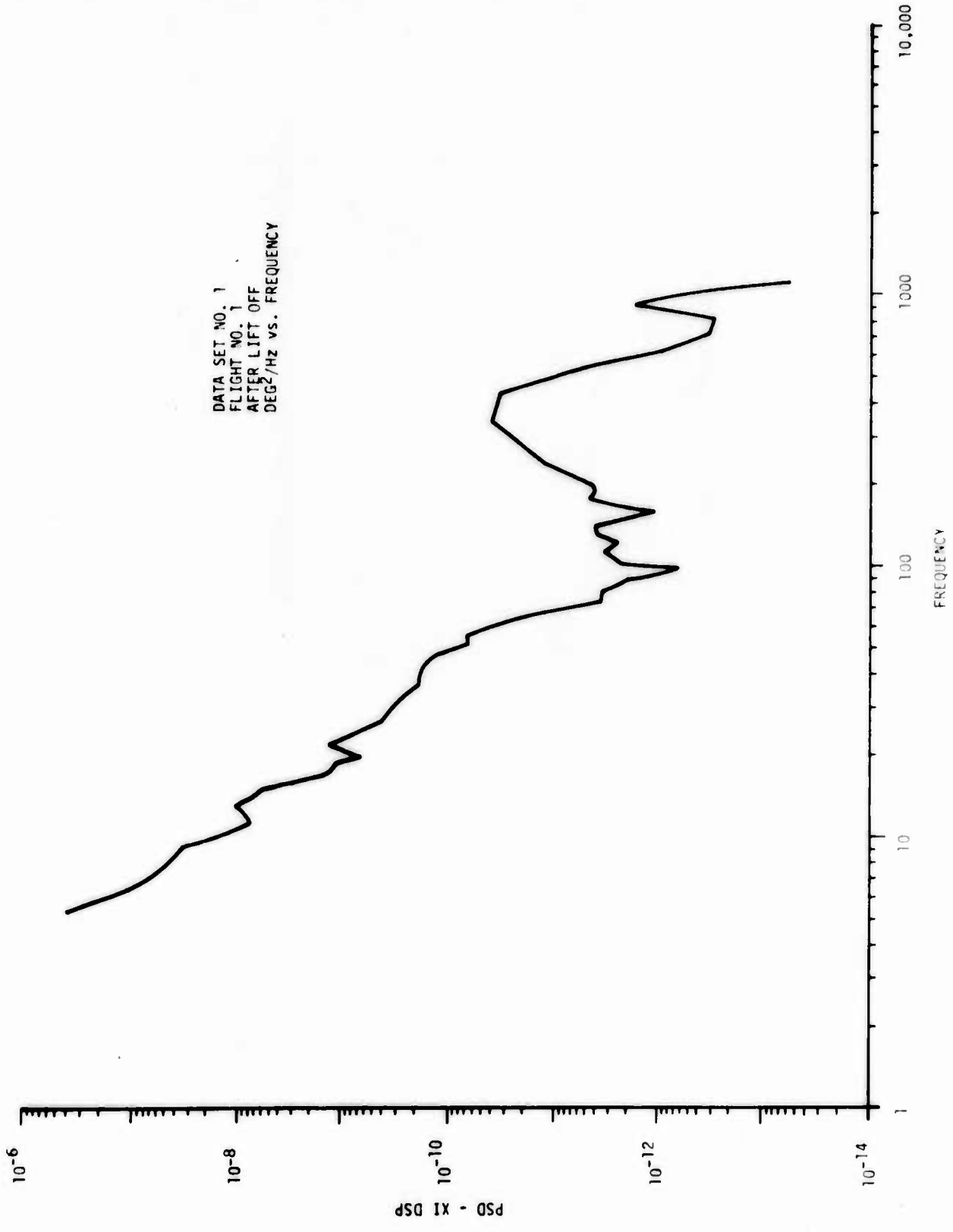
DATA SET NO. 1
FLIGHT NO. 1
AFTER LIFT OFF
DEG²/Hz vs. FREQUENCY
PSD - XI DSP
10⁻⁶
10⁻⁸
10⁻¹⁰
10⁻¹²
10⁻¹⁴
1
10
100
1000
10,000
FREQUENCY

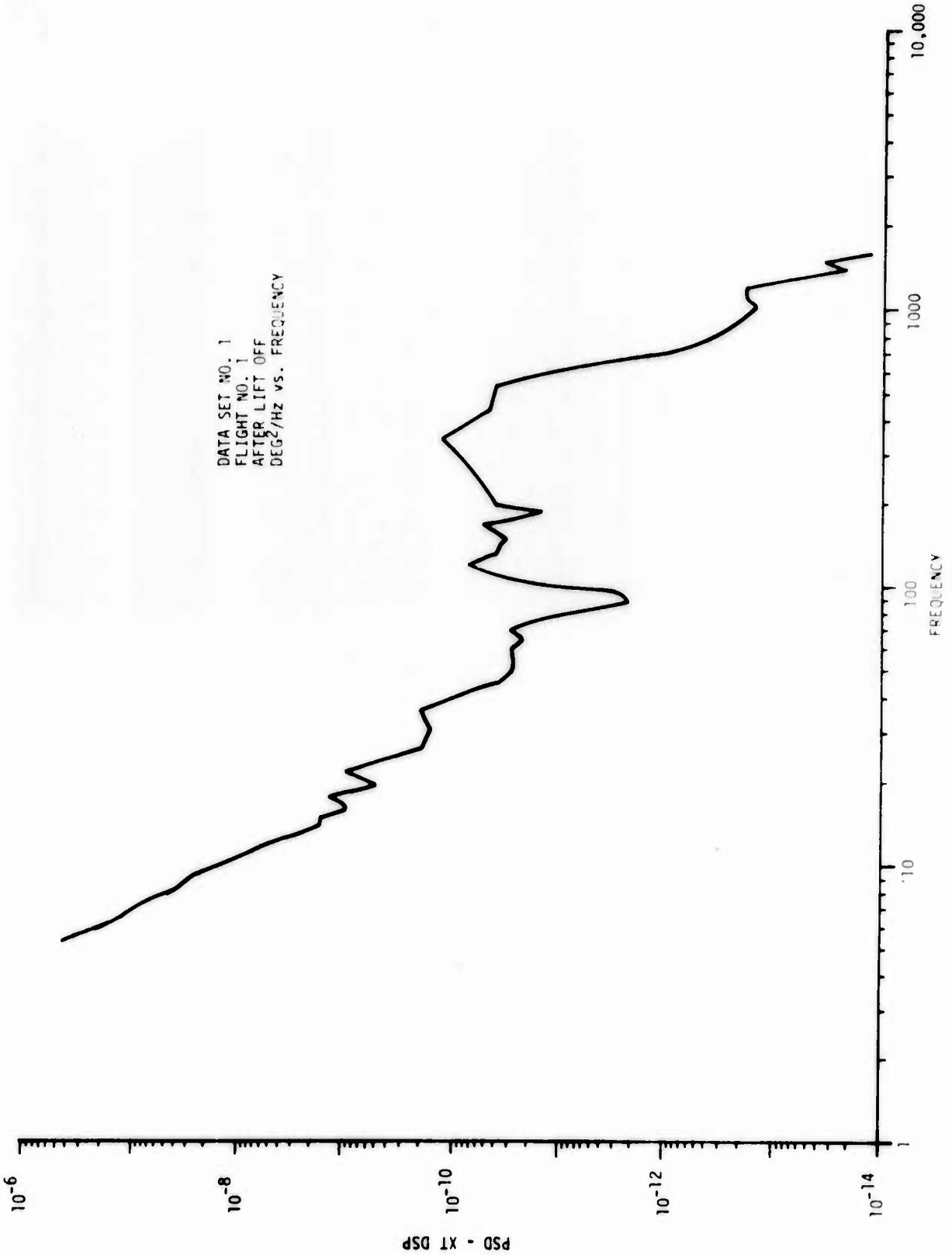
DATA SET NO. 1
FLIGHT NO. 1
AFTER LIFT OFF
DEG²/Hz vs. FREQUENCY
PSD - XT DSP
10⁻⁶
10⁻⁸
10⁻¹⁰
10⁻¹²
10⁻¹⁴
1
10
100
1000
10,000
FREQUENCY

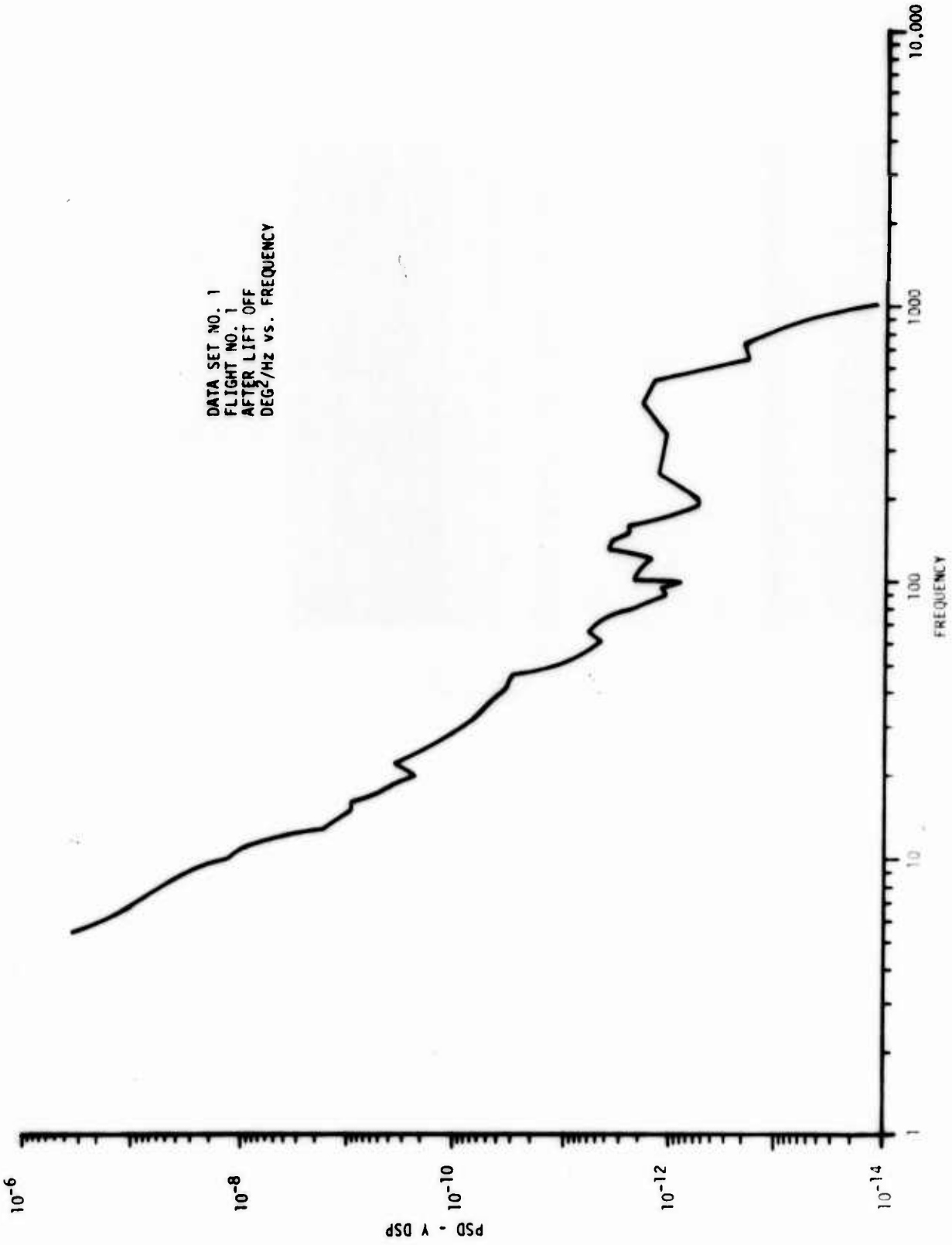
DATA SET NO. 1
FLIGHT NO. 1
AFTER LIFT OFF
DEG²/Hz vs. FREQUENCY
PSD - Y DSP
10⁻⁶
10⁻⁸
10⁻¹⁰
10⁻¹²
10⁻¹⁴
1
10
100
1000
10,000
FREQUENCY

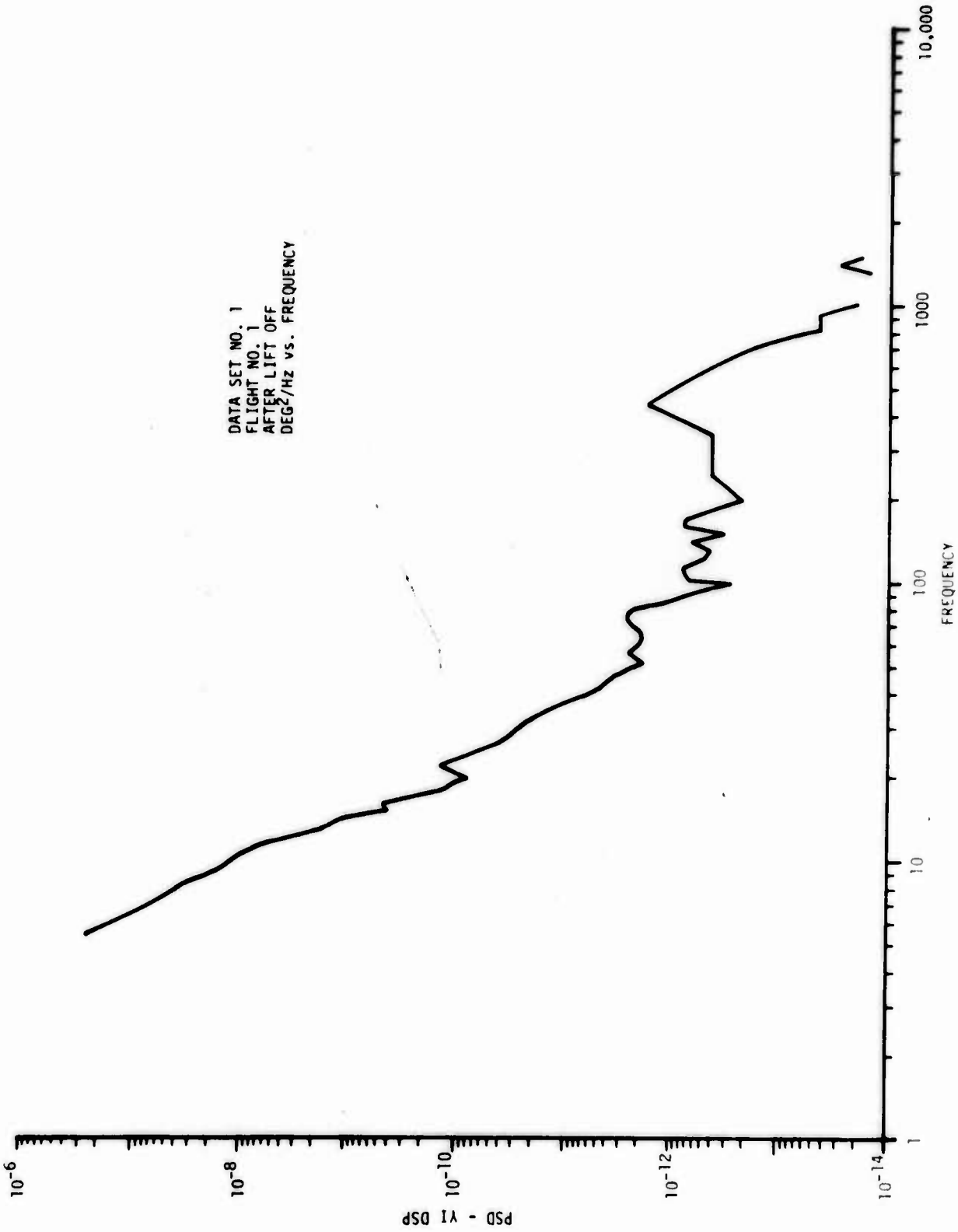
DATA SET NO. 1
FLIGHT NO. 1
AFTER LIFT OFF
DEG²/Hz vs. FREQUENCY
PSD - Y1 DSP
10⁻⁶
10⁻⁸
10⁻¹⁰
10⁻¹²
10⁻¹⁴
1
10
100
1000
10,000
FREQUENCY

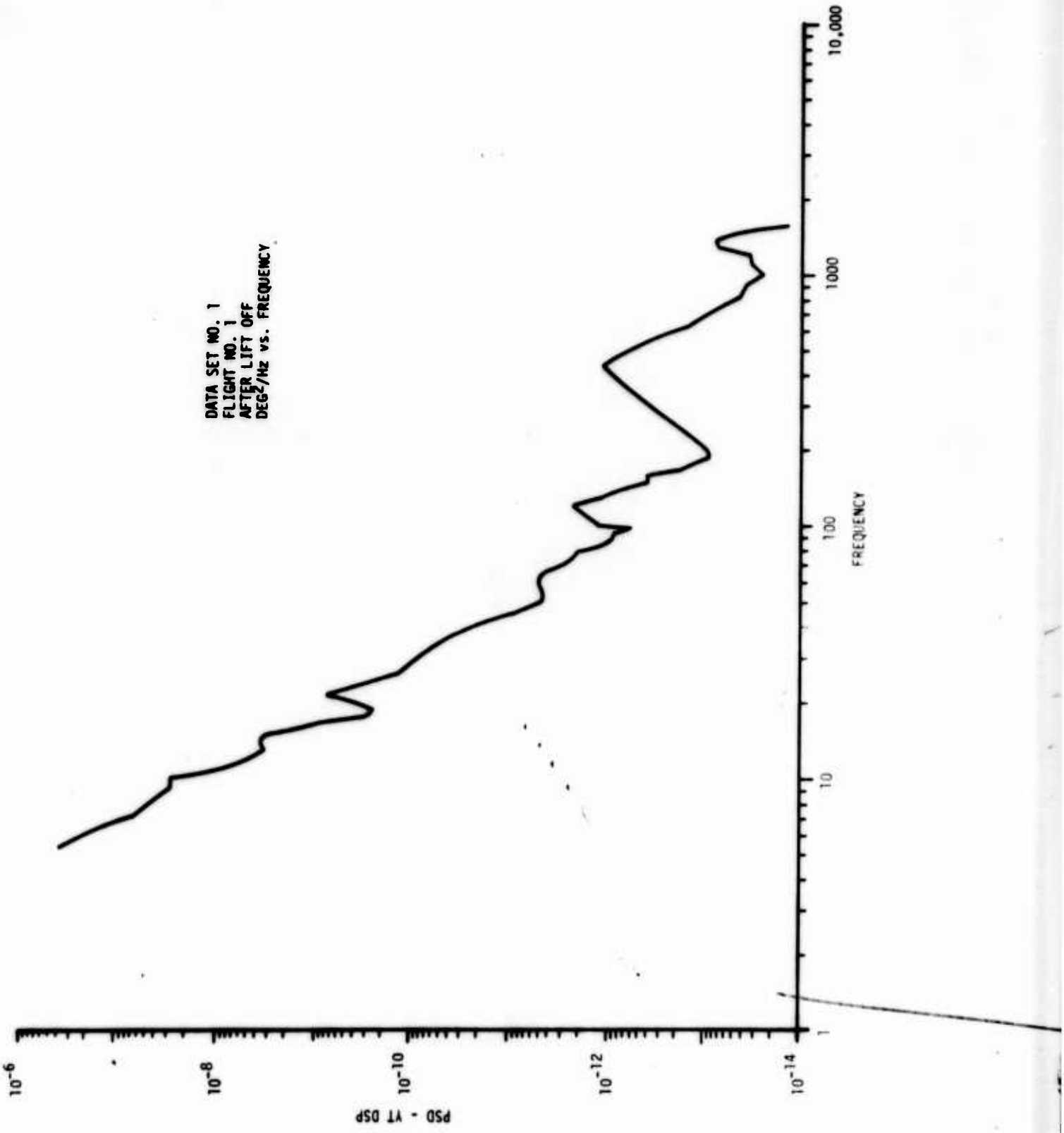
DATA SET NO. 1
FLIGHT NO. 1
AFTER LIFT OFF
DEG²/Hz vs. FREQUENCY
PSD - YT DSP
10⁻⁶
10⁻⁸
10⁻¹⁰
10⁻¹²
10⁻¹⁴
1
10
100
1000
10,000
FREQUENCY

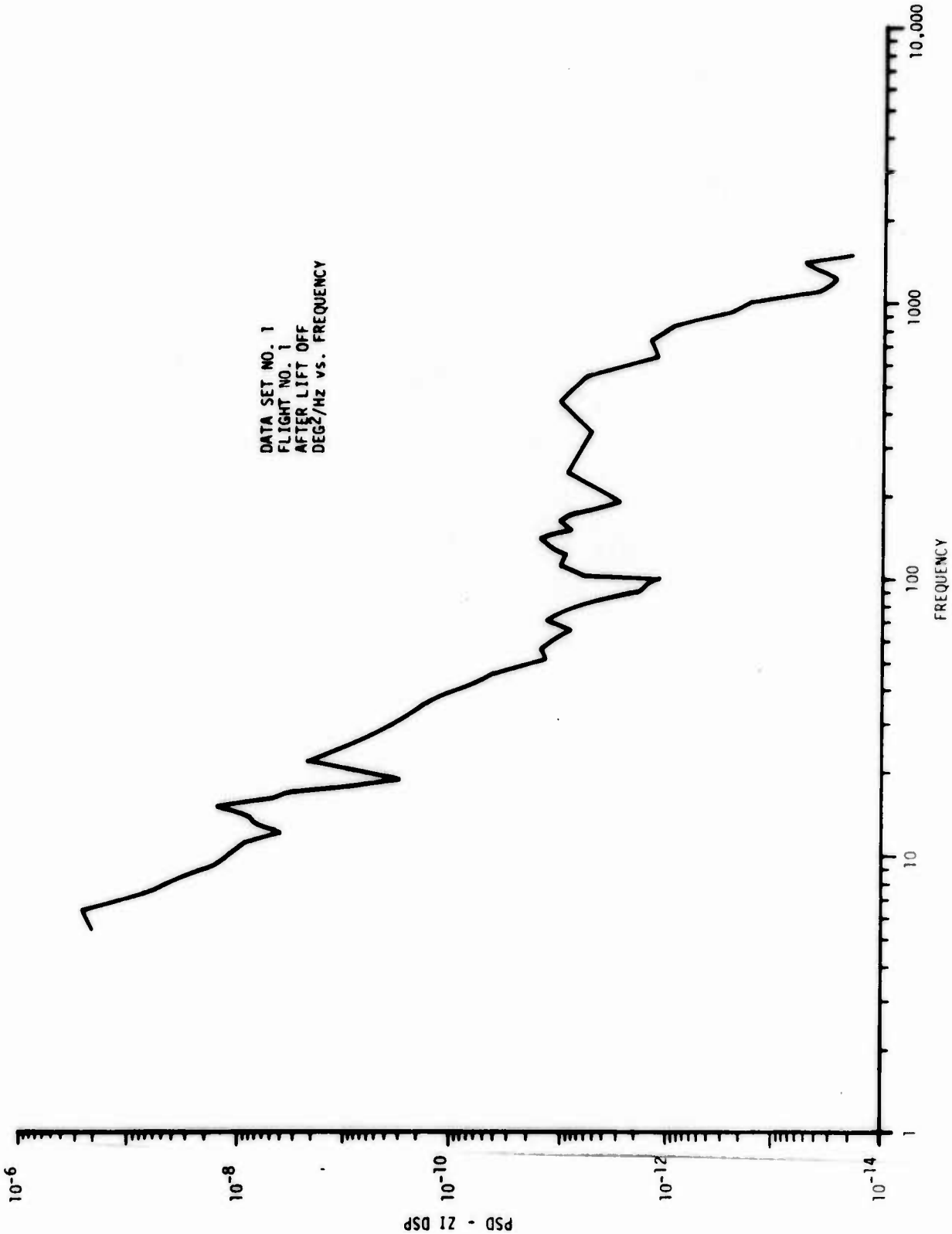
DATA SET NO. 1
FLIGHT NO. 1
AFTER LIFT OFF
DEG²/Hz vs. FREQUENCY
PSD - Z1 DSP
10⁻⁶
10⁻⁸
10⁻¹⁰
10⁻¹²
10⁻¹⁴
1
10
100
1000
10,000
FREQUENCY

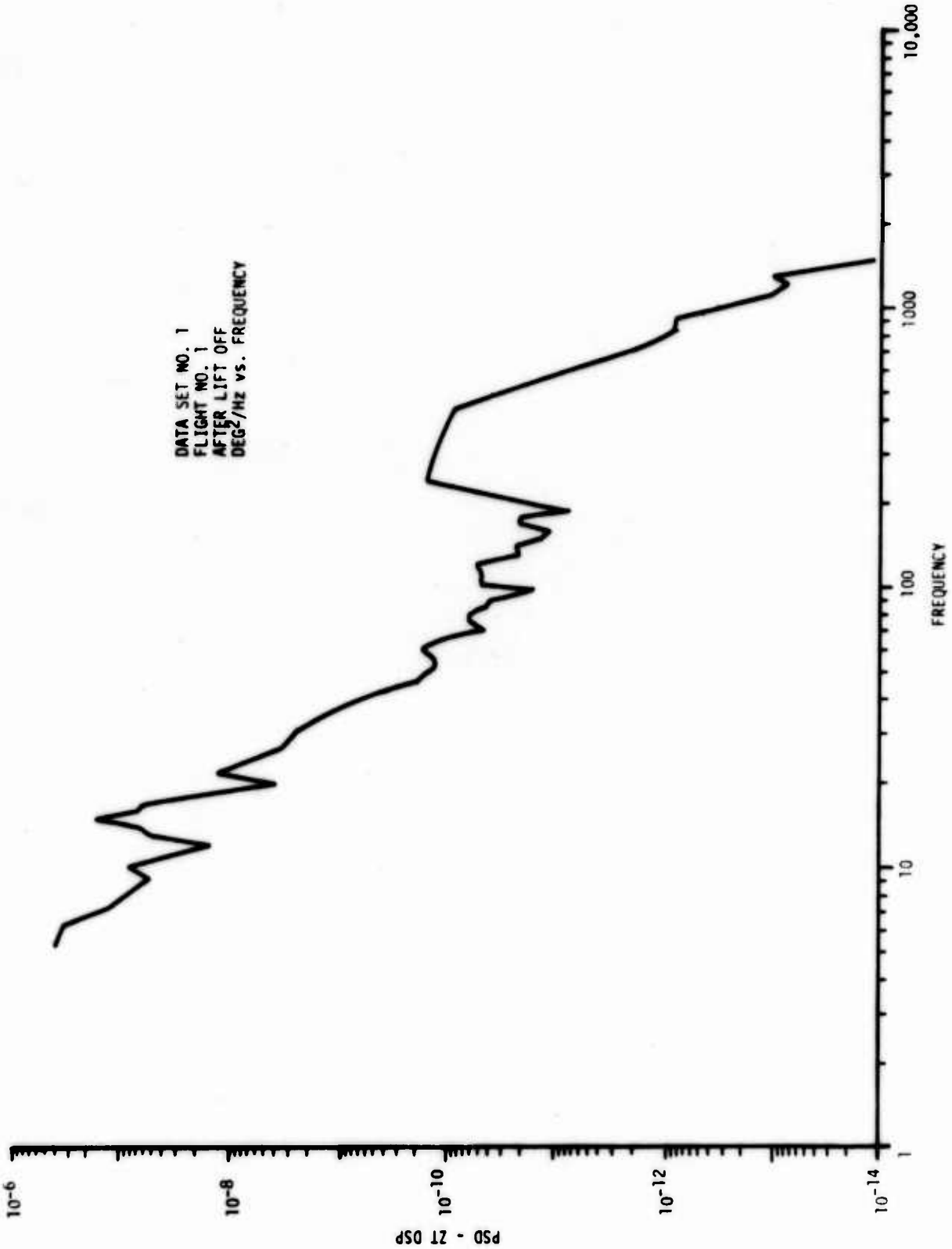
DATA SET NO. 1
FLIGHT NO. 1
AFTER LIFT OFF
DEG²/Hz vs. FREQUENCY
PSD - ZT DSP
10⁻⁶
10⁻⁸
10⁻¹⁰
10⁻¹²
10⁻¹⁴
1
10
100
1000
10,000
FREQUENCY

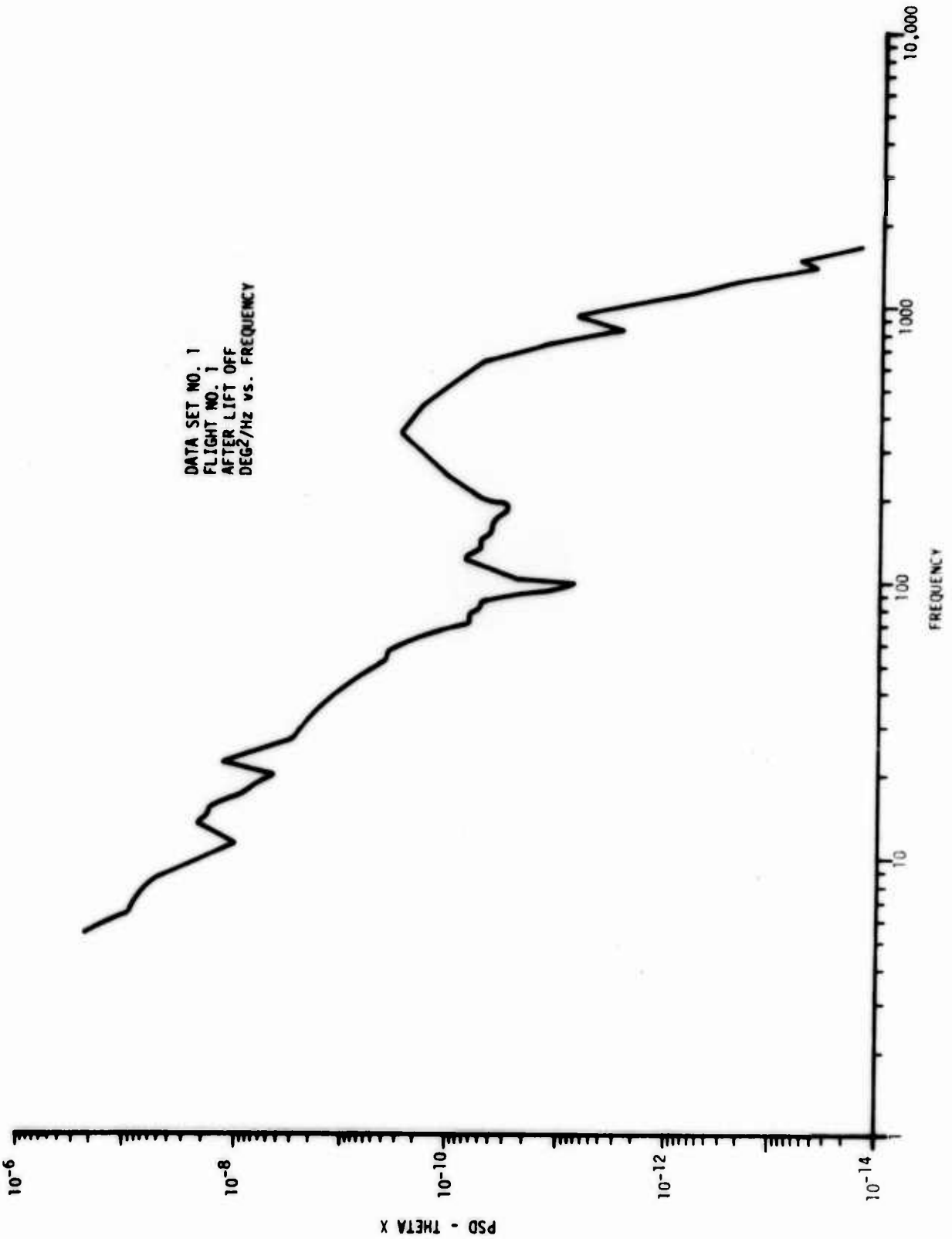
DATA SET NO. 1
FLIGHT NO. 1
AFTER LIFT OFF
DEG²/Hz vs. FREQUENCY
PSD - THETA X
10⁻⁶
10⁻⁸
10⁻¹⁰
10⁻¹²
10⁻¹⁴
10
100
1000
10,000
FREQUENCY

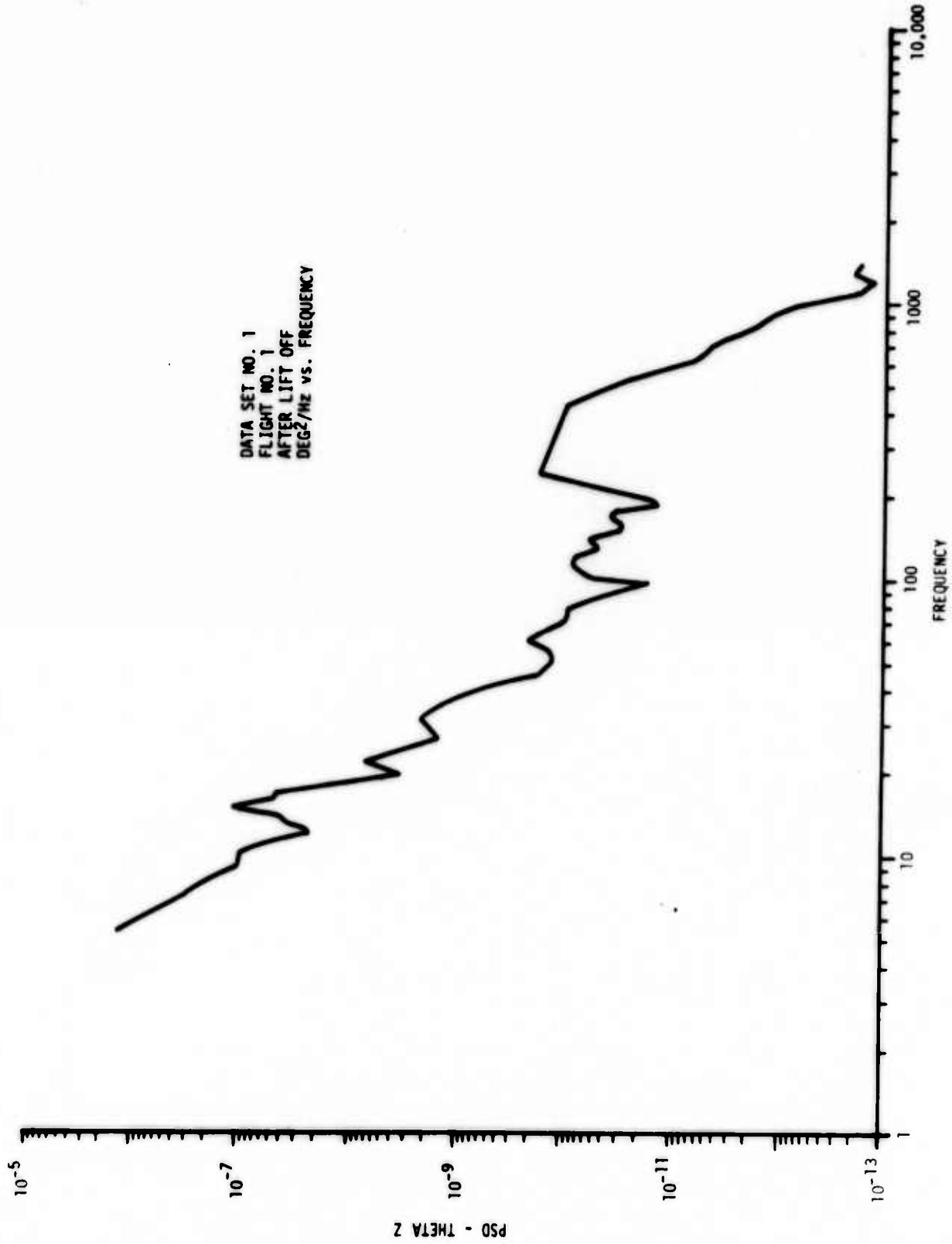
DATA SET NO. 1
FLIGHT NO. 1
AFTER LIFT OFF
DEG²/Hz vs. FREQUENCY
PSD - THETA Z
10⁻⁵
10⁻⁷
10⁻⁹
10⁻¹¹
10⁻¹³
1
10
100
1000
10,000
FREQUENCY

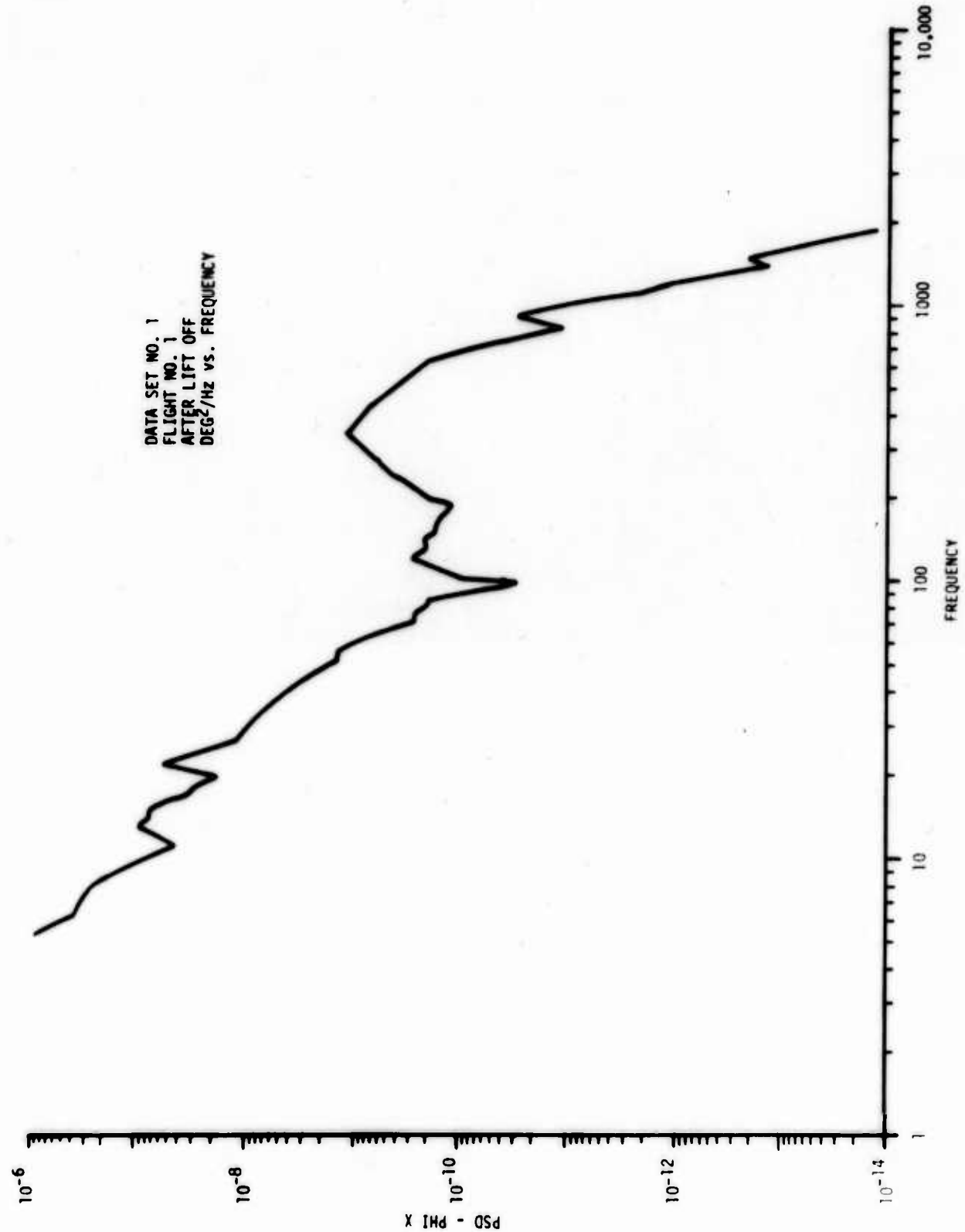
DATA SET NO. 1
FLIGHT NO. 1
AFTER LIFT OFF
DEG²/Hz vs. FREQUENCY
PSD - PHI X
10⁻⁶
10⁻⁸
10⁻¹⁰
10⁻¹²
10⁻¹⁴
1
10
100
1000
10,000
FREQUENCY

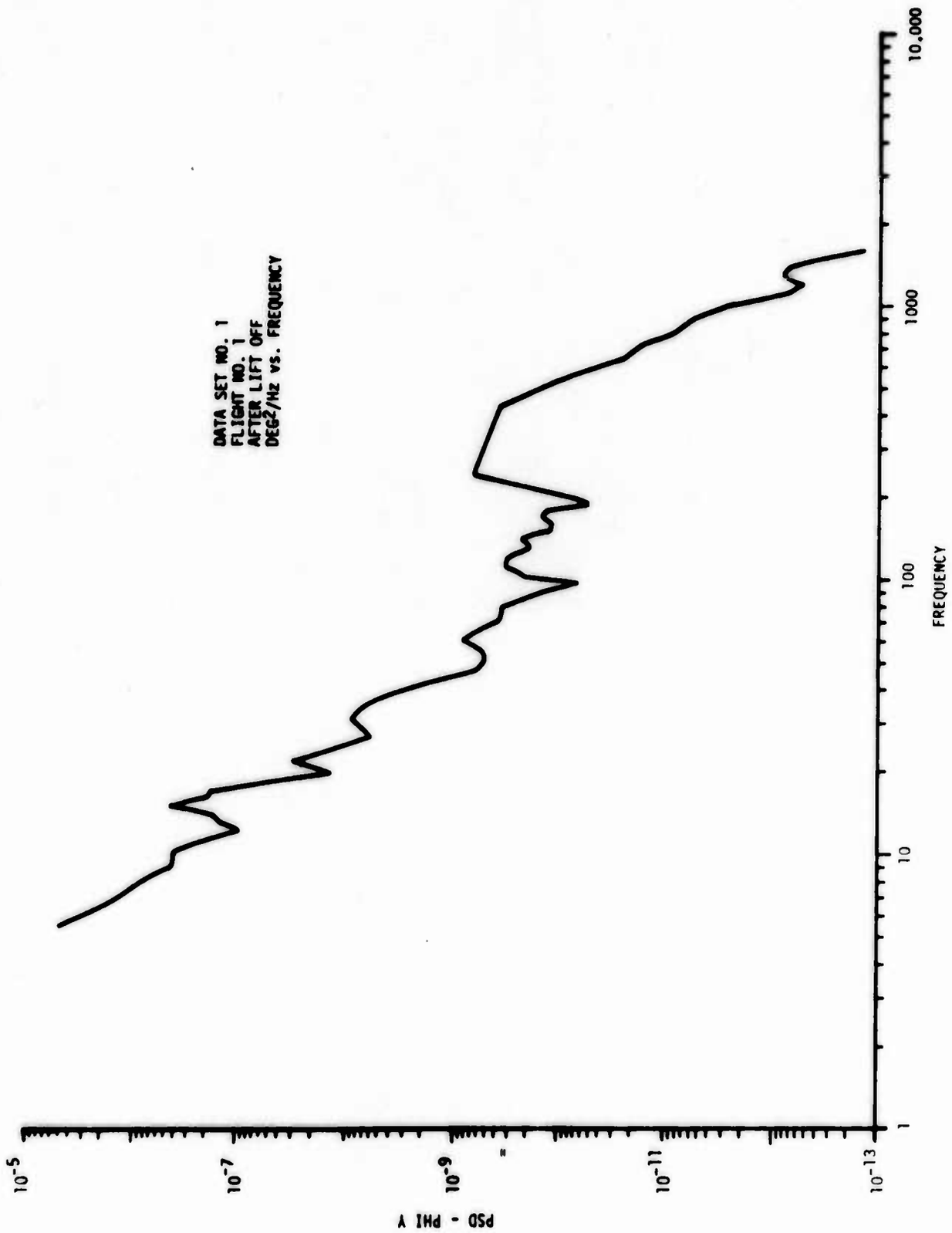
DATA SET NO. 1
FLIGHT NO. 1
AFTER LIFT OFF
DEG²/Hz vs. FREQUENCY
PSD - PHI Y
10⁻⁵
10⁻⁷
10⁻⁹
10⁻¹¹
10⁻¹³
1
10
100
1000
10,000
FREQUENCY

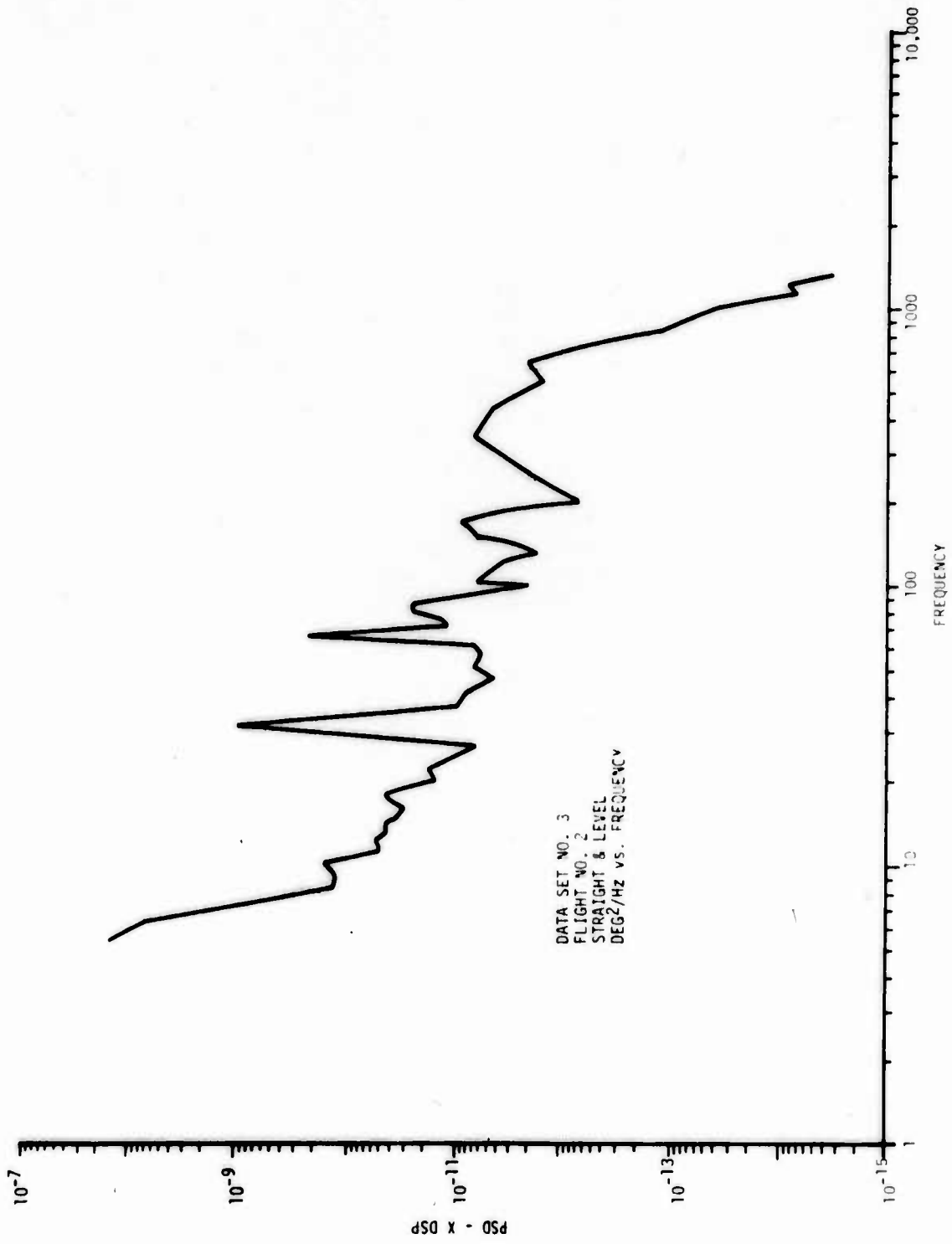
PSD - x DSP
10^{-7}
10^{-9}
10^{-11}
10^{-13}
10^{-15}
1
10
100
1000
10,000
FREQUENCY
DATA SET NO. 3
FLIGHT NO. 2
STRAIGHT & LEVEL
DEG²/Hz vs. FREQUENCY

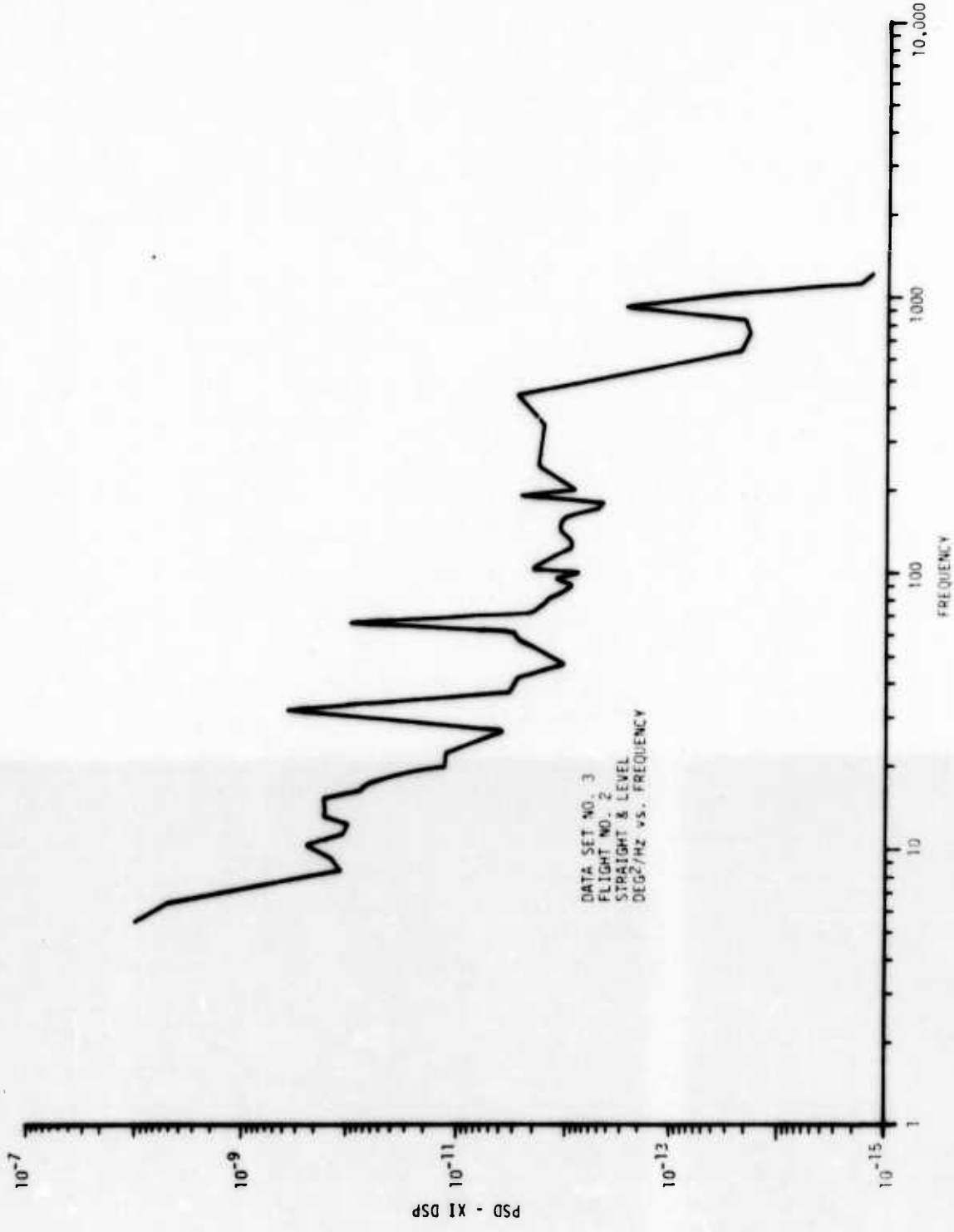
PSD - XI DSP
10^{-7}
10^{-9}
10^{-11}
10^{-13}
10^{-15}
1
10
100
1000
10,000
FREQUENCY
DATA SET NO. 3
FLIGHT NO. 2
STRAIGHT & LEVEL
DEG²/Hz vs. FREQUENCY

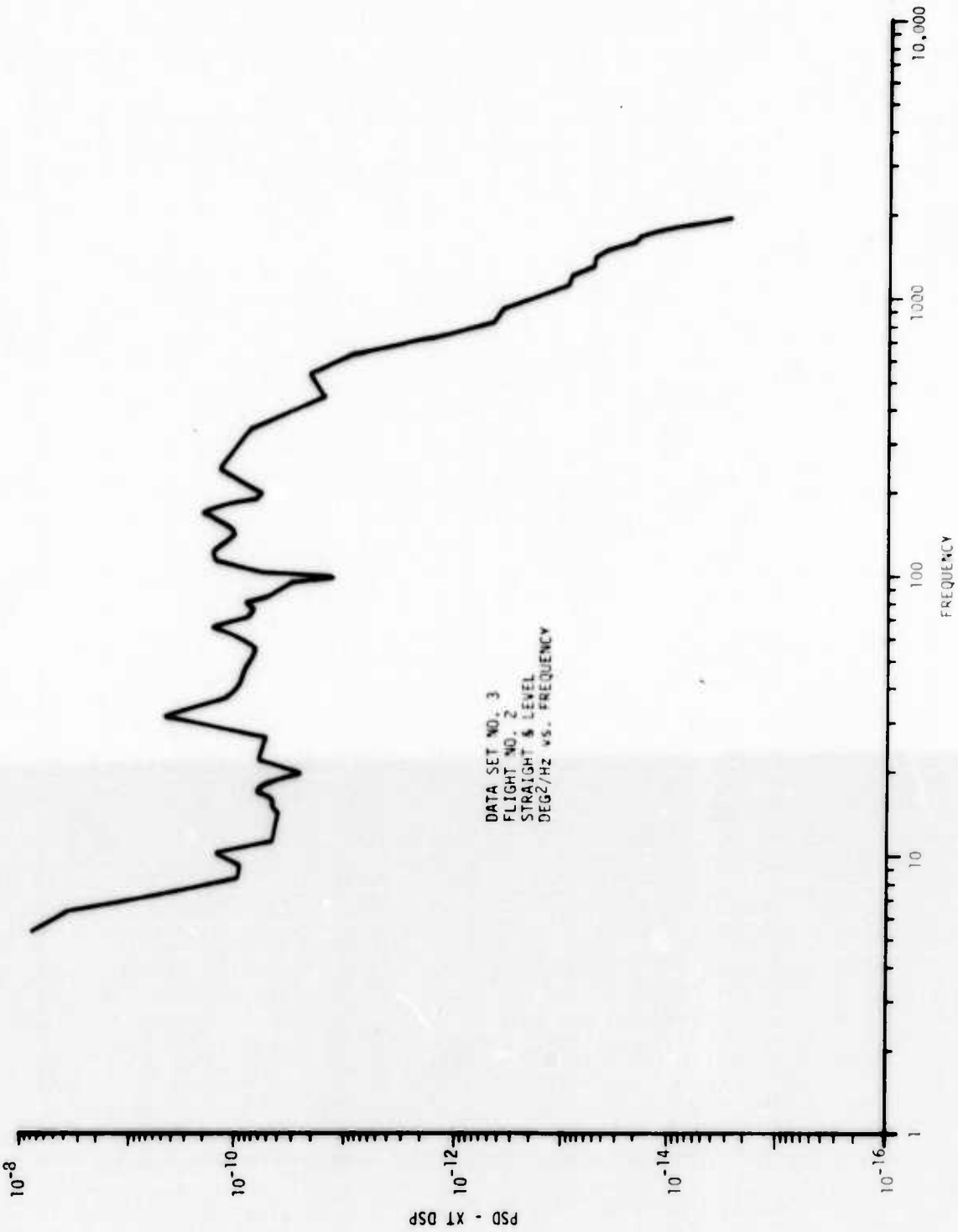
DATA SET NO. 3
FLIGHT NO. 2
STRAIGHT & LEVEL
DEG²/Hz vs. FREQUENCY
PSD - XT DSP
10^{-8}
10^{-10}
10^{-12}
10^{-14}
10^{-16}
1
10
100
1000
10,000
FREQUENCY

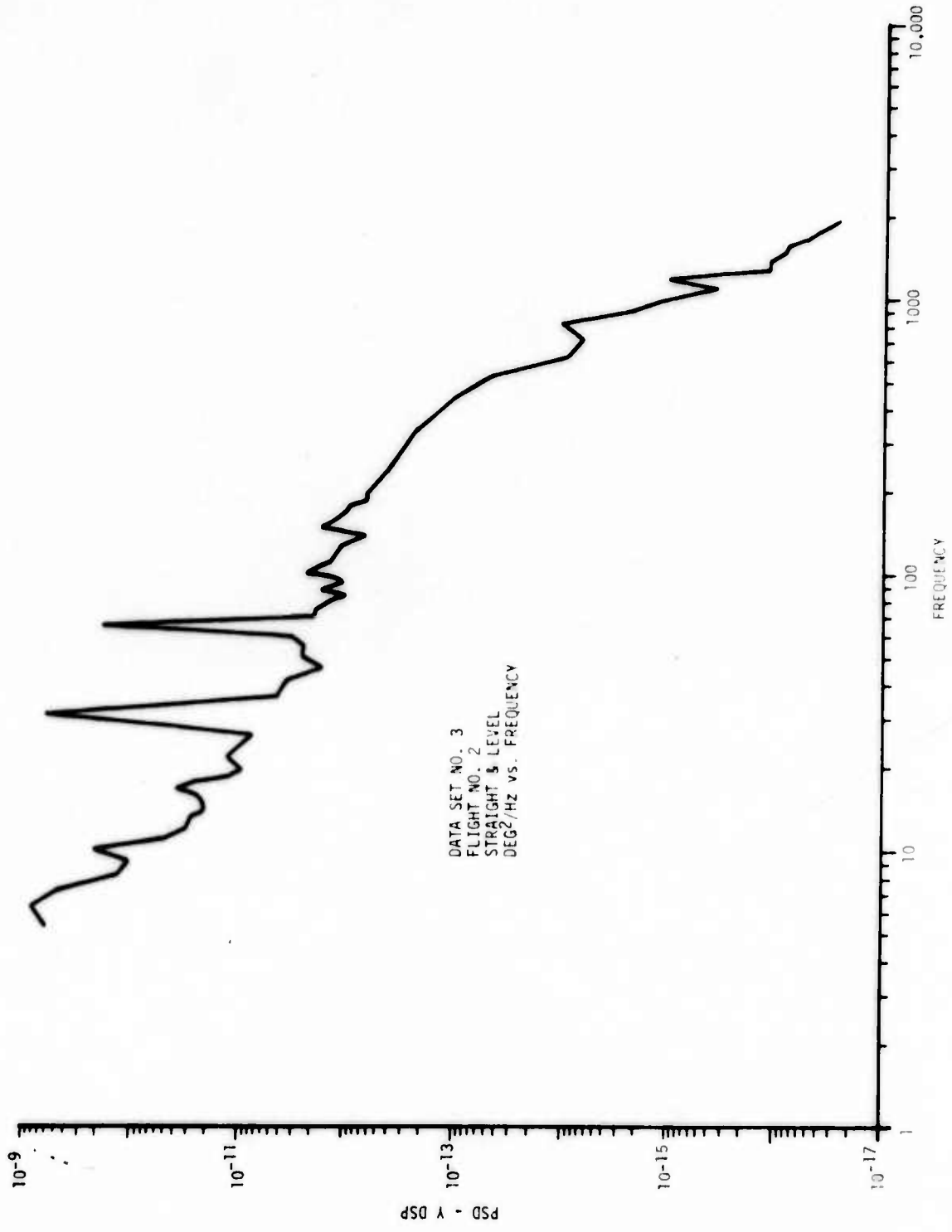
DATA SET NO. 3
FLIGHT NO. 2
STRAIGHT & LEVEL
DEG²/Hz vs. FREQUENCY
PSD - γ DSP
10⁻⁹
10⁻¹¹
10⁻¹³
10⁻¹⁵
10⁻¹⁷
1
10
100
1000
10,000
FREQUENCY

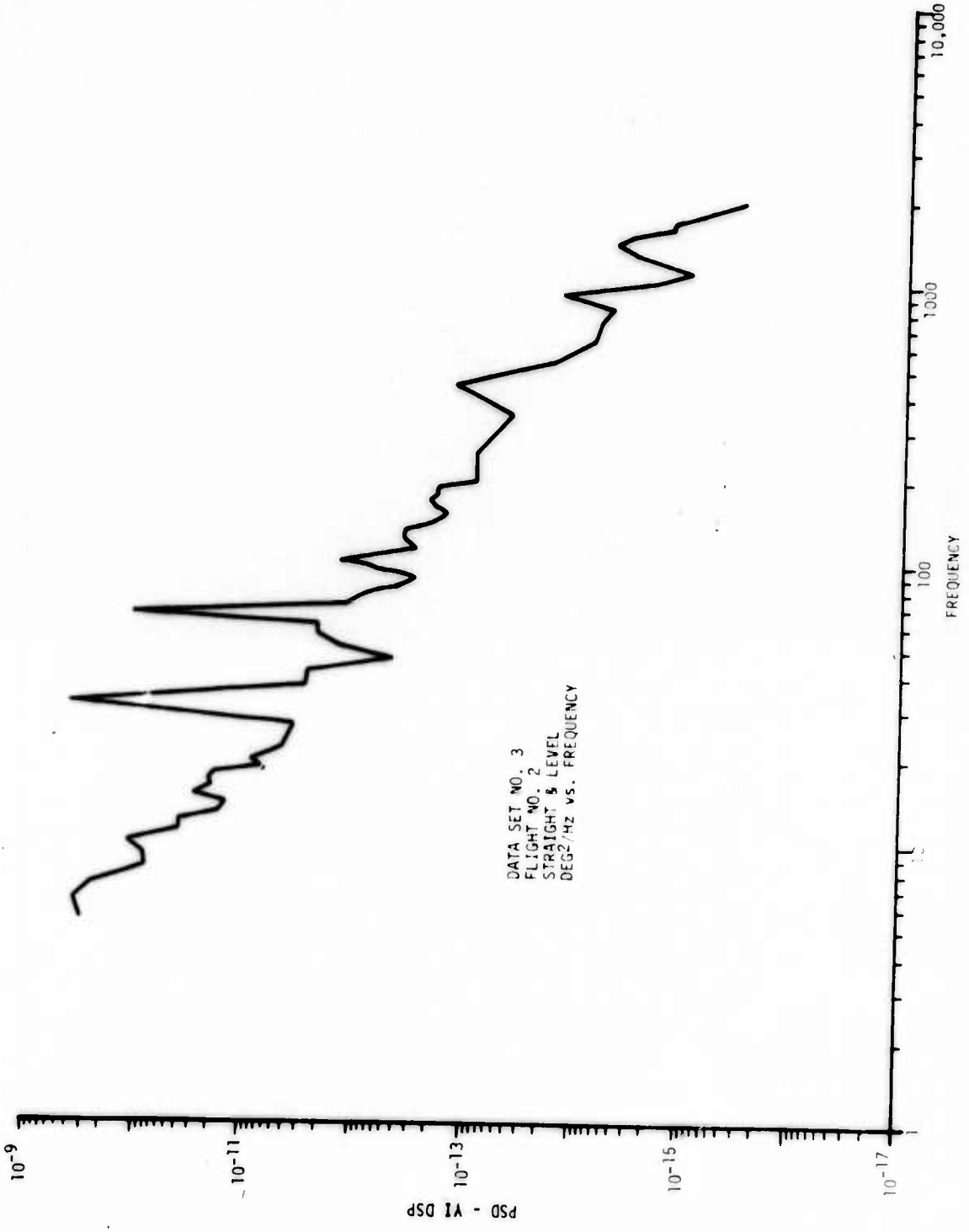
PSD - Y1 DSP
10^{-9}
10^{-11}
10^{-13}
10^{-15}
10^{-17}
1
100
1000
10,000
FREQUENCY
DATA SET NO. 3
FLIGHT NO. 2
STRAIGHT & LEVEL
DEG²/Hz vs. FREQUENCY

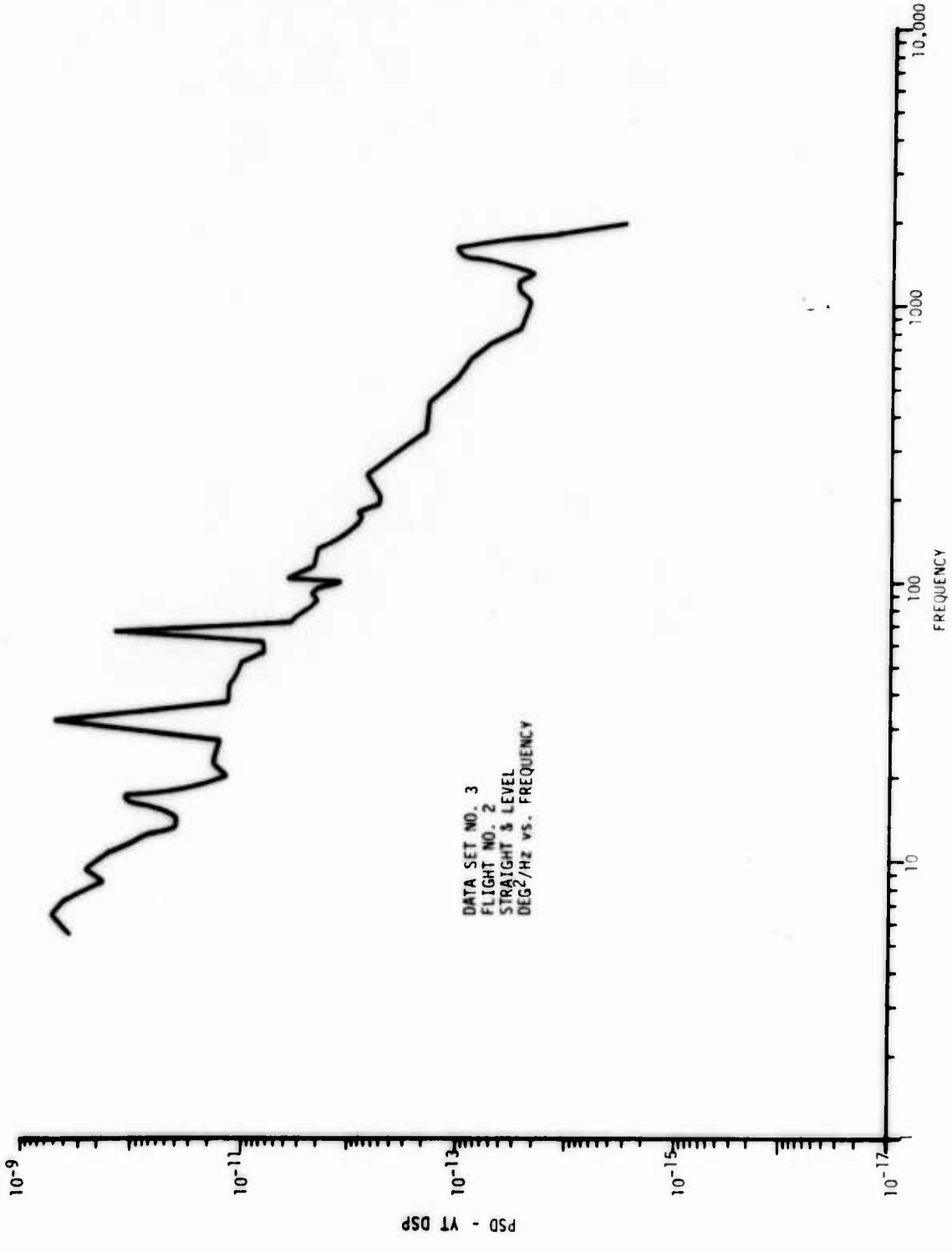
PSD - YT DSP
10^{-9}
10^{-11}
10^{-13}
10^{-15}
10^{-17}
1
10
100
1000
10,000
FREQUENCY
DATA SET NO. 3
FLIGHT NO. 2
STRAIGHT & LEVEL
DEG²/Hz vs. FREQUENCY

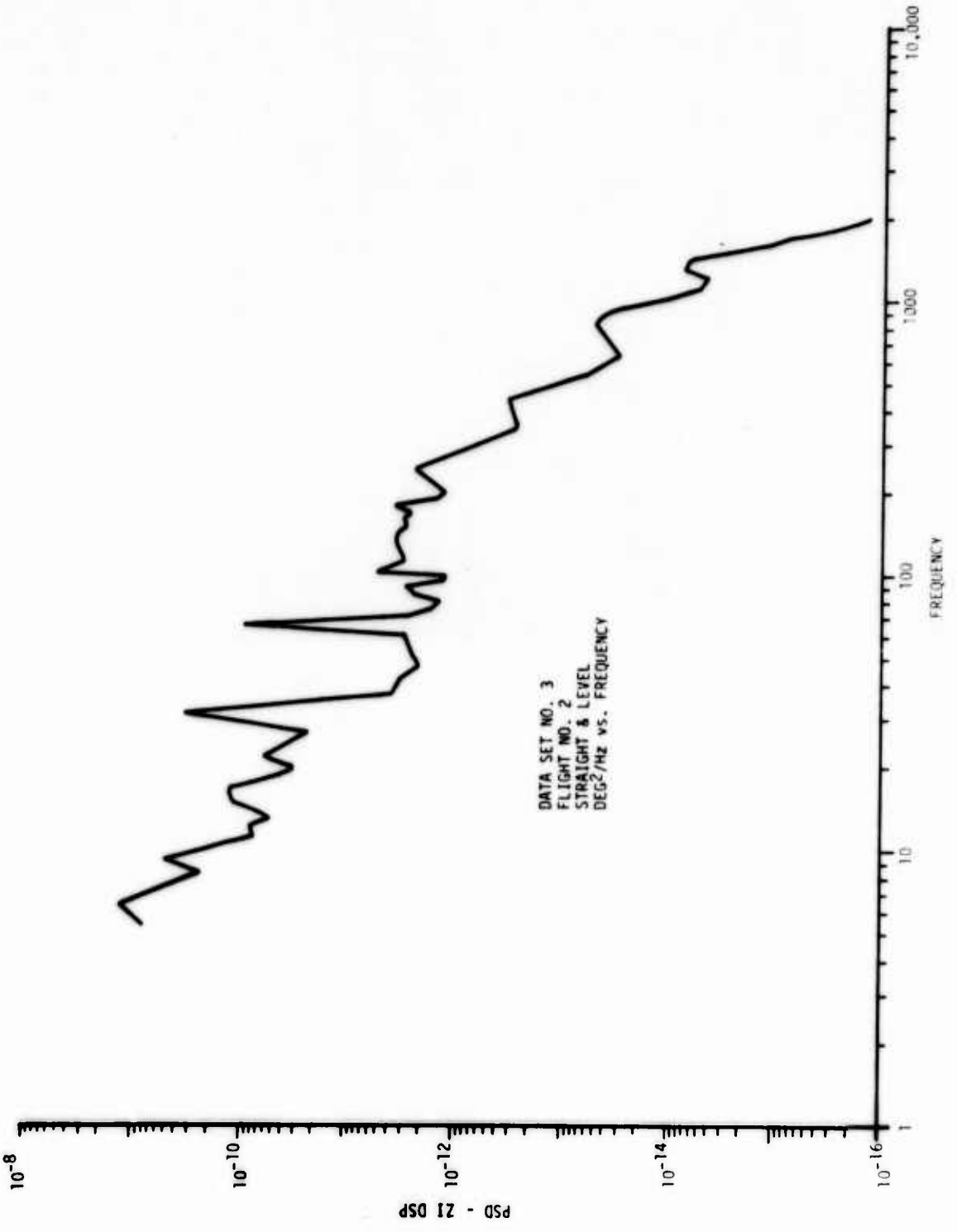
PSD - ZI DSP
10^{-8}
10^{-10}
10^{-12}
10^{-14}
10^{-16}
1
10
100
1000
10,000
FREQUENCY
DATA SET NO. 3
FLIGHT NO. 2
STRAIGHT & LEVEL
DEG²/Hz vs. FREQUENCY

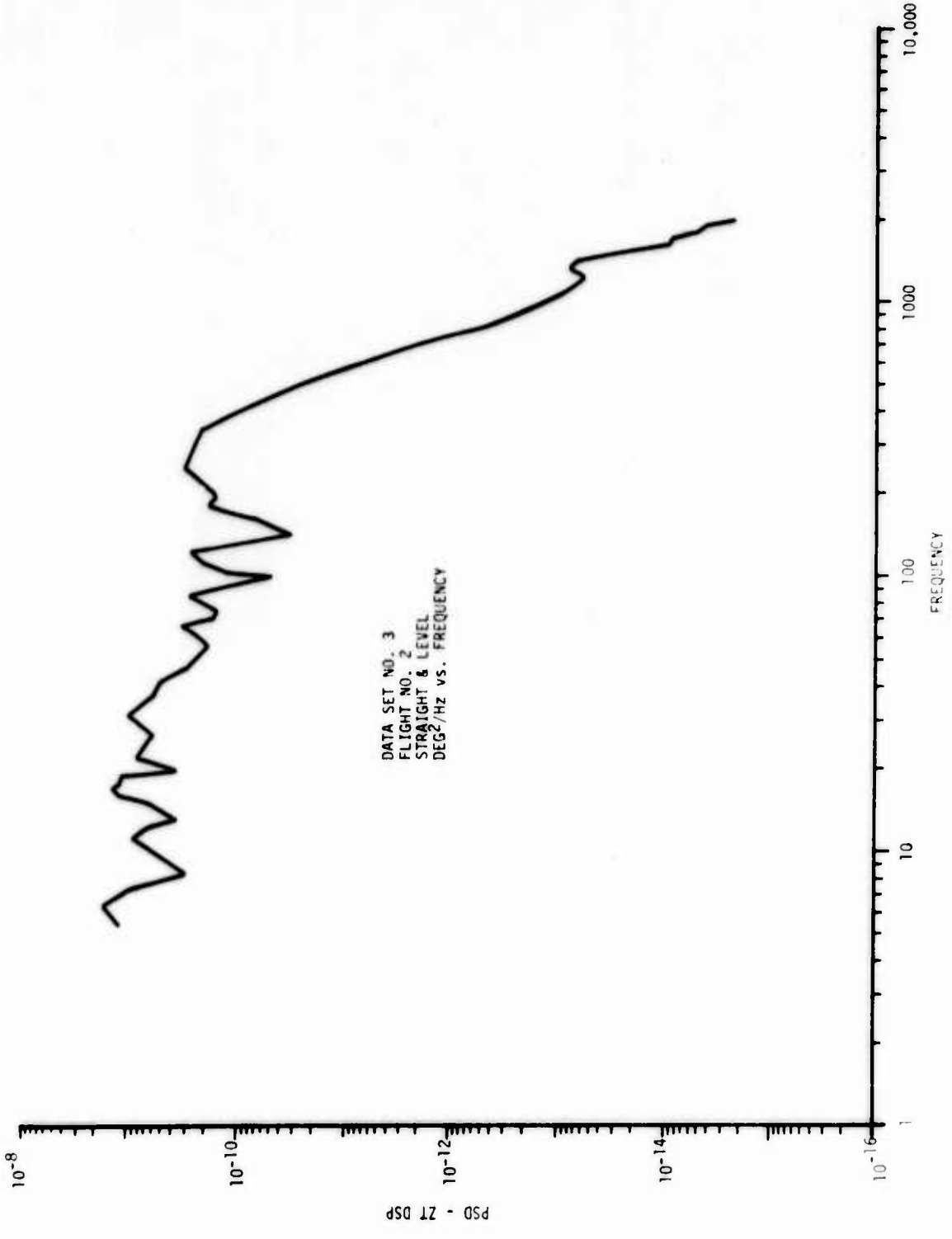
PSD - ZT DSP
10^{-8}
10^{-10}
10^{-12}
10^{-14}
10^{-16}
1
10
100
1000
10,000
FREQUENCY
DATA SET NO. 3
FLIGHT NO. 2
STRAIGHT & LEVEL
DEG²/Hz vs. FREQUENCY

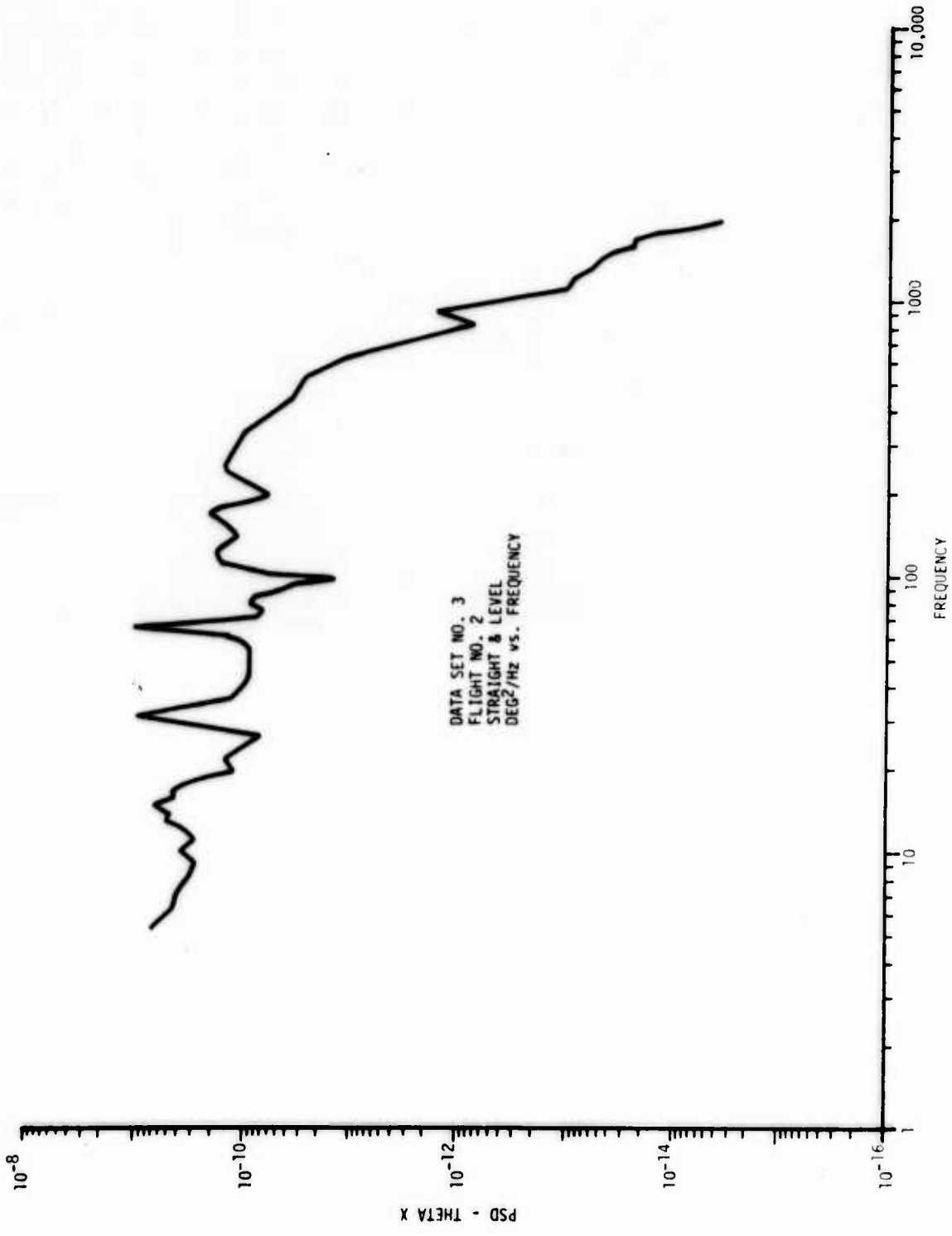
DATA SET NO. 3
FLIGHT NO. 2
STRAIGHT & LEVEL
DEG²/Hz vs. FREQUENCY
PSD - THETA X
10⁻⁸
10⁻¹⁰
10⁻¹²
10⁻¹⁴
10⁻¹⁶
1
10
100
1000
10,000
FREQUENCY

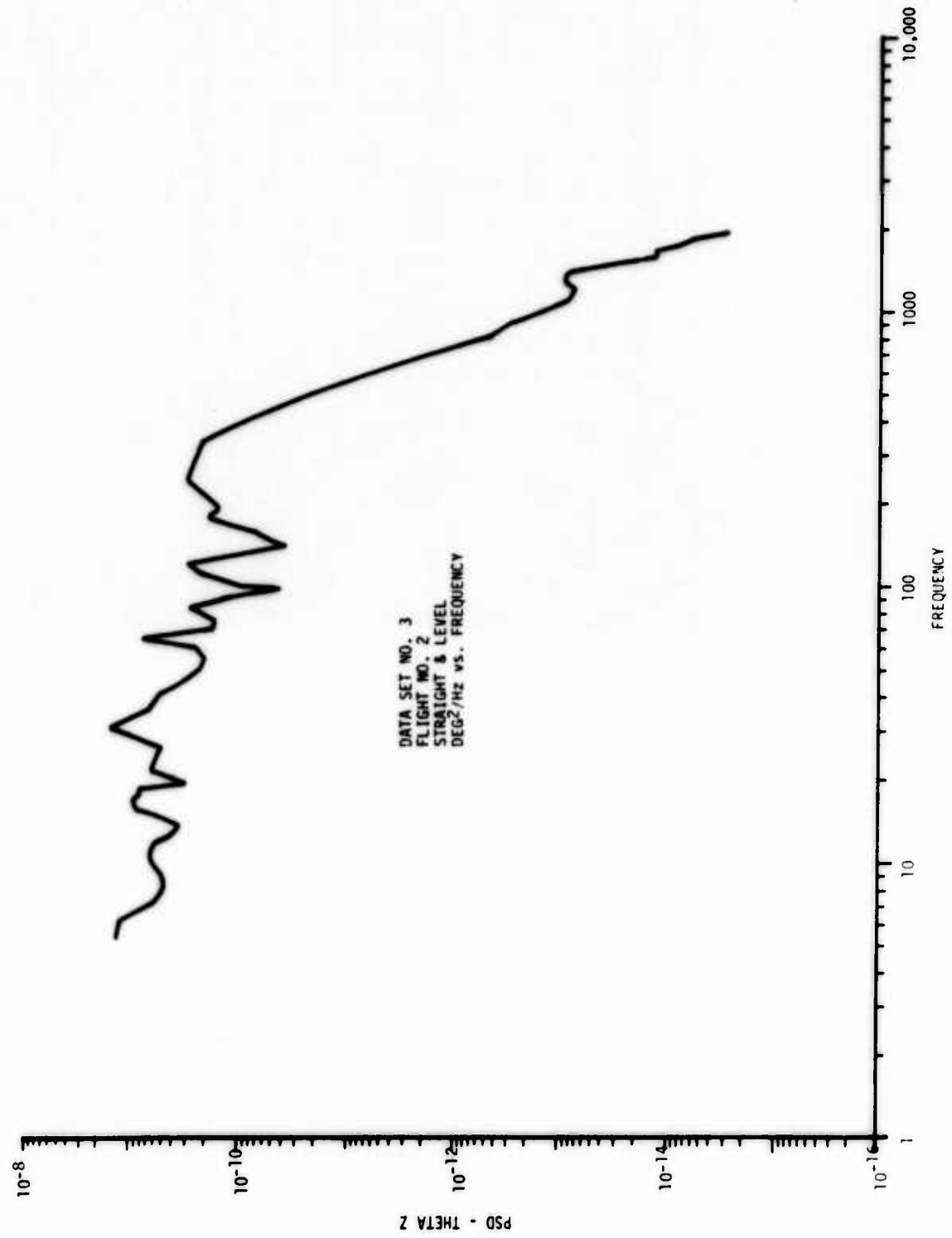
DATA SET NO. 3
FLIGHT NO. 2
STRAIGHT & LEVEL
DEG²/Hz vs. FREQUENCY
PSD - THETA Z
10⁻⁸
10⁻¹⁰
10⁻¹²
10⁻¹⁴
10⁻¹⁶
1
10
100
1000
10,000
FREQUENCY

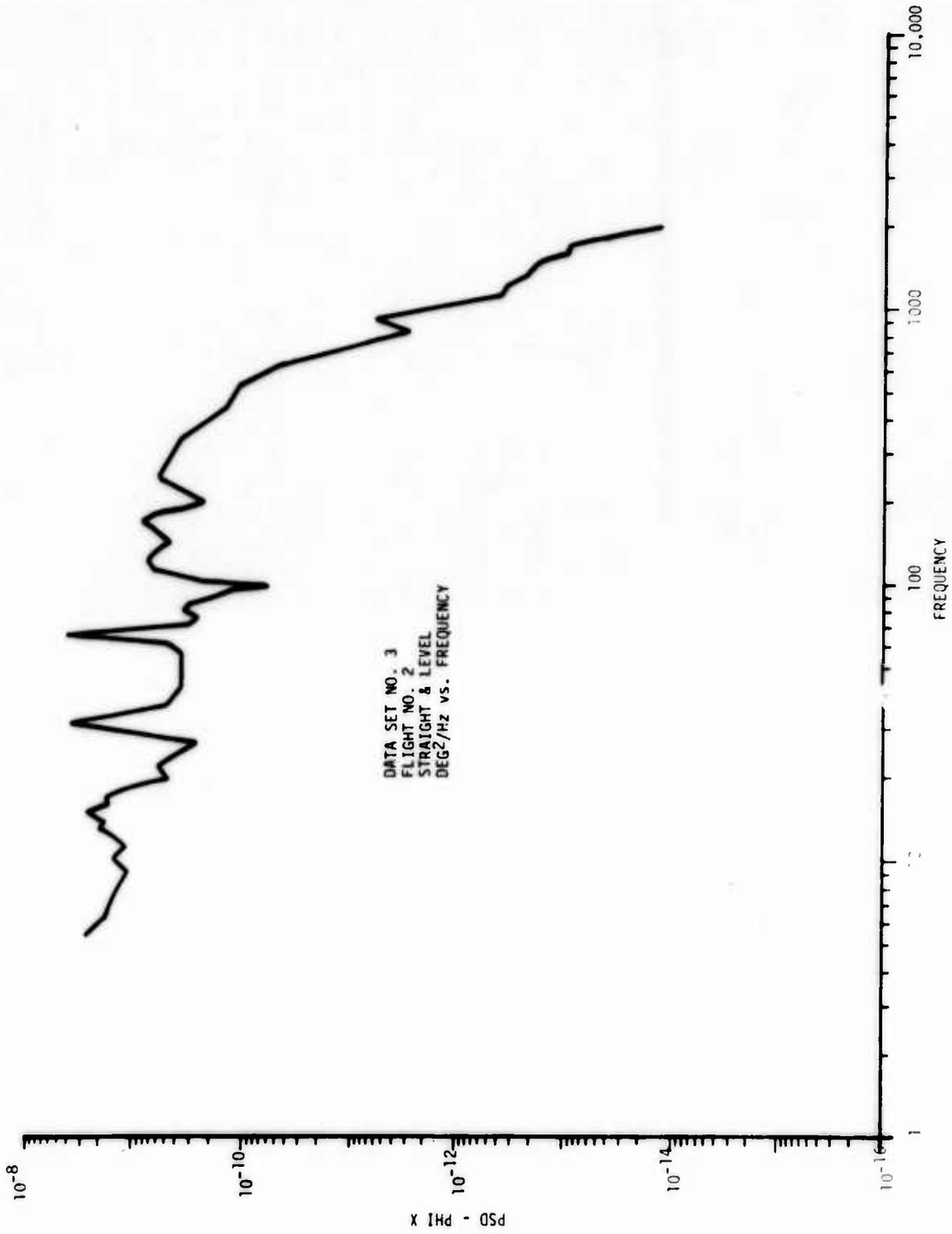
DATA SET NO. 3
FLIGHT NO. 2
STRAIGHT & LEVEL
DEG²/Hz vs. FREQUENCY
PSD - PHI X
10⁻⁸
10⁻¹⁰
10⁻¹²
10⁻¹⁴
10⁻¹⁶
1
100
1000
10,000
FREQUENCY

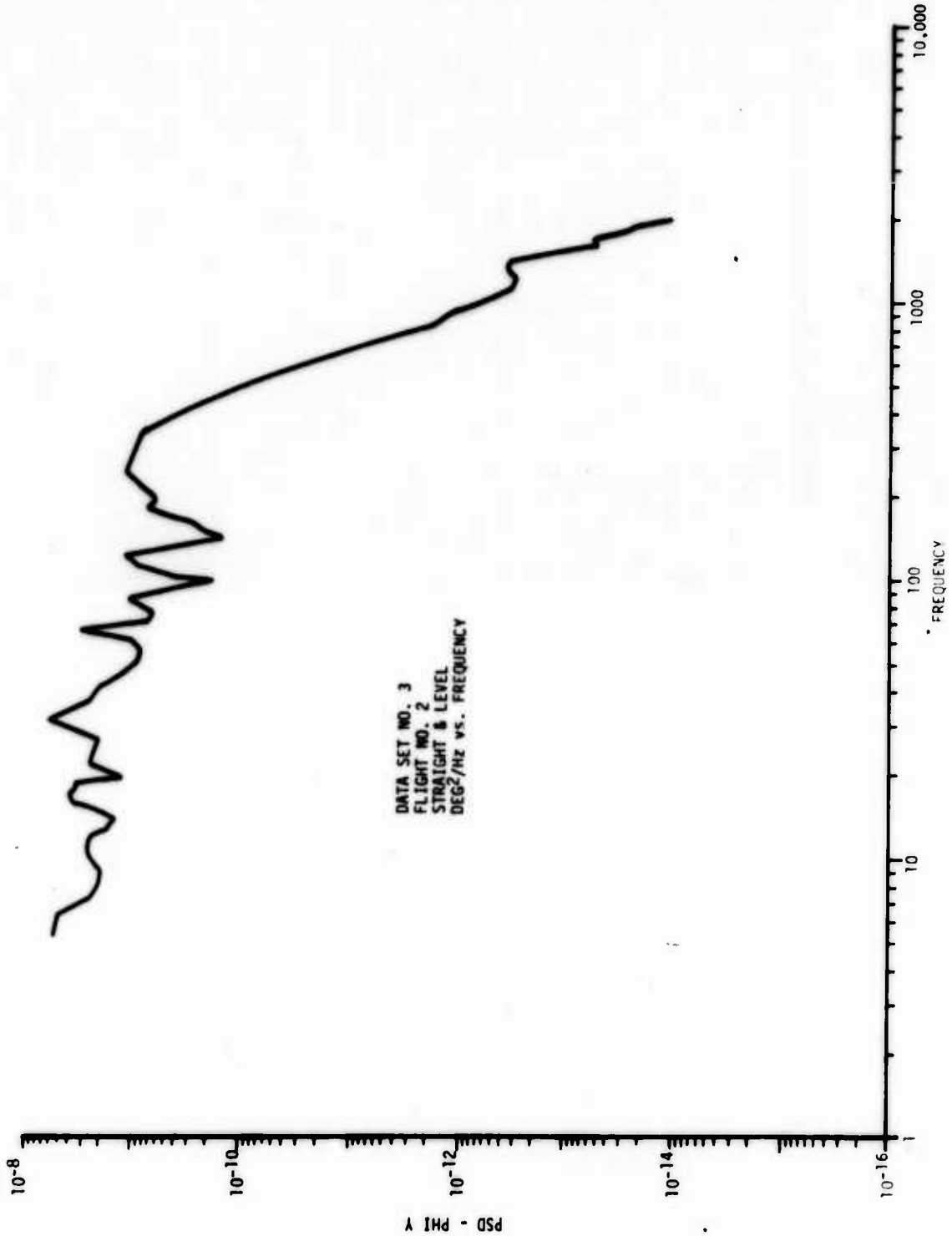
DATA SET NO. 3
FLIGHT NO. 2
STRAIGHT & LEVEL
DEG²/Hz vs. FREQUENCY
PSD - PHI Y
10⁻⁸
10⁻¹⁰
10⁻¹²
10⁻¹⁴
10⁻¹⁶
1
10
100
1000
10,000
FREQUENCY

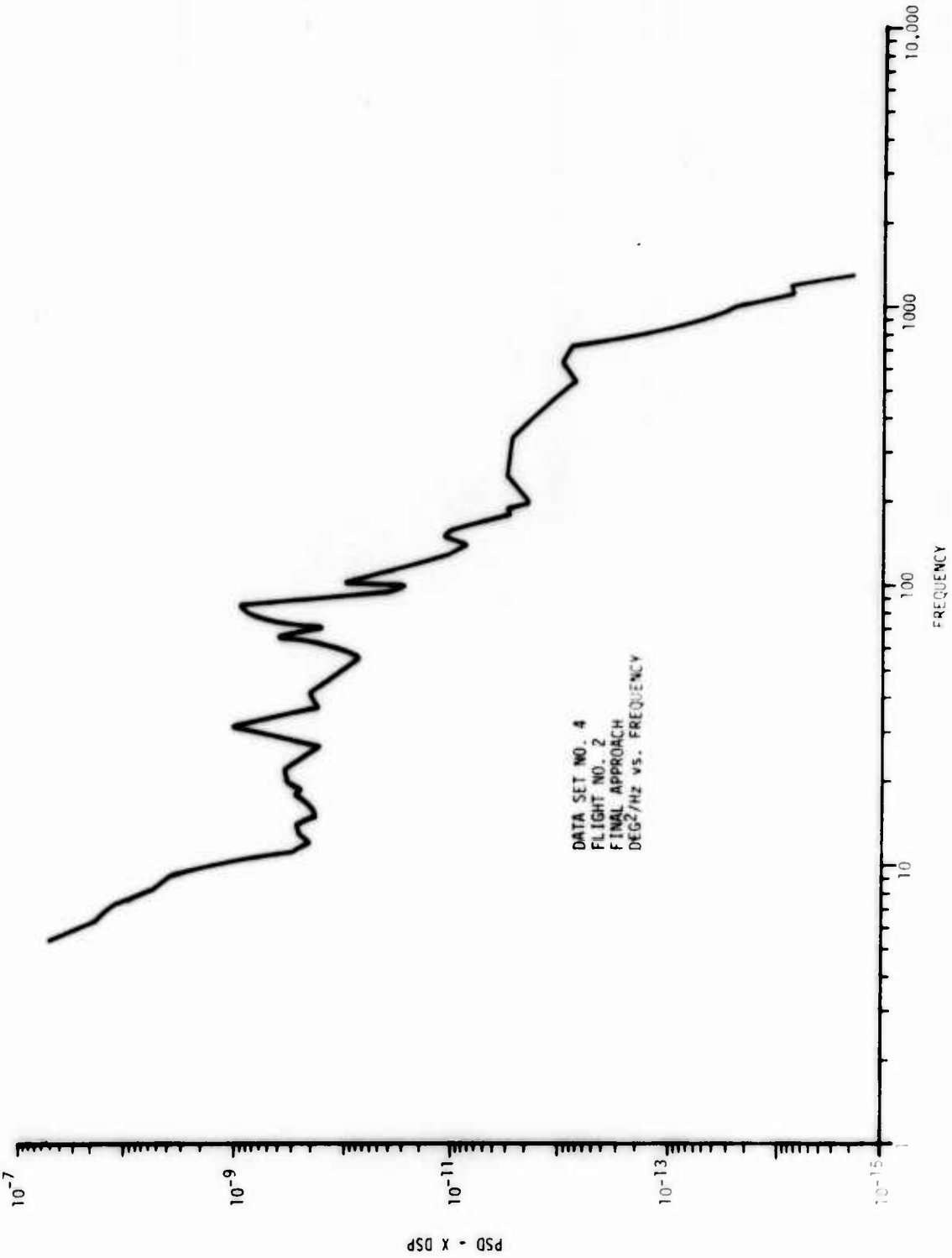
DATA SET NO. 4
FLIGHT NO. 2
FINAL APPROACH
DEG²/Hz vs. FREQUENCY
PSD - X DSP
10^{-7}
10^{-9}
10^{-11}
10^{-13}
10^{-15}
1
10
100
1000
10,000
FREQUENCY

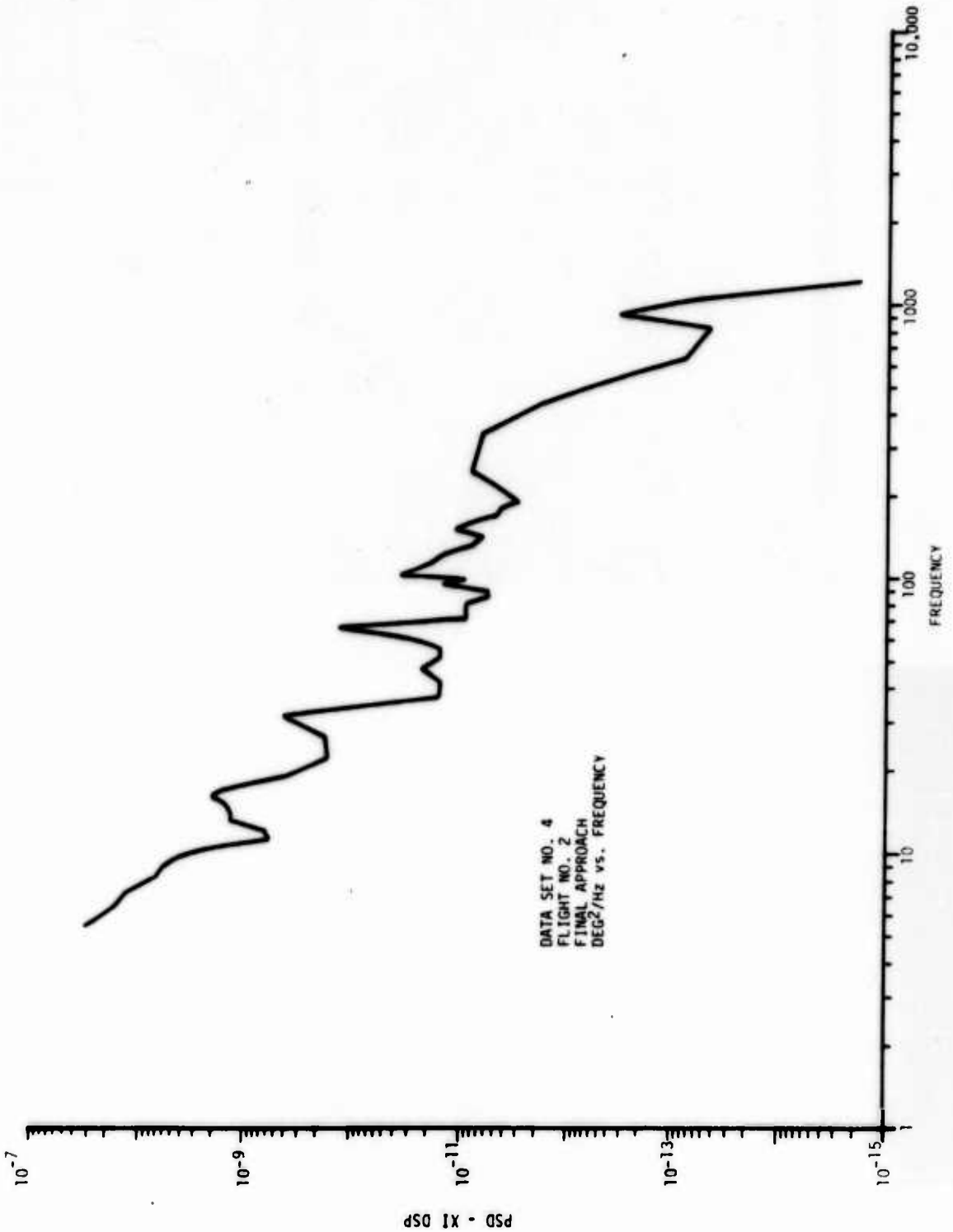
PSD - X1 DSP
10^{-7}
10^{-9}
10^{-11}
10^{-13}
10^{-15}
1
10
100
1000
10,000
FREQUENCY
DATA SET NO. 4
FLIGHT NO. 2
FINAL APPROACH
DEG²/Hz vs. FREQUENCY

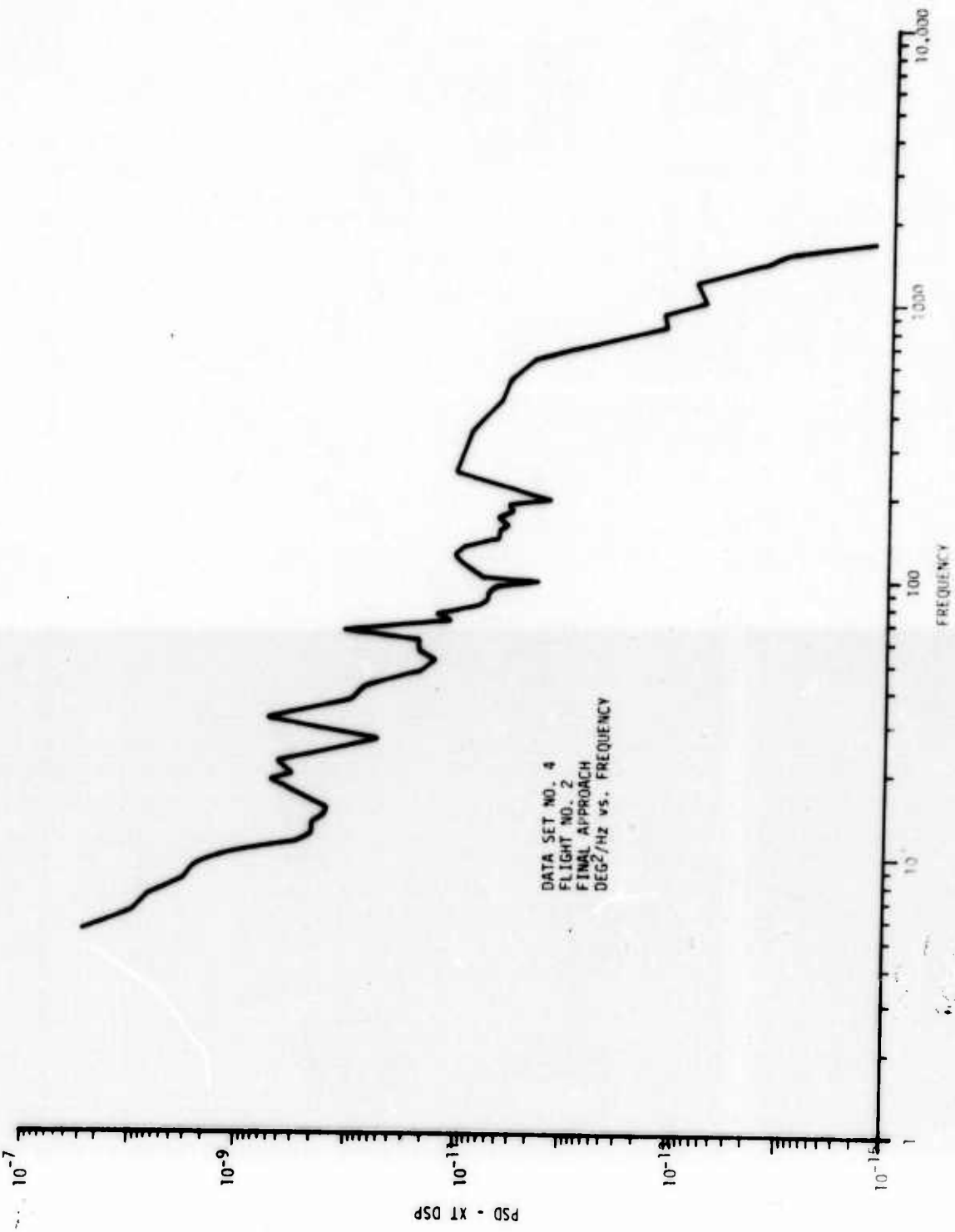
PSD - XT DSP
10^{-7}
10^{-9}
10^{-11}
10^{-13}
10^{-15}
1
10
100
1000
10,000
FREQUENCY
DATA SET NO. 4
FLIGHT NO. 2
FINAL APPROACH
DEG²/Hz vs. FREQUENCY

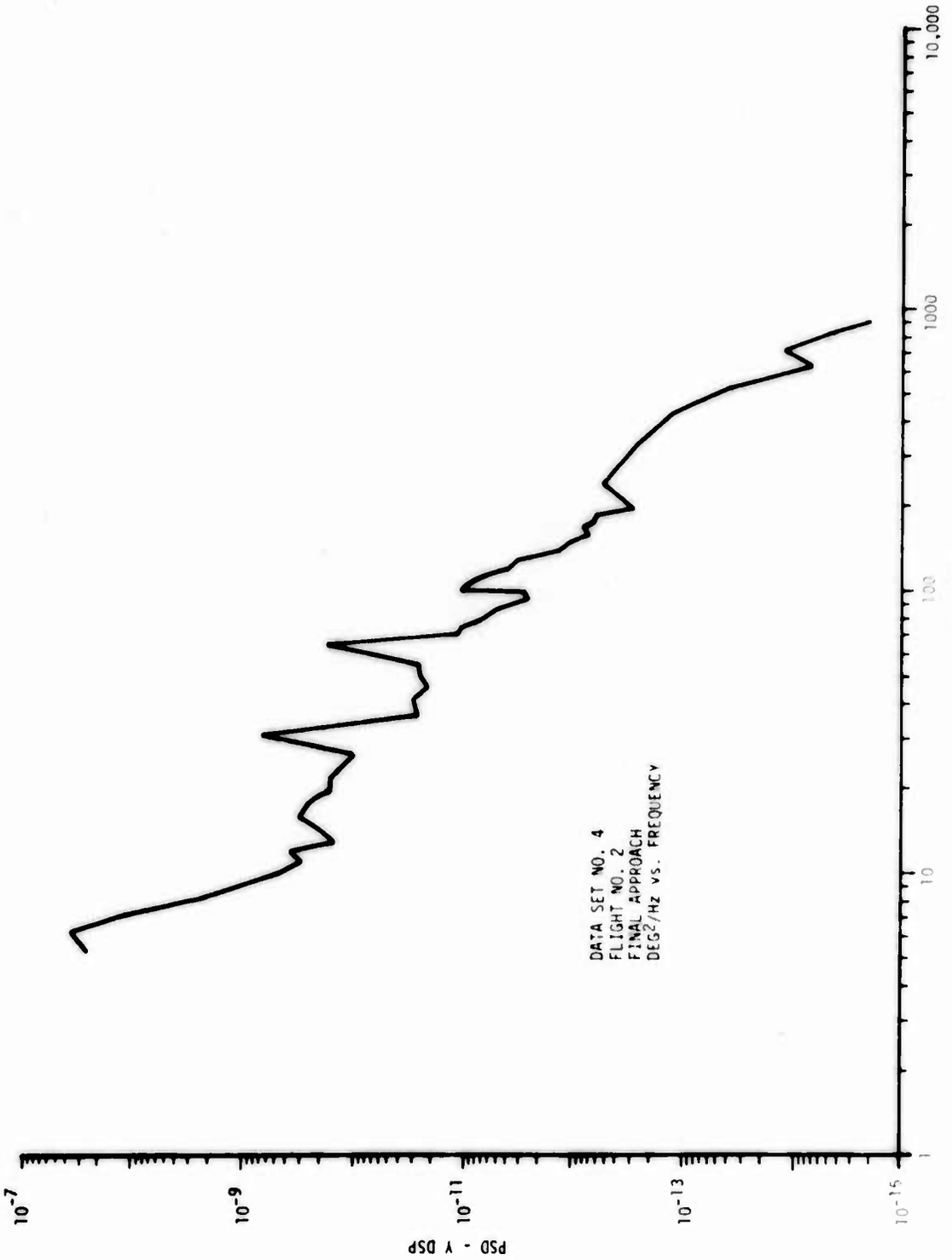
DATA SET NO. 4
FLIGHT NO. 2
FINAL APPROACH
DEG²/Hz vs. FREQUENCY
PSD - Y DSP
10⁻⁷
10⁻⁹
10⁻¹¹
10⁻¹³
10⁻¹⁵
1
10
100
1000
10,000

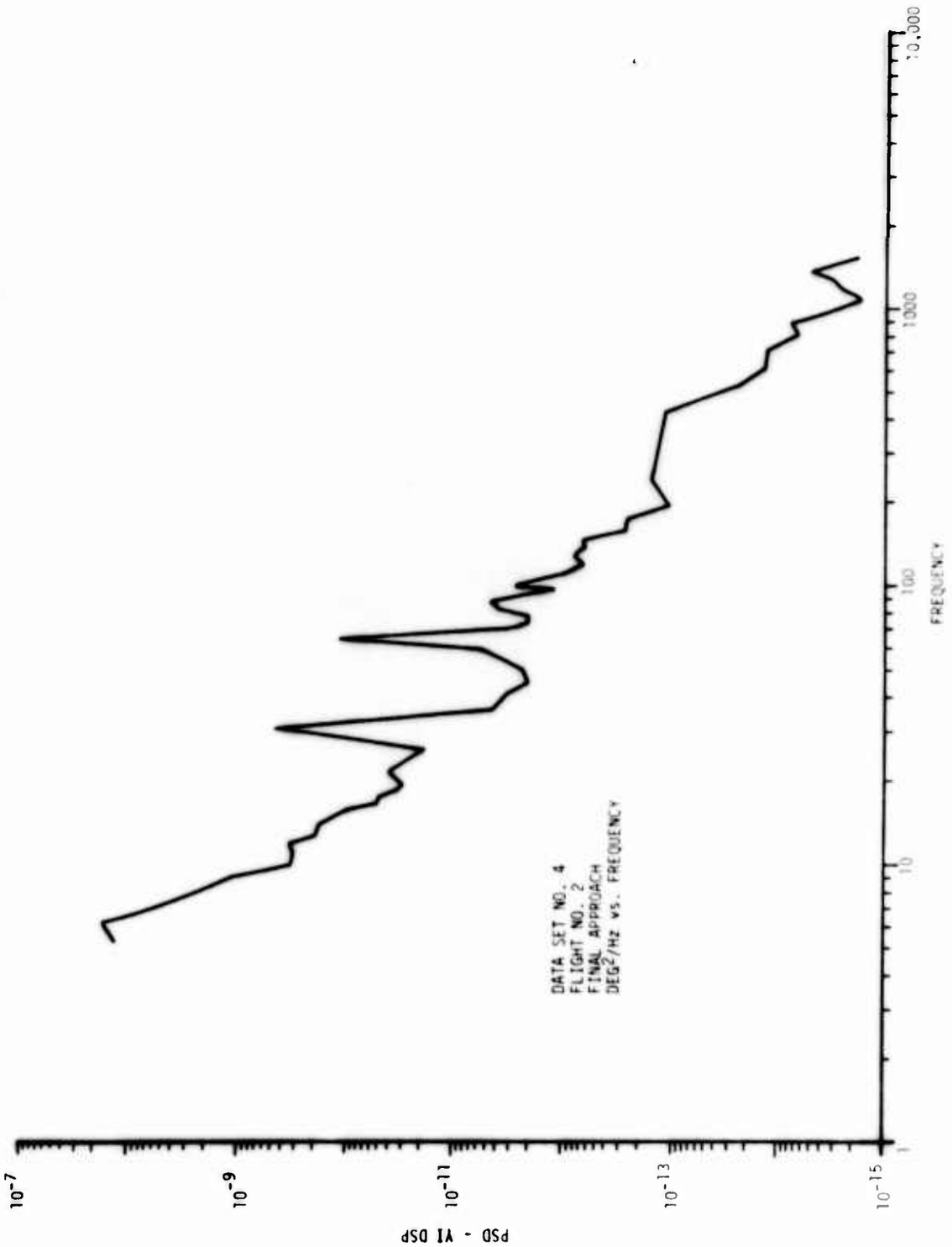
PSD - Y1 DSP
10^{-7}
10^{-9}
10^{-11}
10^{-13}
10^{-15}
1
10
100
1000
10,000
FREQUENCY
DATA SET NO. 4
FLIGHT NO. 2
FINAL APPROACH
DEG²/Hz vs. FREQUENCY

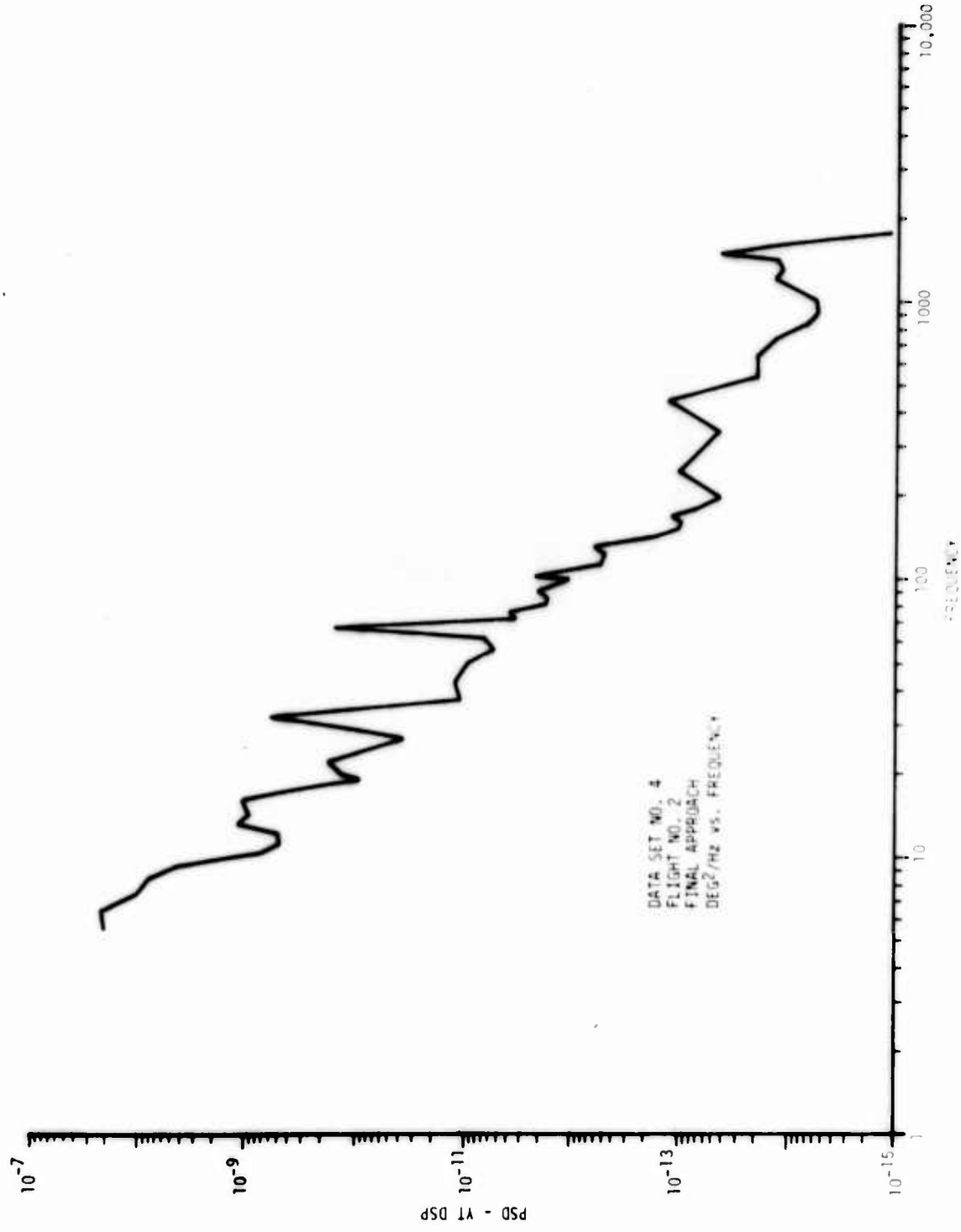
PSD - YT DSP
10^{-7}
10^{-9}
10^{-11}
10^{-13}
10^{-15}
1
10
100
1000
10,000
DATA SET NO. 4
FLIGHT NO. 2
FINAL APPROACH
DEG²/Hz vs. FREQUENCY

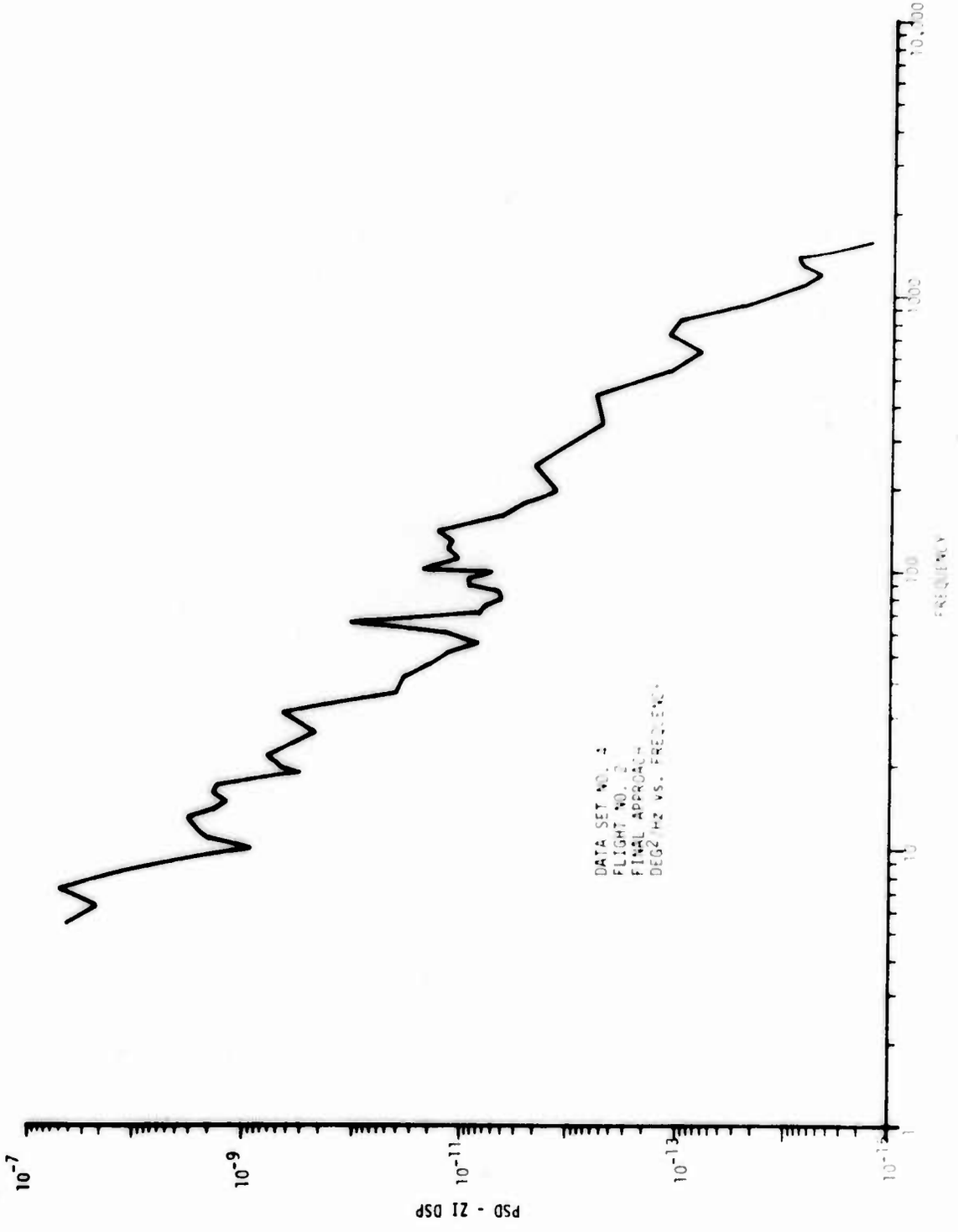
PSD - ZI DSP
10^{-7}
10^{-9}
10^{-11}
10^{-13}
1
10
100
1000
FREQUENCY
DATA SET NO. 4
FLIGHT NO. 2
FINAL APPROACH
DEG² Hz vs. FREQUENCY

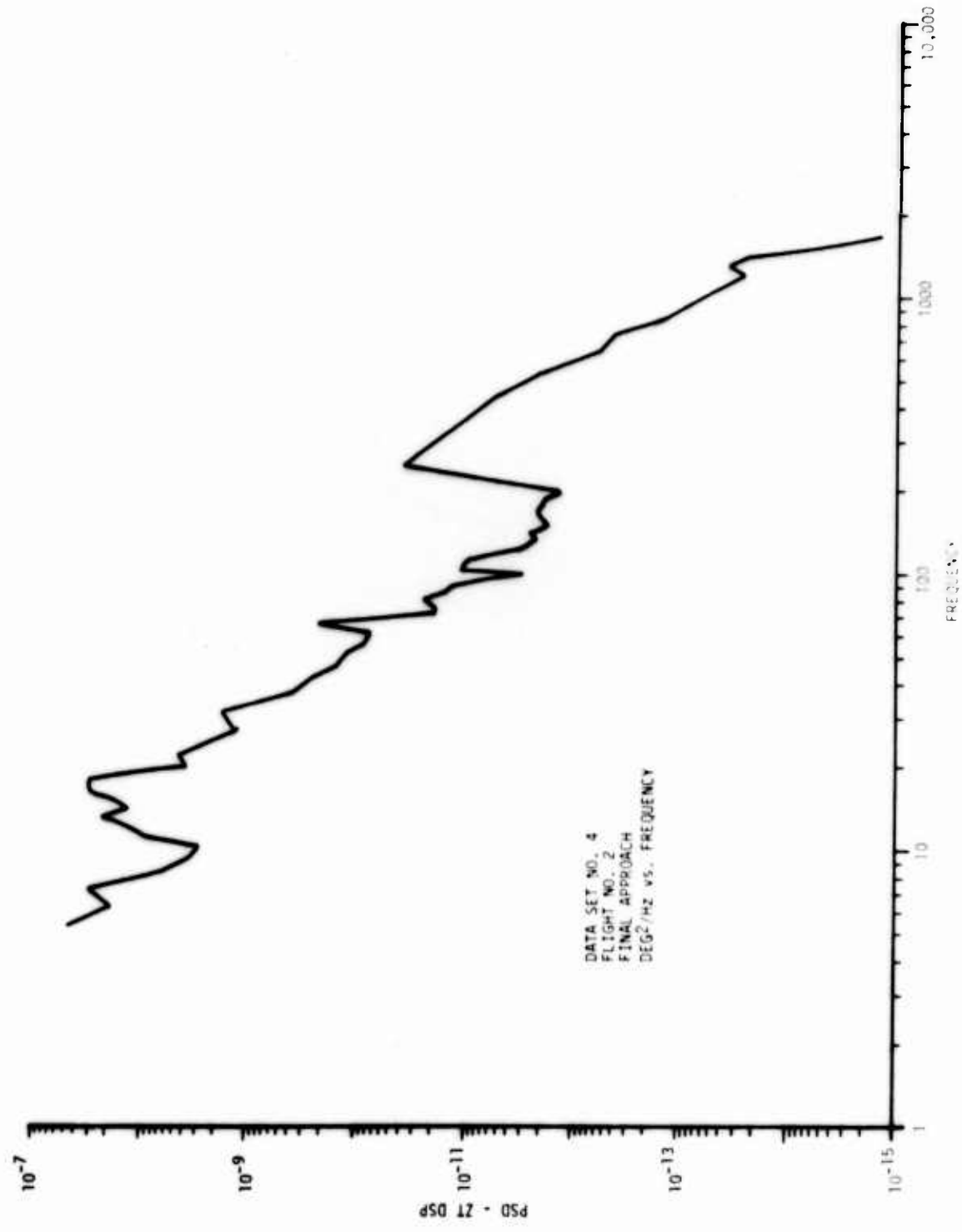
PSD - ZT DSP
10^{-7}
10^{-9}
10^{-11}
10^{-13}
10^{-15}
1
10
100
1000
10,000
DATA SET NO. 4
FLIGHT NO. 2
FINAL APPROACH
DEG²/HZ vs. FREQUENCY

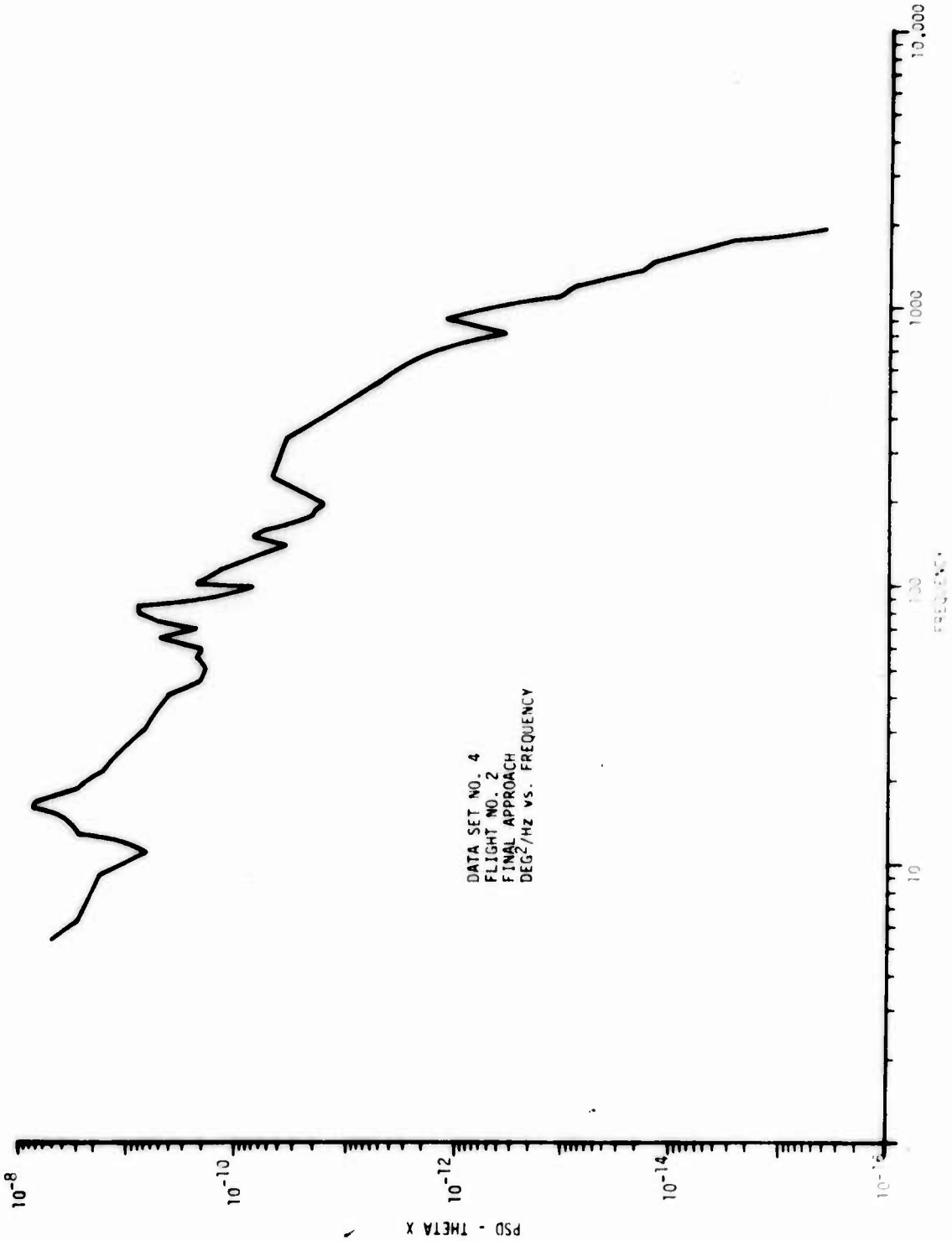
DATA SET NO. 4
FLIGHT NO. 2
FINAL APPROACH
DEG²/Hz vs. FREQUENCY
PSD - THETA X
10⁻⁸
10⁻¹⁰
10⁻¹²
10⁻¹⁴
10
100
1000
10,000

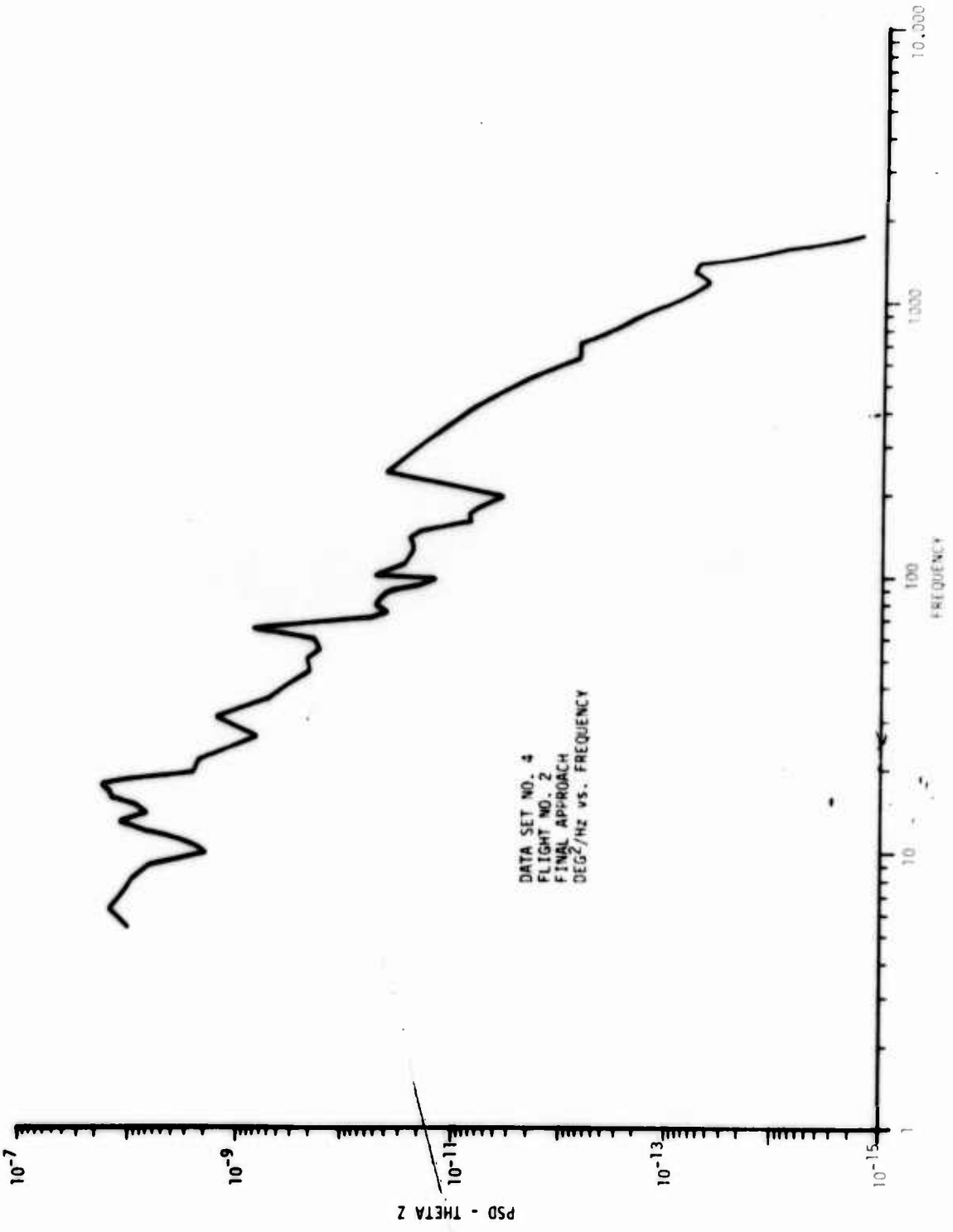
DATA SET NO. 4
FLIGHT NO. 2
FINAL APPROACH
DEG²/Hz vs. FREQUENCY
PSD - THETA Z
FREQUENCY
10⁻⁷
10⁻⁹
10⁻¹¹
10⁻¹³
10⁻¹⁵
1
10
100
1000
10,000

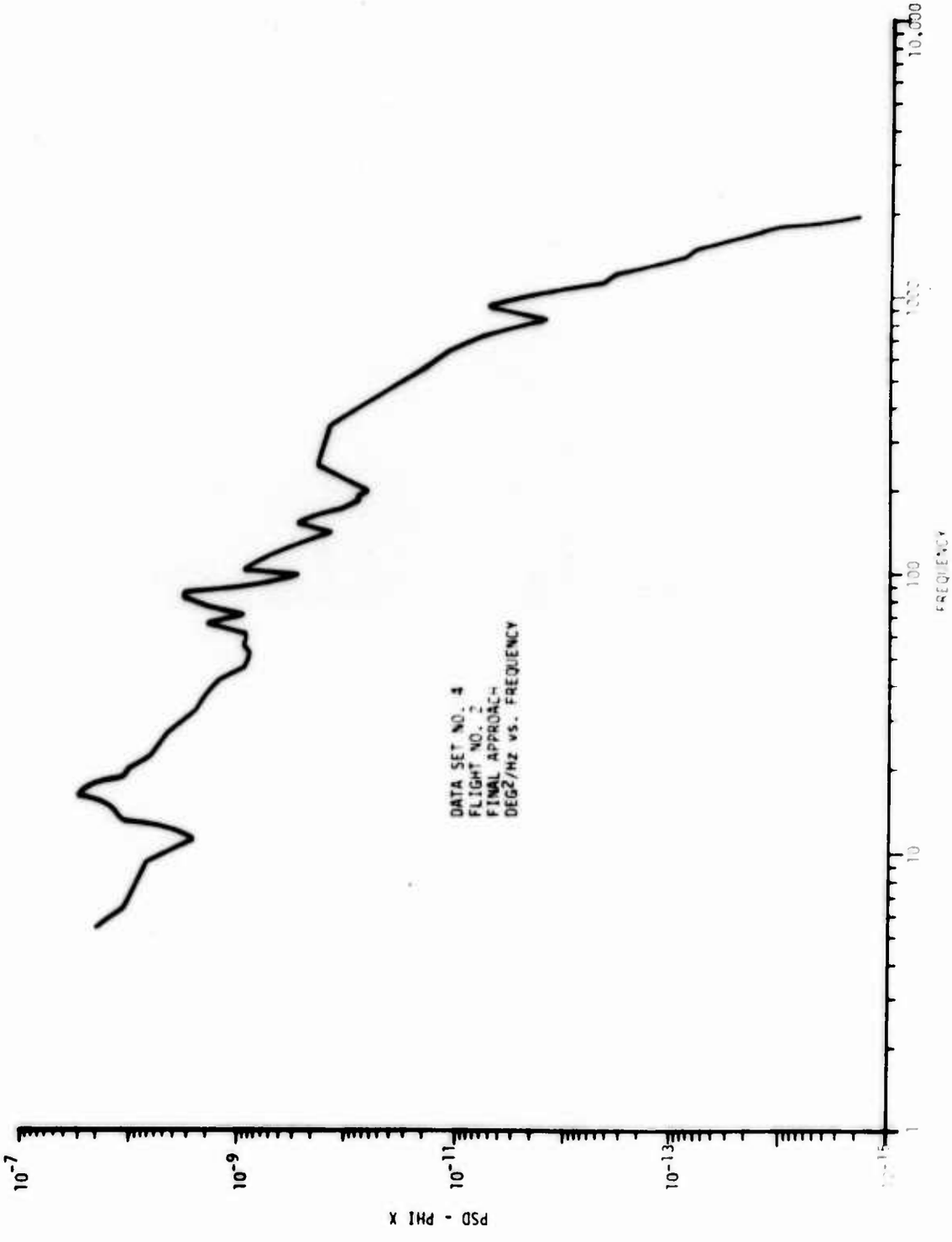
DATA SET NO. 4
FLIGHT NO. 2
FINAL APPROAC-
DEG2/Hz vs. FREQUENCY
PSD - PHI X
10^{-7}
10^{-9}
10^{-11}
10^{-13}
1
10
100
10,000
FREQUENCY

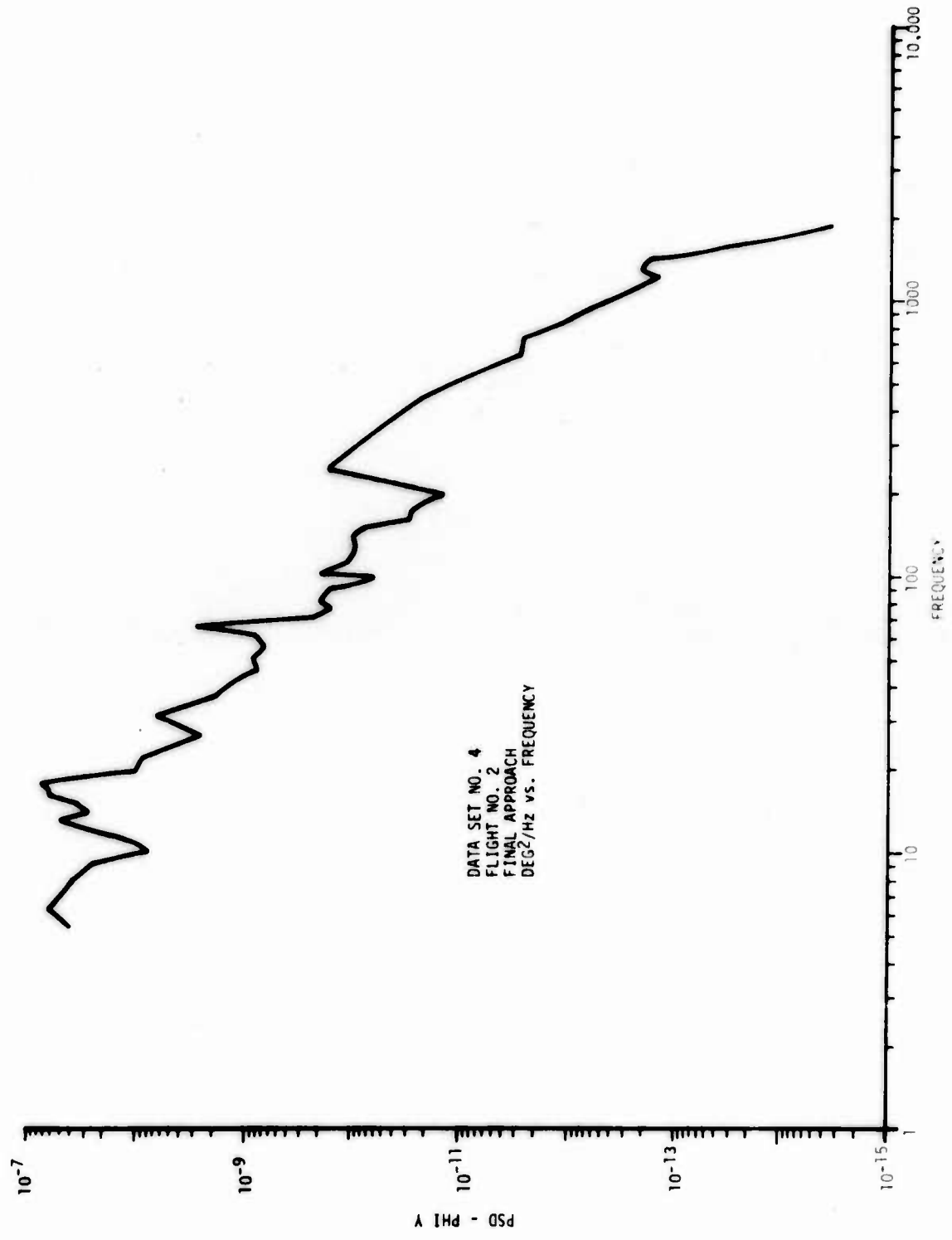
DATA SET NO. 4
FLIGHT NO. 2
FINAL APPROACH
DEG²/Hz vs. FREQUENCY
PSD - PHI Y
10⁻⁷
10⁻⁹
10⁻¹¹
10⁻¹³
10⁻¹⁵
1
10
100
1000
10,000
FREQUENCY

REFERENCES

1. Whittaker, Burdin, "A Gyro-Stabilized Heliostat for Airborne Astronomy," ISA TRANS. Vol. 5, No. 2, 1966.

2. Comfort, G., Base Motion Isolation of a 2-Axis Beam Deflector, SLR-TR-72-0008, F. J. Seiler Research Lab, USAF Academy, Colorado Springs, Colorado, DDC #AD-743002.

3. Rue, A., "Stabilization of Precision Electrooptical Pointing & Tracking Systems," IEEE TRANS. AES, Vol. 5, No. 5, 1969.

4. Canfield, E., Electromechanical Control Systems and Devices, John Wiley, 1965.

5. Sher, L., Fagan, J., Strapdown Navigator Errors in a Vibration Environment, Fifth Inertial Guidance Test Symposium, Holloman AFB, New Mexico, 1970.

UNCLASSIFIED
Security Classification

DOCUMENT CONTROL DATA - R & D
(Security classification of title, body of abstract and indexing annotation must be entered when the overall report is classified)

1 ORIGINATING ACTIVITY (Corporate author)
Air Force Weapons Laboratory (LRO)
Kirtland Air Force Base, New Mexico 87117

2a. REPORT SECURITY CLASSIFICATION
UNCLASSIFIED

2b. GROUP

3 REPORT TITLE
ANGULAR VIBRATION EFFECTS ON A TELESCOPE SYSTEM

4 DESCRIPTIVE NOTES (Type of report and inclusive dates)
January 1972 through September 1972

5 AUTHOR(S) (First name, middle initial, last name)
Lawrence Sher

6. REPORT DATE
January 1973

7a. TOTAL NO. OF PAGES
105

7b. NO. OF REFS
5

8a. CONTRACT OR GRANT NO.

b. PROJECT NO 317J
Task II

c

d.

9a. ORIGINATOR'S REPORT NUMBER(S)
AFWL-TR-72-202

9b. OTHER REPORT NO(S) (Any other numbers that may be assigned this report)

10. DISTRIBUTION STATEMENT
Distribution limited to US Government agencies only because of test and evaluation (Feb 73). Other requests for this document must be referred to AFWL (LRO), Kirtland AFB, NM

11 SUPPLEMENTARY NOTES

12 SPONSORING MILITARY ACTIVITY
AFWL (LRO)
Kirtland AFB, NM 87117

13 ABSTRACT

(Distribution Limitation Statement B

The results of angular vibration measurements made at three stations in an NC-135 aircraft are described. The magnitude of the relative motions between stations is calculated. The requirements for the range of corrections required for an autocollimator to correct the relative motion between the three stations are determined. The effects of the motions at the aircraft ceiling on the angular stability of various types of pointing systems are calculated and discussed.

DD FORM 1 NOV 65 1473

UNCLASSIFIED
Security Classification

14 KEY WORDS	LINK A		LINK B		LINK C	
	ROLE	WT	ROLE	WT	ROLE	WT
Angular vibration Optical system Pointing and tracking Control systems						